Final Report

APN 2000-16

Atmospheric Aerosols and their Impact on UV Radiation over the Northeast Asia

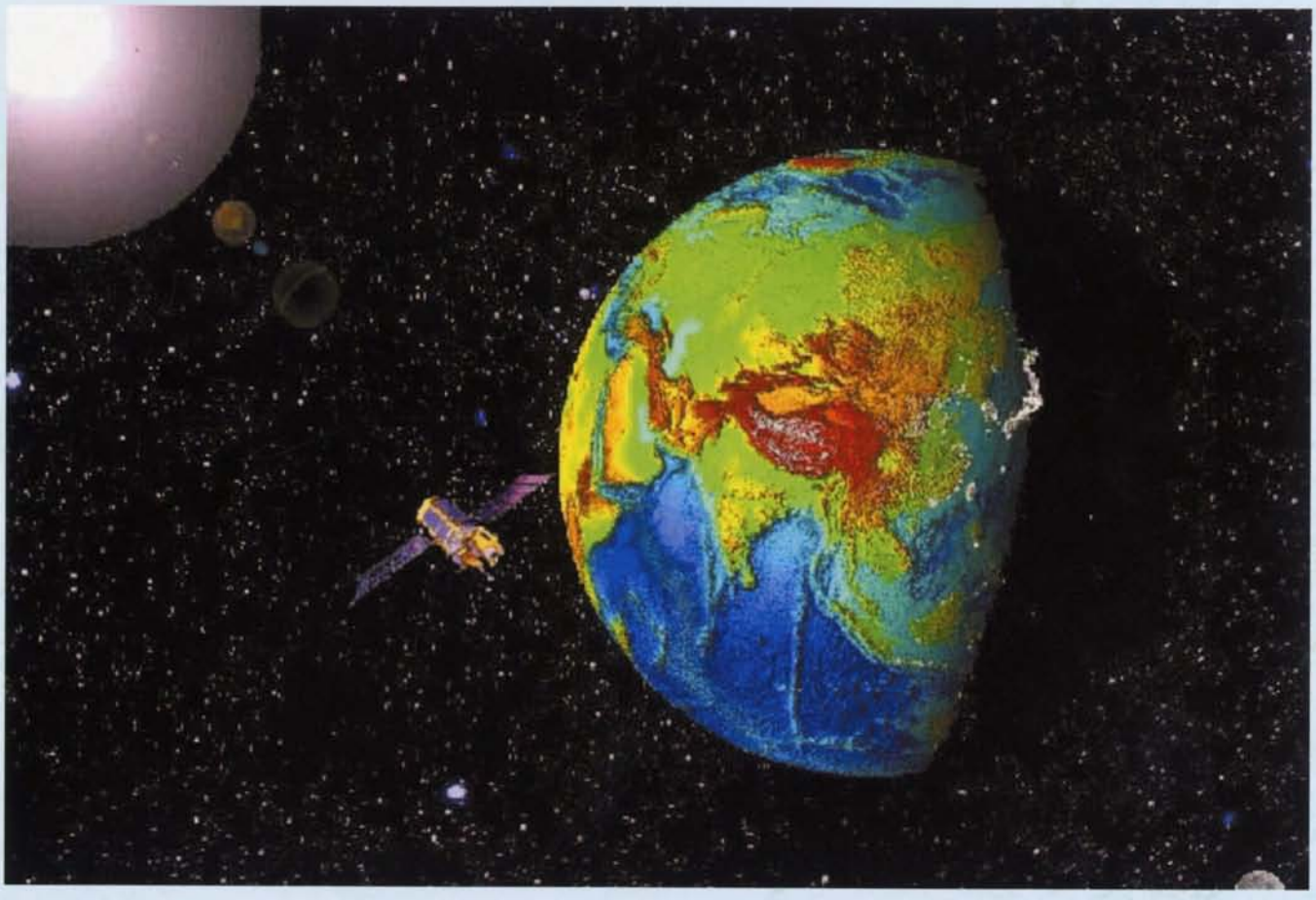

The **A**sia-**P**acific **N**etwork for Global Change Research(**APN**)

Global change for System for Analysis, Research and Training

Final Report **APN 2000-16**

Atmospheric Aerosols and their Impact on UV Radiation over the Northeast Asia

The **A**sia-**P**acific **N**etwork for Global Change Research(**APN**)

Global change for System for Analysis, Research and Training

Project Leader: Professor Young J Kim

(Kwangju Institute of Science and Technology, Korea)

Korea : Kwangju Institute of Science and Technology (KJIST)

Professor, Young J Kim

Assistant Researcher, Seong Y Ryu

Assistant Researcher, Kehinde Ogunjobi

Assistant Researcher, Jeong E Kim

China : Institute of Atmospheric Physics (IAP)

Professor, Guang-Yu Shi

Associate Professor, Wang Biao

Ph. D, Wang Xihong

Senior Engineer, Chen Huansen

Japan : Kyoto University

Professor, Mikio Kasahara

Associate Professor, Susumi Tohno

Assistant Researcher, Kohei Yamamato

Mongolia : Central Laboratory of Environmental Monitoring (CLEM)

Ministry for Nature and Environment

Ms. Bolormaa Batsukh (Ministry for Nature and Environment)

Dr. Tumendemberel Bulgan (CLEM)

Table of Contents

List of Tables

List of Figures

1. EXECUTIVE SUMMARY

1. Executive Summary

Atmospheric Aerosols and their Impact on UV Radiation in the Northeast Asia

Introduction

Atmospheric aerosol particles influence the Earth's radiation balance directly by scattering and absorbing incoming solar radiation fluxes. Secondly, it can also affect the global climate indirectly by modifying the properties of clouds through microphysical processes and by altering abundance of radiatively important gases through heterogeneous chemistry. The radiative forcing by anthropogenic aerosol particles due to the combined effects is estimated to be in the range between –0.4 and –3.0 w/m^2 on a global scale (IPCC, 1995). There is however a substantial uncertainty in the magnitude and spatial distribution of the radiative forcing by aerosols. This uncertainty significantly limits our ability to assess the effect of natural and human induced changes in the chemistry of the atmosphere on global climate. With the above-mentioned limitation there exists need for comprehensive monitoring of changes in global atmospheric aerosol loading.

The growing evidence of global depletion of stratospheric ozone has emphasized the importance of monitoring terrestrial ultraviolet radiation. UV radiation affects many chemical and biological processes. Any increase in the UV radiation intensity is of great concern because of its potential adverse effects on the biosphere, tropospheric air quality and materials such as wood and polymers. Therefore, there is also need for characterizing atmospheric aerosols and their impact on UV radiation in the Northeast Asia through international collaboration.

Objectives of the project

The objectives of this research project includes

- to determine the physical, chemical, and radiative properties of atmospheric aerosol in the Northeast Asia.
- to monitor the variation of UV radiation in the Northeast Asia.
- to investigate the atmospheric aerosols' impact on UV radiation in the Northeast Asia.

- to provide useful data for characterizing changes in atmospheric compositions in the Northeast Asia.

Outline of activities conducted

(i) Chemical properties of aerosols over the Northeast Asia:

Aerosol samples were collected with $PM_{2.5}$ and MOUDI (Micro-Orifice Uniform Deposition Impactor) samplers at Kwangju, Beijing, and Kyoto. Three intensive samplings were conducted in August, November 2000, and January 2001, respectively. The method of ion chromatography and carbon analysis was used to determine the chemical properties of the atmospheric aerosol.

(ii) Physical and optical properties of aerosols:

Using nephelometer, aethalometer and MOUDI, the scattering and absorption coefficients as well as size distribution of atmospheric aerosols were characterized at Kwangju and Kyoto.

(iii) Radiative properties over the Northeast Asia region:

Using Rotation Shadow band Radiometer (RSR) and a Multi-Filter Rotating Shadow band Radiometer (MFRSR) at Kwangju, aerosol optical depth (AOD) was determined in order to investigate the changes in atmospheric aerosol loading. RSR measurement was performed at four sites in the Northeast Asia ; Kwangju, Beijing, Kyoto and Ulaanbaatar.

(iv) UV radiation:

Changes in surface UV radiation was monitored intensively by UV-B radiometers at Kwangju, Beijing, Kyoto and Ulanbaartaar. Measured aerosol and UV data were analyzed to characterize the atmospheric aerosols' impact on UV radiation and to provide information on atmospheric compositions changes in the region.

Measurement

Measurements parameters at each monitoring station are summarized in Table 1.1.

Table 1.1 Measured parameters at four monitoring stations.

Site	Continuous Monitoring		Intensive Aerosol Sampling		
	RSR	UV-B	1st 14. Aug. ~ 21. Aug. 2000	2nd 30. Oct. ~ 6. Nov. 2000	3rd 14. Jan. ~ 21. Jan. 2001
Kwangju, Korea Lat.35°13'N, Long.126°53'E	Mar. 2000 ~	Apr. 2000 ~	PM 2.5 URG Cyclone Sampler	PM 2.5 URG Cyclone Sampler	PM 2.5 URG Cyclone Sampler, MOUDI
Kyoto, Japan Lat.34° 78' N, Long.135° 85'E	Mar. 2000 ~	Oct. 2000 ~			
Beijing, China Lat39° 52' N, Long.123° 53'E	Aug. 2000 ~				
Ulaanbaatar Mongolia Lat.47°55'N, Long.106° 55'E	Oct. 2000 ~	Oct. 2000 ~			

Future Works

We are currently participating in the ACE-Asia (Aerosol Characterization Experiment) program, which is one of the activities of the International Global

Atmospheric Chemistry of IGBP (International Geo-sphere-Biosphere Program). This APN project has provided regional scientists the opportunity of collaborating with ACE-Asia activities. The APN program will be of great benefit and exposure to the ACE-Asia program through data exchange and scientific collaboration. Since atmospheric change monitoring requires long-term data accumulation and analysis funding support for continuation of the activities will be actively sought in the future.

2. INTRODUCTION

2. Introduction

Atmospheric aerosol is a significant source of direct and indirect global climate forcing. There is a natural aerosol component consisting mostly of soil dust, sea salt, biogenic sulfates, and organic matter that is geographically and seasonally variable. It plays a fundamental role in cloud formation processes, and also makes a small-amplitude direct radiative forcing contribution (Lacis and Mishchenko, 1995).

There are two major sources of atmospheric aerosols: widespread surface sources and spatial sources. Widespread surface sources implied the sources at the base of the atmospheric volume (e.g., oceans and deserts) while spatial sources refer to those within the atmospheric volume (e.g., gas to particle conversion and clouds). Additional point sources, such as volcanoes, are globally important in their influence on the stratosphere. Otherwise, due to short tropospheric residence times, aerosols from point sources affect mainly regional and local scales (Jaenicke, 1993).

Northeast Asia is an important source region of all major tropospheric aerosols. The fast economic development, the large area of desert, and the intensive forest and agriculture fires in this region contribute to 1/4 to 1/3 of global emissions of SO_2, organic matter, soot, and dust. Northeast Asian aerosols are probably always a mixture of multiple components. For example, mineral dust transported out from the desert can travel over major pollution regions where it can be coated and mixed with sulfate and organic aerosols. It can be further mixed with sea salt particles off the coast. Long-range transport of anthropogenic acidic aerosol and organic aerosol has great impacts on not only regional air quality but also regional climate through radiative balance change.

Visibility impairment, one of the most obvious indications of air pollution, results from light extinction by atmospheric particles and gases. The effects of pollution on light scattering and absorption are particularly strong in urban and industrial air basins than in rural area. Anthropogenic emissions leading to atmospheric aerosols which have been synonymous of modern industrial and technological development, have been implicated in human health effects; visibility reduction, acid deposition and in altering the Earth' radiation balance (Dockery and Pope, 1994; Turpin et al., 1991; Dockery et al., 1992). Many of the recent studies have indicated that among all the pollutants present in a typical urban environment airborne particulate matter, specifically fine particles are the main contributor to visibility degradation (Gray et al., 1998; Countess et al., 1980).

It has been recent years that fine airborne particulate matters in the visibility impairment have begun to receive attention in Korea. Visibility impairment in an urban atmosphere is greatly affected by ambient particulate substances: sulfates, nitrates, organics, elemental carbon, and soil dust. The determination of the contribution of different emission sources to the total light extinction is of great importance in visual air quality control.

Visibility impairment is primarily due to the interaction of light with particles in the atmosphere; gaseous pollutants usually play a small role. Particles interact with light by two important mechanisms: They can absorb light, and they can scatter light in a direction different from that of the incident light (Friedlander S.K., 1977). The magnitude of these effects depends on diverse factors, the most important of which are the size and composition of the particles and the wavelength of the incident light. Despite the diversity of these physical phenomena, a variety of available techniques

make it possible to characterize the optical properties of the atmosphere and to identify and quantify the pollutants that can affect visibility degradation.

The extinction coefficient, b_{ext}, is an important measure of atmospheric transparency and is the measure most directly related to the composition of the atmosphere. It is a measure of the fraction of light energy dE lost from a collimated beam of energy E in traversing a unit thickness of atmosphere dx: $dE = -b_{ext} Edx$. The extinction coefficient has dimensions of inverse length (e.g., Mm^{-1}). The extinction coefficient comprises four additive components:

$$b_{ext} = b_{scat} + b_{abs} = b_{Ray} + b_{sp} + b_{ag} + b_{ap} \qquad (1\text{-}1)$$

where b_{Ray} is light scattering by gas molecules. Gas scattering is almost entirely attributable to oxygen and nitrogen molecules in the air and often is referred to as natural "blue-sky" scatter. It is obviously unaffected by pollutant gases and is 12 Mm^{-1} at the wavelength of 550nm at sea level. b_{sp} is light scattering by particles. This scattering usually is dominated by fine particles, because particles at the size range of $0.1\sim1.0\mu m$ have the greatest scattering efficiency. Many pollutant airborne particles are in this size range. b_{ag} is light absorption by gases. Nitrogen dioxide (NO_2) is the only common atmospheric gaseous species that significantly absorbs light. b_{ap} is light absorption by particles. Absorption arises nearly entirely from elemental carbon particles.

The spectral distribution of the observe d solar irradiance at the earth surface is required in scientific and applied studies such as the radiative effects on various ecosystems and the interactions between environmental pollution and solar irradiance. The interactions have resultant impacts on atmospheric radiative energy transfer and

balance (Charlson et al., 1991, Adeyefa et al., 1997, Constantinos et al., 2000). The increase in aerosol loading in the atmosphere not only changes the environment but also modify the optical properties and lifetimes of clouds as cloud condensation nuclei CCN that in turn impacts global and regional climate. (Kiehl and Briegleb, 1993, Yunfeng et at., 2000). Atmospheric pollutants and aerosols absorb and scatter short wave radiation. Scattering and absorption of solar radiation by aerosol particles and trace gases result in considerable attenuation of surface solar radiation. Scattering moderately increases the diffuse component of solar radiation which at any instant however depend on other factors like the latitude, the sun declination angle, the watervapour in the atmosphere and the cloudiness of such location (Coppolino 1989). The clearness index CI, indicates the percentage depletion of incoming radiation by the sky while the diffuse ratio for the area under study is a quantity that mirrors the effectiveness of the sky in the scattering the incoming radiation (Ideriah & Suleman, 1989, Kuye & Japtap, 1992). It is well know fact that clouds determine the solar radiation received at the ground and other atmospheric constituent like aerosols and water vapor also affect the transmission of solar radiation.

The objectives of this study is to investigate the spectral distribution of solar radiation in North East Asia cities of Kwangju, Beijing and Ulaanbaatar and the extent to which changes in environmental factors affect this energy distribution. The accurate estimates of environmental and climatic effects due to aerosols mainly depend on the full understanding of its spatial and temporal distribution and good estimate of the atmospheric aerosol optical depth. Hence this study will further compute and compare the total atmospheric optical depths in North East Asia sites and investigate the distribution of the TOD and AOD at Kwangju, Beijing and Ulaanbaatar.

In many cases where a ground – based measurement of optical depth is required there exists neither the required resources nor the expertise to perform an accurate radiometric calibration of the sun photometer employed. The standard Langley plot technique for calibration is very susceptible to systematic errors related to atmospheric instability (Norman et al., 1989). Alternatively the Langley plot slope method, computed for the measurement acquired during the day to give an effective temporal average value of the optical depth over the measurement period has been used in this study. This long method solves the problem of logistical difficulties of absolute calibration.

The UV radiation constitutes very small portion of solar radiation, but it significantly affects on ecosystem as well as human health (e.g. cataracts, skin cancer). The ultraviolet radiation in the troposphere is referred to as radiation with wavelengths between about 290 and 400 nm. The UV radiation spectrum can be divided into three regions, named UV-A (315~400 nm) constituting most of the UV radiation received at the earth's surface, UV-B (280~315 nm) being partially absorbed or scattered in the atmosphere [*Al-Dhafiri et al., 2000*], and the most energetic UV-C (<280 nm) being completely absorbed by stratospheric ozone. Atmospheric ozone controls the amount of the most energetic ultraviolet radiation that reaches the troposphere, and total ozone amount and surface UV irradiance has an anticorrelation [*Cappellani et al.,* 2000 ; *Bais et al.,* 1997 ; *Bernhard et al.,* 1997 : *Weele,* 1996]. So, there has been a growing concern about increase in the surface UV radiation since ozone hole was observed in 1970s. While the largest changes in the surface UV radiation are due to the changes in the solar zenith angel, less is known about the impact by other parameters such as extraterrestrial solar radiation, cloud cover, extinction by aerosol [*Tsay et al.*, 1992], the thickness of the atmosphere expressed by surface pressure (Rayleigh scattering),

altitude, and surface reflectivity (albedo) [*Kylling et al.*, 1998 ; *Grobner et al.*, 2000 ; *Tsay et al.*, 1992]. Extraterrestrial solar radiation changes with Sun-Earth distance. Maximum and minimum values of extraterrestrial solar irradiance appear in January and July, respectively, because the Earth is at its closest point to the sun (perihelion) on approximately 3 January, and at its farthest point (aphelion) on approximately 4 July [*Iqbal*, 1983]. Clouds scatter incident radiation and reduce the irradiance reaching the Earth's surface [*Tsay et al.*, 1992]. Aerosol is important in that the size of aerosol is very similar to solar radiation wavelength.

Several studies have tried to investigate the effect of atmospheric aerosol on the surface UV radiation. *Kylling et al.* [1998] used measurement data and modeling results to investigate the effect of aerosol on UV irradiance by two instruments located at different two areas. The presence of aerosol is seen to reduce the UVB irradiance by a fraction ranging from 5% to 35% from the ratio between simulated UV spectra with and without aerosols. *Mayer et al.* [1997] studied the influence of several parameters such as aerosol on the ground level UV irradiance using spectral UV measurement and modeling results. Results of modeling without consideration of aerosol in the model input showed that the model clearly overestimated the measured results.

In this study the variation of the surface UV irradiance was monitorred the Northeast Asia (Korea, Japan, and Mongolia) to investigate the impact of aerosol amount on the surface UV irradiance at Kwangju, Korea. A simple statistical analysis of the data will be used to investigate the variability of surface UV irradiance due to atmospheric aerosol at Kwangju, Korea.

3. MEASUREMENT AND ANALYSIS

3. Measurement and Analysis

3.1 Chemical properties of atmospheric aerosols

In order to determine the chemical properties of atmospheric aerosol over the Northeast Asia, three intensive samplings were conducted at three measurement sites : Kwangju, Korea, Beijing, China, and Kyoto, Japan (Figure 3.1). Atmospheric aerosols were collected with a PM2.5 URG cyclone sampler and a MOUDI (Micro-Orifice Uniform Deposit Impactor) sampler during three intensive periods; 14~22 August, 30 October ~ 6 November 2000, and 14~21 January 2001.

The samples from each intensive sampling were analyzed by ion chromatography for ionic compound (Na^+, NH_4^+, K^+, Mg^{2+}, Ca^{2+}, Cl^-, NO_3^-, SO_4^{2-}) concentrations.

PM2.5 particles were collected on a teflon filter and a quartz filter at a flow rate of 16.7 liter per minute. After field sampling the collected particles on the filter were analyzed for anion compounds (Cl^-, NO_3^-, SO_4^{2-}) and cation compounds (Na^+, NH_4^+, K^+, Mg^{2+}, Ca^{2+}) using ion chromatography (IC). Aerosol samples collected on quartz filter were used for analysis of organic carbon (OC) and elemental carbon (EC).

For pretreatment of the teflon filter before sampling, the filters were exposed by clean air for 30 minutes and then were dried in a desiccator for 24 hours. After desiccating, the initial filter weight was measured. After sampling, the PM2.5 mass concentration was calculated by dividing the measured mass difference by the total sampled air volume. For pretreatment of 47mm diameter quartz filters, all were baked at a constant temperature of 550℃ for 12 hours. After baking the filters were placed in a clean room until they have been sealed into prepared petri dishes.

In order to extract the ionic compounds (Na^+, NH_4^+, K^+, Mg^{2+}, Ca^{2+}, Cl^-, NO_3^-,

SO_4^{2-}) from the Teflon filter collected particles were placed inside a vial. At first 1ml methanol was added onto the filter face uniformly and then 9ml ultra-pure water was added into vial. Additionally, 20μl of chloroform was also added to prevent chemical oxidation by microbes, Lastly, the vial containing the sample was systematically shaken for 30 minutes for complete extraction of ionic compounds.

Ionic compounds were analyzed by ion chromatography. The IONPAC AS4A-SC column was used for anion column and the IONPAC CS12 column was used for cation column. The anion eluent was 0.35 M Na_2CO_3 + 0.1 M $NaHCO_3$ with a flowrate of 2ml/min and cation eluent was 22mN H_2SO_4 with a flowrate of 1ml/min.

Carbon analyses were carried out at AtmmAA, Inc., Calabasas, CA, USA by the selective thermal oxidation method with a MnO_2 catalyst.

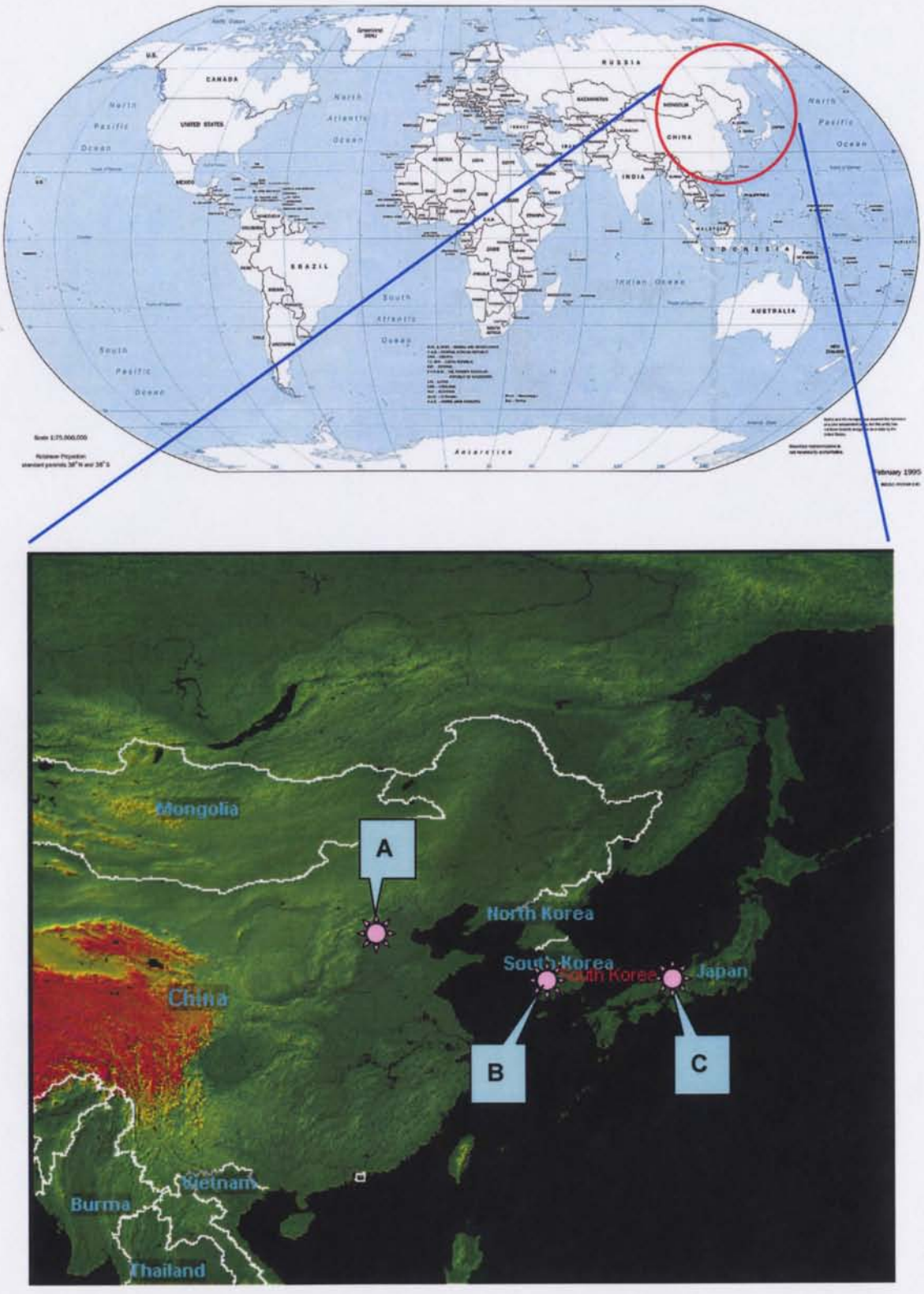

Figure 3.1 Area map of three sampling stations

(A) Beijing, China, (B) Kwangju, Korea (C) Kyoto, Japan

3.2 Optical properties of aerosols

Aerosol Monitoring

In this visibility monitoring at Kwangju, short-interval samplings were introduced for the special analysis for hourly variation of acidic aerosol and elemental carbon during day time (from 06:00 to 18:00) and diurnal-nocturnal variation of them through each 12-hour sampling interval with start times of 06:00 (diurnal) and 18:00 (nocturnal). 2000 summer visibility monitoring was carried out during the summer intensive sampling period, from July 12 to July 22, 1999. Aerosol monitoring data are used to determine the gravimetric mass and chemical composition of size differentiated particles and ionic concentration for the analysis of acidic aerosol (sulfate and nitrate) and artifacts caused by gas phase. URG-VAP sampler for aerosol monitoring has three sampling arms. As described below, two of the three arms and a cyclone collect fine particles with aerodynamic diameter $\leq 2.5\ \mu m$:

- A teflon filter is used first to fine mass, sulfate, nitrate and ammonium ions
- A quartz filter is used to measure organic and elemental carbon.

URG cyclone also employs a teflone filter pack with $2.5\mu m$ cut size. A teflon filter inserted into the cyclone was used to measure elements associated with sulfur compounds and soil. Fine particles with diameters less than 2.5 microns are especially efficient at scattering light. Another center arm collects coarse particles with aerodynamic diameters up to $10\mu m$, using a nuclepore filter. Coarse particles are less efficient light scatterers than $PM_{2.5}$ particles. Table 3.1 shows the aerosol sampling

condition in this study.

Table 3.1 Sampling methods and filter treatments for aerosol analysis.

Arms	Particle Size	Filter Type	Analytical Method
Right	0~2.5μm	Quartz (Whatman, 4.7cm)	• Thermal Manganese Oxidation Analysis (elemental & organic carbon)
Center	2.5~10μm	Nuclepore (Costa, 0.4μm, 47mm)	• Gravimetric Analysis (mass)
Left	0~2.5μm	Teflon (Gelman, 2μm, 47mm)	• Gravimetric Analysis (mass) • Ion Chromatography Analysis (sulfate, nitrate ions)
		Denuder (242mm, 150mm)	• Ion Chromatography Analysis (SO_2, HNO_3, NH_3 gas)
Cyclone	0~2.5μm	Teflon (Gelman, 2μm, 47mm)	• Gravimetric Analysis (mass) • Induced Couple Plasma Analysis (ICP/MS & ICP/AES: Elements Na – Pb)

Optical Monitoring

Optical monitoring provides a quantitative measure of ambient light extinction (light attenuation per unit distance) or its components to represent visibility conditions. optical monitoring at Kwangju collect continuous measures of extinction, scatter and absorption coefficients (b_{ext}, b_{scat} and b_{abs}) using a long-path transmissometer, a nephelometer and an aethalometer, respectively. Soot in the air may also affect the light absorption and is analyzed as elemental carbon, which is associated with black carbon concentration by aethalometer.

3.3 Radiative properties of aerosols

The solar radiation measurement station at Kwangju is located on the roof of the Material Environmental Science and Engineering building in the Kwangju Institute of Science and Technology (Lat.35°13'N, Long.126°53'E). Similar radiation stations were estabilished at Beijing and Ulaanbaatar for this study.RSR (Rotating Shadow band Radiometer) measures global radiation and diffuse radiation for the estimation of total atmospheric optical depth (TOD) at every 10 minutes since January 2000 at Kwangju, while measurements began October 2000 at Beijing (Lat39° 52' N, Long.123 ° 53'E) and Ulaanbaartar (Lat.47°55'N, Long.106 ° 55'E). The RSR sensors include a LI-190SA Quantum sensor, and a LI-200SA pyranomter sensor. Recalibration of the RSR is done as recommended by the manufacturer. The cosine correction error is less than ± 5% for angles less than 80° from the normal axis of the sensor and at 90 ° the cosine error is infinite.

Detailed information on the RSR equipment can be found from Kim et. al, (1995).

The direct normal solar irradiance is computed as

$$DNSI = (I_{max}-I_{min})/\cos\Phi$$

where DNSI is direct normal solar irradiance, I is the solar irradiance incident on the snesor, Φ is the solar zenith Angler . The total optical depth is computed using the Beer's law

$$I = G_0 \exp(-\tau m)$$

where G_o is the solar irradiance at top of atmosphere, I is the direct normal solar irradiance, τ *is the* total optical depth and m is the air mass. The relative optical air mass $2 < m = 1/\cos\Phi < 6$ for the solar zenith angle 60° ~ 80°. The total atmospheric aerosol optical depth is then computed by

$$\tau_{total} = \tau_{ozone} + \tau_{watervapor} + \tau_{Rayleigh} + \tau_{aerosol}$$

The clearness index CI is defined as G/G_o . G_o can be calculated as

$$G_o = 24/\pi\, I_{sc}E_o \sin\Phi \mathrm{Sin}\delta((\pi/180)w_s - \tan w_s)$$

where I_{sc} = solar constant, E_o = Eccentricity correction factor, Φ = station Latitude, δ = Declination angle or each day of the year, w_s = sunrise hour angle.

The diffuse ratio is given as D/G, where D is the diffuse radiation and G is the global radiation measured on a horizontal surface.

3.4 Surface UV radiation

The UV-S-B-T, and UV-S-A-T *(Scintec, Inc.)* for measuring UV-B and UV-A were

installed at the roof of the department of Material Science and Engineering building in the Kwangju Institute of Science and Technology (K-JIST) at Kwangju, Korea. These UV radiometers measure the integrated global UV irradiance at the wavelength of 280 to 315 nm and 315 to 400 nm, respectively. Measurement outputs from the UV sensors are sampled at every 15 seconds interval and averaged over a 1 minute interval and saved into the YESDAS (Yankee Environmental Systems) data logger.

UV measurements at Ulaanbaatar, Mongolia, was conducted by a UVB-1 radiometer (Yankee Environmental Systems) at the ground of Institute of Geoecology, Ministry of Nature and the Environment. This instrument measures the integrated global UV-B irradiance at the wavelength of 280 to 320 nm, and shares a CR10X (Campbell Scientific) data logger with the RSR system. Measurement outputs from the UV radiometer are sampled and recorded every 10 minutes as a mean value into the data logger.

A UV-B radiometer (EKO, MS-212W) was installed at Kyoto University at Kyoto, Japan to measure the integrated global UV-B radiation (280 – 315 nm) every 10 minutes interval and record it into a data logger.

The measured data are averaged each hour to investigate the diurnal variation. Mean value of UV irradiance was computed for each month. The UV radiation measurements were taken under all sky conditions. This study uses the UVB and UVA data obtained during the period form Feb to Nov 2000 at Kwangju, UVB data from Oct to Dec 2000 at Ulaanbaatar, and UVB data from Nov to Dec 2000 at Kyoto.

In chapter 4.3 aerosol optical depth (AOD) values in visible wavelength range were calculated. AOD indicates the total amount of aerosol in the column atmosphere and is related to radiative forcing of aerosols in the atmosphere [*Kim et al.* 2000]. Atmospheric

aerosols attenuate ultraviolet radiation as well as solar radiation at other wavelength ranges. Correlations between UV radiation and AOD in the visible region was analyzed inthis study to investigate the atmospheric aerosols' impaction on the surface UV irradiance.

The regression analysis for AOD determination is performed only for relative optical air mass range between 2 and 6. Lower air masses are excluded because the rate of change of the optical air mass is too small creating a greater opportunity for changing atmospheric conditions to affect the regression. Air mass over 6 is avoided because of the greater uncertainty in air mass caused by refractions that are increasingly sensitive to atmospheric temperature profile [*Harrison et al.*, 1994 ; *Min,* 2000].

Relationship between AOD and UV irradiance was investigated by scatter plots at 60°, 70°, and 80° of solar zenith angle. All regressio analysis was done for clear-sky condition valyes since our AOD values were calculated under clear-sky conditions.

4. RESULTS AND DISCUSSION

4. Results and Discussion

4.1 Chemical properties of aerosols

4.1.1 Particulate ionic and mass concentrations

Three intensive sampling of aerosols were conducted during three seasons; summer (14~22 August 2000), fall (30.October ~ 6 November 2000), and winter (14~21 January 2001) at the three measurement sites ; Kwangju, Kyoto, and Beijing.

Table 4.1.1 summarizes the mean concentrations of mass and ionic compound concentrations from the 1st to 3rd intensive samplings of aerosols over the three stations.

Concentrations of mass and ionic compounds increased in winter. At Beijing, China, three major ions ; SO_4^{2-}, NH_4^+ and NO_3^- have the mean concentrations of 15.75, 5.82, and 5.60 μg/m^3 in summer ; 18.78, 8.45, and 17.41 μg/m^3 in fall, and 57.92, 16.85, and 30.12 μg/m^3 in winter,respectively. At Kwangju, Korea, three major ions, SO_4^{2-}, NH_4^+ and NO_3^- have the mean concentrations 3.22 , 2.69 , and 0.63 μg/m^3 in summer ; 3.13, 3.70, and 4.56 μg/m^3 in fall, 6.15, 4.58, and 2.11 μg/m^3 in winter. At Kyoto, Japan, three major ions, SO_4^{2-}, NH_4^+ and NO_3^- have the mean concentrations 7.07, 3.39, and 0.19 μg/m^3 in summer ; 4.29, 2.27, and 0.55 μg/m^3 in fall, 3.50, 2.74, and 0.75 μg/m^3 in winter (Figure 4.1.2)

The mean concentrations of PM 2.5 particles during the three intensive samplings were measured to be 67.5, 172.4 and 225.3 μg/m^3 at Beijing, 21.4, 17.1, and 33.6 μg/m^3 at Kwangju, and 16.1, 40.4 and 17.5 μg/m^3 at Kyoto, respectively

(Figure 4.1.1).

The results of Pearson correlation were presented in Tables 4.1.2 ~ 4.1.4. From these results the correlation values between NH_4^+ and SO_4^{2-}, and NH_4^+ and NO_3^- are higher than other correlation values. The measurement data indicated that particulate ammonium sulfate and ammonium nitrate were formed in the atmosphere. It can be concluded that ammonium sulfate ($(NH_4)_2SO_4$) is the major pollutant component in PM2.5 and secondly ammonium nitrate (NH_4NO_3).

Table 4.1.1 Mean concentration of ionic compounds from 1st to 3rd intensive sampling of aerosol over three countries.

($\mu g/m^3$)

Sampling periods	Stations	Cl^-	NO_3^-	SO_4^{2-}	Na^+	NH_4^+	K^+	Mg^{2+}	Ca^{2+}
1st (14~22 August 2000)	Beijing, China	0.905	5.601	15.753	0.198	5.824	1.374	0.179	1.202
	Kwangju, Korea	0.045	0.629	3.2236	0.102	2.686	0.013	0.007	0.003
	Kyoto, Japan	0.026	0.188	7.066	0.093	3.392	0.066	0.015	0.014
2nd (30~6 November 2000)	Beijing, China	5.000	17.405	18.784	0.632	8.447	2.319	0.334	2.834
	Kwangju, Korea	0.482	4.555	3.132	0.251	3.704	0.412	0.054	0.144
	Kyoto, Japan	0.059	0.548	4.292	0.186	2.274	0.096	0.015	0.031
3rd (14~21 January 2001)	Beijing, China	5.203	30.117	57.917	1.735	16.851	2.747	0.194	0.876
	Kwangju, Korea	0.995	2.106	6.150	0.318	4.581	0.211	0.029	0.129
	Kyoto, Japan	0.406	0.750	3.499	0.275	2.738	0.121	0.018	0.053

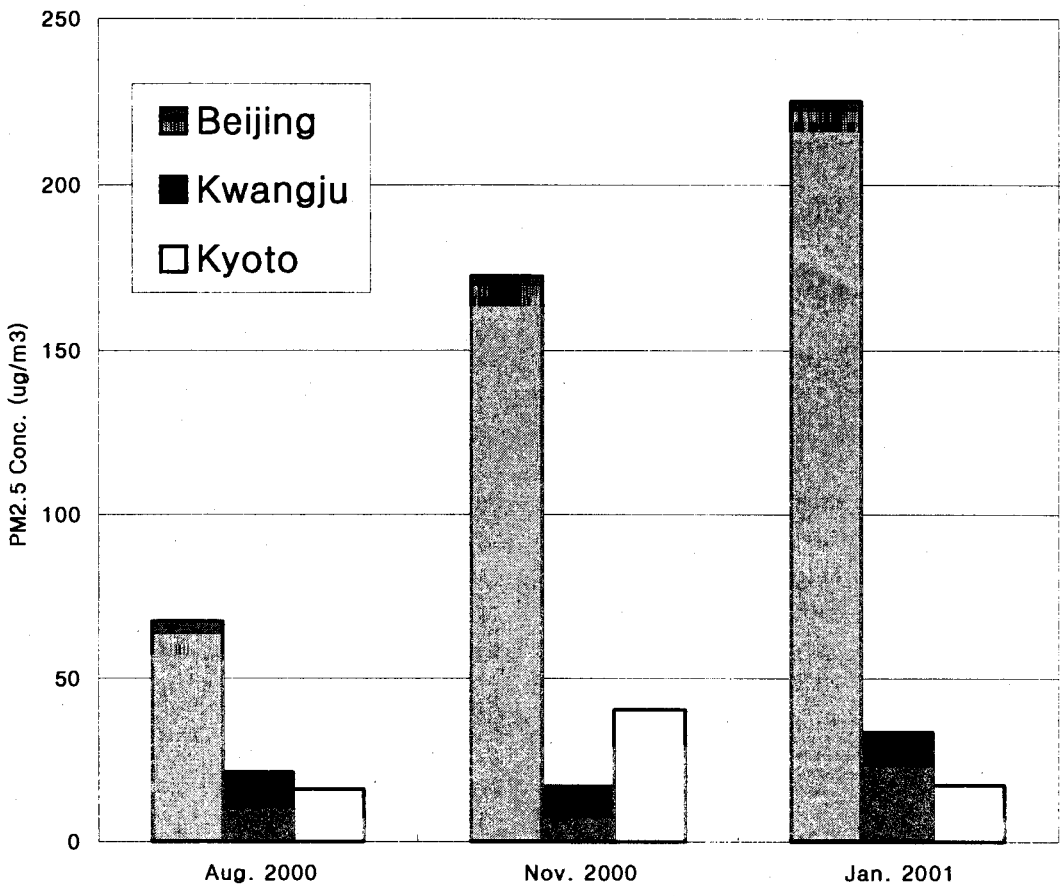

Figure 4.1.1 Mean PM 2.5 Mass concentrations during three intensive sampling periods

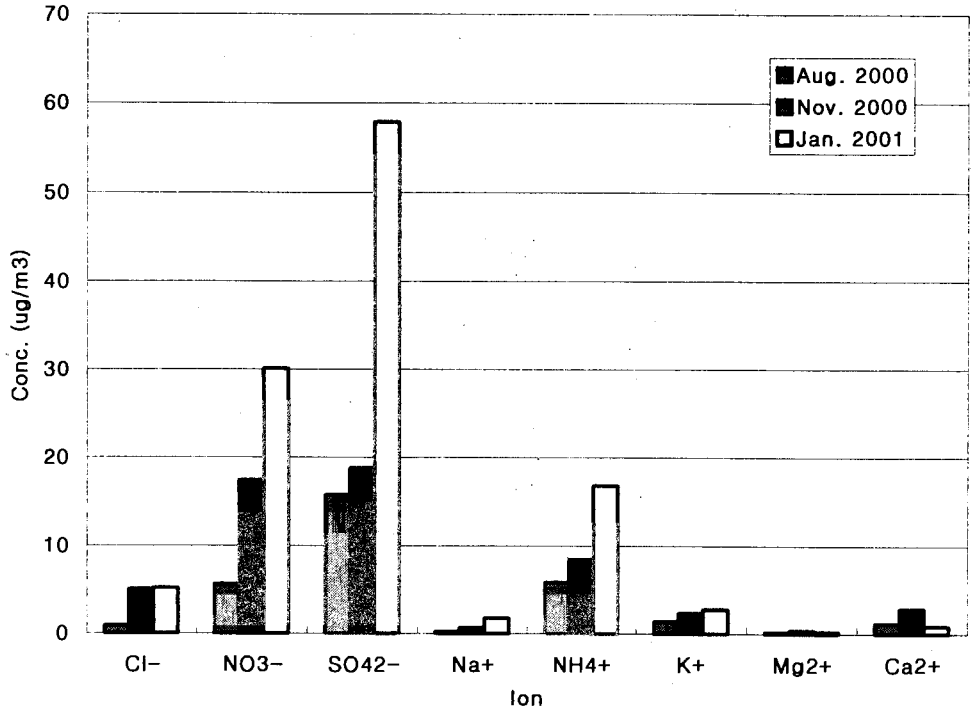

(a) Beijing

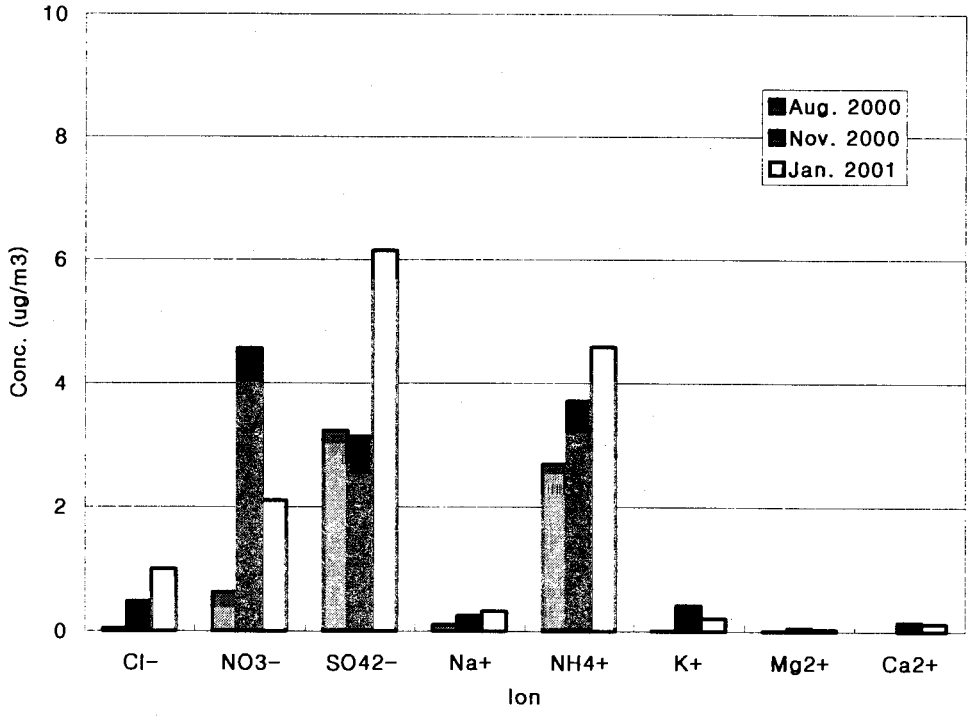

(b) Kwangju

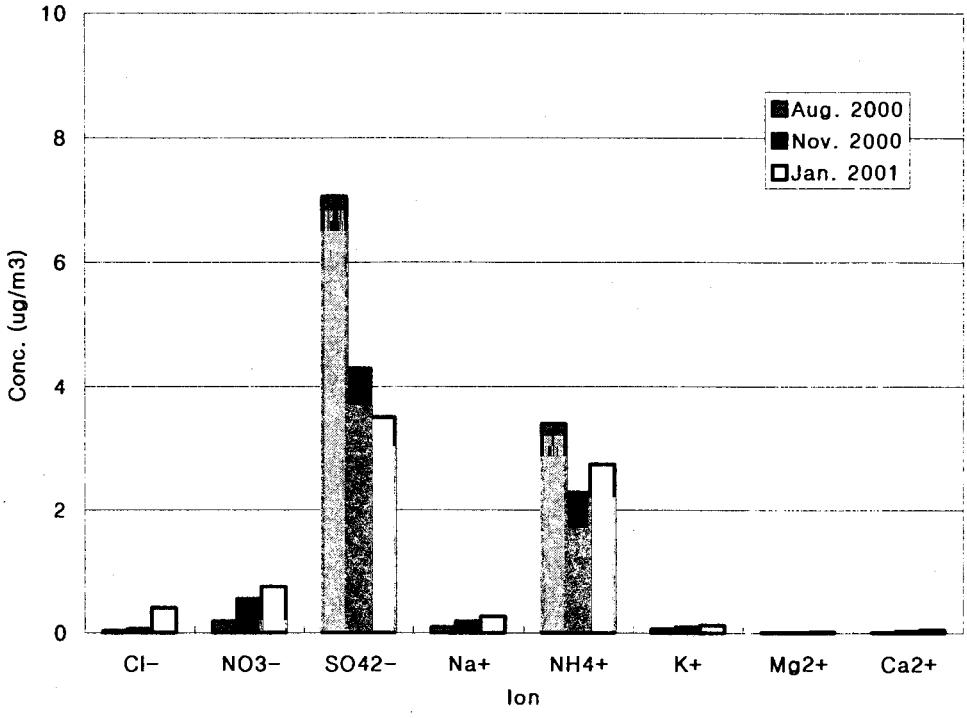

(c) Kyoto

Figure 4.1.2 Mean PM 2.5 Ion concentrations at (a) Beijing, China (b) Kwangju, Korea and (c) Kyoto, Japan during three intensive sampling period

Table 4.1.2 Pearson correlation matrix for ion compounds for the 1st intensive sampling period

Beijing	Cl^-	NO_3^-	SO_4^{2-}	Na^+	NH_4^+	K^+	Mg^{2+}	Ca^{2+}
Cl^-	1.000	0.645	0.167	0.873	0.462	0.317	0.754	0.712
NO_3^-		1.000	0.462	0.788	0.771	0.502	0.681	0.671
SO_4^{2-}			1.000	0.079	0.899	0.827	0.414	0.606
Na^+				1.000	0.399	0.344	0.834	0.698
NH_4^+					1.000	0.791	0.563	0.745
K^+						1.000	0.669	0.872
Mg^{2+}							1.000	0.881
Ca^{2+}								1.000

Kwangju	Cl^-	NO_3^-	SO_4^{2-}	Na^+	NH_4^+	K^+	Mg^{2+}	Ca^{2+}
Cl^-	1.000	0.703	0.650	0.407	0.743	-0.133	0.241	0.165
NO_3^-		1.000	0.643	-0.187	0.519	-0.378	-0.274	-0.406
SO_4^{2-}			1.000	0.264	0.867	0.433	0.383	0.252
Na^+				1.000	0.662	0.300	0.930	0.934
NH_4^+					1.000	0.286	0.664	0.562
K^+						1.000	0.599	0.581
Mg^{2+}							1.000	0.974
Ca^{2+}								1.000

Kyoto	Cl^-	NO_3^-	SO_4^{2-}	Na^+	NH_4^+	K^+	Mg^{2+}	Ca^{2+}
Cl^-	1.000	0.038	-0.334	-0.009	-0.441	-0.086	0.355	-0.042
NO_3^-		1.000	0.036	-0.171	0.146	0.334	-0.003	-0.235
SO_4^{2-}			1.000	0.355	0.952	0.069	-0.589	0.688
Na^+				1.000	0.464	0.405	0.453	-0.074
NH_4^+					1.000	0.203	-0.515	0.469
K^+						1.000	0.309	0.031
Mg^{2+}							1.000	-0.582
Ca^{2+}								1.000

Table 4.1.3 Pearson correlation matrix for ion compounds for the 2nd intensive sampling period

Beijing	Cl^-	NO_3^-	SO_4^{2-}	Na^+	NH_4^+	K^+	Mg^{2+}	Ca^{2+}
Cl^-	1.000	0.849	0.861	0.817	0.886	0.797	0.941	0.839
NO_3^-		1.000	0.959	0.401	0.995	0.981	0.743	0.607
SO_4^{2-}			1.000	0.446	0.961	0.955	0.690	0.574
Na^+				1.000	0.475	0.320	0.861	0.836
NH_4^+					1.000	0.962	0.784	0.642
K^+						1.000	0.684	0.593
Mg^{2+}							1.000	0.947
Ca^{2+}								1.000

Kwangju	Cl^-	NO_3^-	SO_4^{2-}	Na^+	NH_4^+	K^+	Mg^{2+}	Ca^{2+}
Cl^-	1.000	0.355	-0.232	0.462	0.325	0.817	0.325	0.033
NO_3^-		1.000	-0.551	-0.078	0.483	0.319	0.375	-0.280
SO_4^{2-}			1.000	0.476	0.334	-0.029	-0.076	0.516
Na^+				1.000	0.202	0.597	0.525	0.755
NH_4^+					1.000	0.244	-0.050	-0.170
K^+						1.000	0.754	0.419
Mg^{2+}							1.000	0.661
Ca^{2+}								1.000

Kyoto	Cl^-	NO_3^-	SO_4^{2-}	Na^+	NH_4^+	K^+	Mg^{2+}	Ca^{2+}
Cl^-	1.000	0.252	-0.613	-0.357	-0.552	0.178	-0.113	-0.142
NO_3^-		1.000	0.180	0.534	0.352	0.349	0.536	0.204
SO_4^{2-}			1.000	0.846	0.962	0.458	0.795	0.810
Na^+				1.000	0.817	0.443	0.915	0.798
NH_4^+					1.000	0.500	0.786	0.746
K^+						1.000	0.754	0.707
Mg^{2+}							1.000	0.913
Ca^{2+}								1.000

Table 4.1.4 Pearson correlation matrix for ion compounds for the 3rd intensive sampling period

Beijing	Cl^-	NO_3^-	SO_4^{2-}	Na^+	NH_4^+	K^+	Mg^{2+}	Ca^{2+}
Cl^-	1.000	0.129	0.148	0.143	0.359	0.265	-0.155	0.079
NO_3^-		1.000	0.967	0.969	0.967	0.915	0.805	0.451
SO_4^{2-}			1.000	0.972	0.965	0.972	0.864	0.387
Na^+				1.000	0.953	0.971	0.904	0.232
NH_4^+					1.000	0.949	0.748	0.429
K^+						1.000	0.888	0.193
Mg^{2+}							1.000	-0.054
Ca^{2+}								1.000

Kwangju	Cl^-	NO_3^-	SO_4^{2-}	Na^+	NH_4^+	K^+	Mg^{2+}	Ca^{2+}
Cl^-	1.000	0.740	0.440	0.134	0.791	0.830	0.700	0.319
NO_3^-		1.000	0.913	0.705	0.995	0.977	0.910	0.847
SO_4^{2-}			1.000	0.860	0.883	0.842	0.867	0.964
Na^+				1.000	0.643	0.600	0.647	0.882
NH_4^+					1.000	0.987	0.921	0.814
K^+						1.000	0.880	0.778
Mg^{2+}							1.000	0.819
Ca^{2+}								1.000

Kyoto	Cl^-	NO_3^-	SO_4^{2-}	Na^+	NH_4^+	K^+	Mg^{2+}	Ca^{2+}
Cl^-	1.000	0.503	0.115	0.629	0.464	0.155	0.223	0.376
NO_3^-		1.000	0.296	0.503	0.598	0.194	0.093	0.571
SO_4^{2-}			1.000	0.624	0.901	0.883	0.902	0.726
Na^+				1.000	0.711	0.759	0.737	0.859
NH_4^+					1.000	0.732	0.778	0.784
K^+						1.000	0.910	0.657
Mg^{2+}							1.000	0.727
Ca^{2+}								1.000

4.1.2 Seasonal variation of ion compounds

Figure 4.1.3 shows the seasonal variation of sulfate, nitrate and ammonium ion concentrations. In general it can be seen that NO_3^-, SO_4^{2-} and NH_4^+ showed similar variations for each season. The measurement data indicated that particulate ammonium sulfate or ammonium nitrate was formed in the atmosphere.

Results from the Pearson correlation matrix calculations for the three intensive sampling periods as shown in Table 4.1.2~4.1.4, the correlation values between NH_4^+ and SO_4^{2-}, and NH_4^+ and NO_3^- are higher than other correlation values.

Since potassium has a high correlation values with Cl^-, NO_3^-, SO_4^{2-} and NH_4^+, it can be considered to be related to similar sized particles. Although calcium usually belongs to large size particle, the correlation values were associated with smaller size particles of Cl., SO_4^{2-}, NH_4^+ and K^+ were higher than associated large particles of Mg_2^+ and Na^+. It can be transported from the same origins.

4.1.3 Back-trajectory analysis

Air mass backward trajectories were calculated using the Hybrid Single-Particle Lagrangian Trajectory (HYsplit) model for the three intensive sampling periods (1^{st} : 14~22 August 2000, 2^{nd} : 30.October ~ 6 November 2000, and 3^{rd} : 14~21 January 2001). The trajectories, which reflect the large-scale atmospheric transport characteristics of air mass arriving at the sampling sites, are useful for estimating the long-range transport of pollutants and other chemical species. It equally provided a better understanding of the airflow patterns in this region. The patterns of the long-

range transport to sampling sites based on analysis of 3-day (72hr) backward trajectories are presented in Figure 4.1.4 ~ 4.1.12).

The maximum values of SO_4^{2-}, NH_4^+ and NO_3^- at Beijing during the 1st intensive sampling period occurred on August 16th, 2000 and the lowest value on August 20th, 2000, respectively. Therefore, it can be concluded that air mass on August 17th at 10 AM local time transported from western part of China carried much more pollutants than that on August 21th at 10 AM local time 2000 transported from northern part of China. Back-trajectory results also showed that pollutant concentrations depend on the pathways of the air mass (Figure 4.1.4 ~ Figure 4.1.12). The transport of dust over the Northeast Asia was simulated by the HYsplit back-trajectory program. The Asian dust particles transported from China or Mongolia can affect the atmospheric composition over the Northeast Asia in spring.

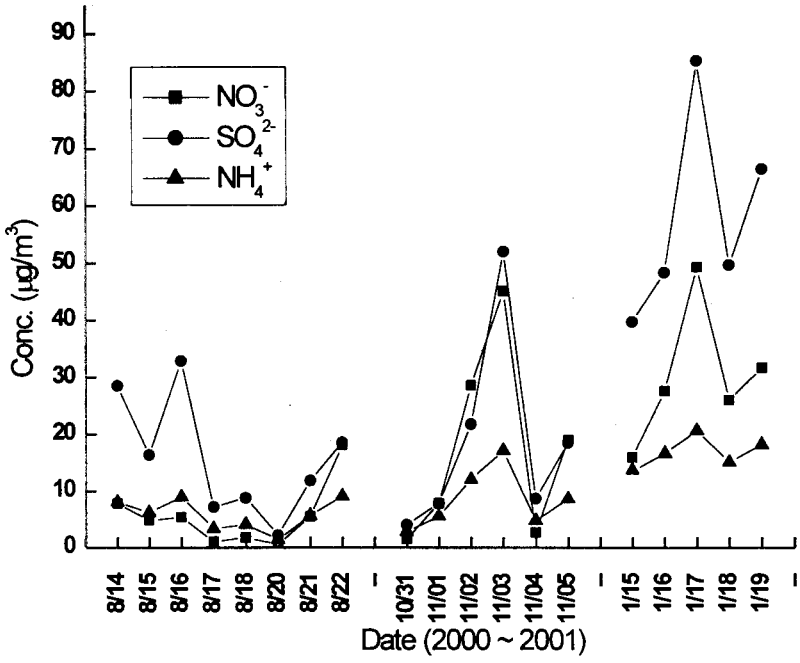

(a) Beijing, China

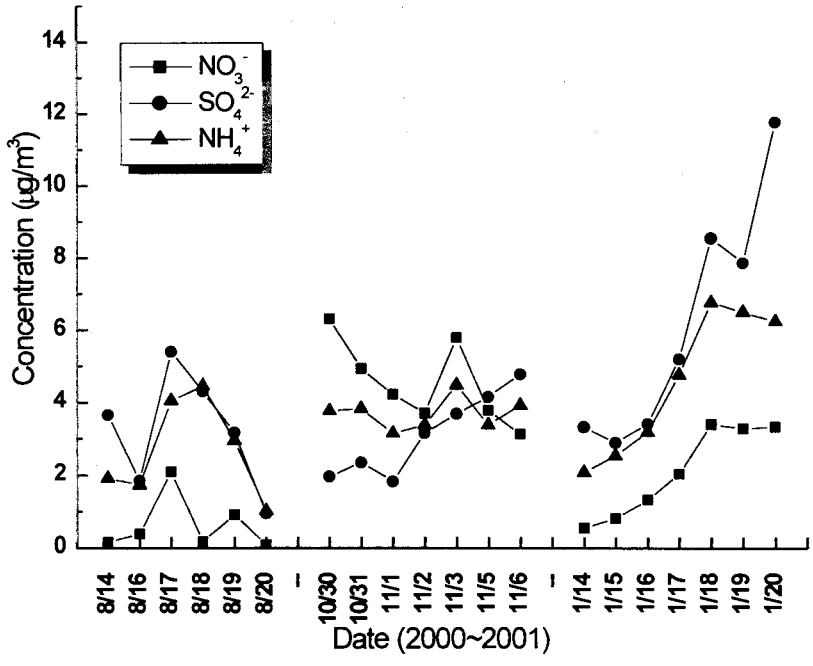

(b) Kwangju, Korea

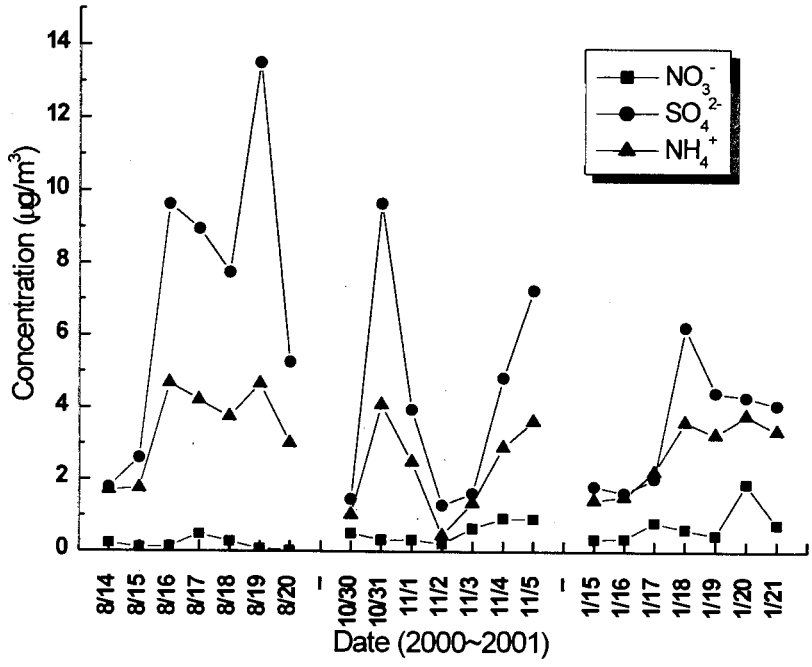

(c) Kyoto, Japan

Figure 4.1.3 Daily variation of nitrate, sulfate, ammonium ion concentrations in (a) Beijing, China (b) Kwangju, Korea, and (c) Kyoto, Japan.

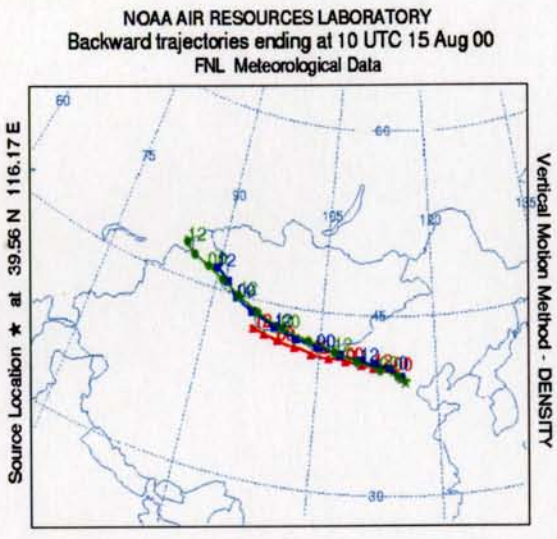
NOAA AIR RESOURCES LABORATORY
Backward trajectories ending at 10 UTC 15 Aug 00
FNL Meteorological Data
Source Location ★ at 39.56 N 116.17 E
Vertical Motion Method - DENSITY

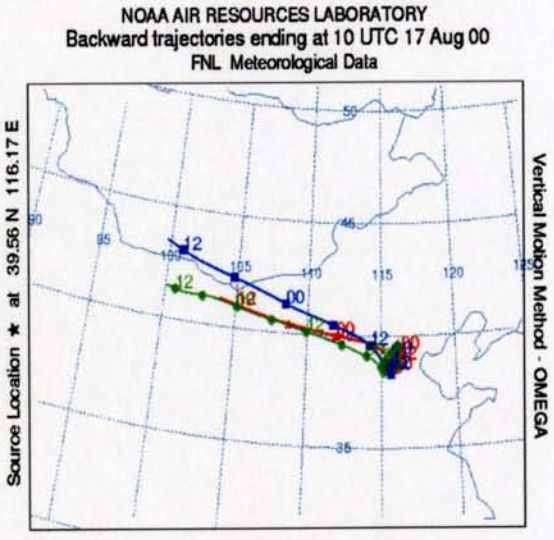
NOAA AIR RESOURCES LABORATORY
Backward trajectories ending at 10 UTC 17 Aug 00
FNL Meteorological Data
Source Location ★ at 39.56 N 116.17 E
Vertical Motion Method - OMEGA

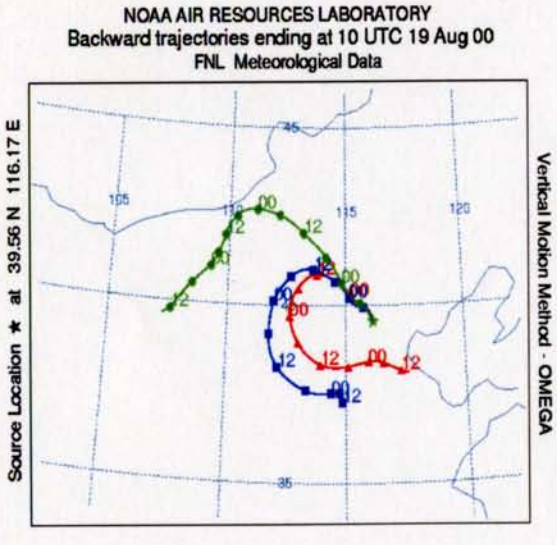
NOAA AIR RESOURCES LABORATORY
Backward trajectories ending at 10 UTC 19 Aug 00
FNL Meteorological Data
Source Location ★ at 39.56 N 116.17 E
Vertical Motion Method - OMEGA

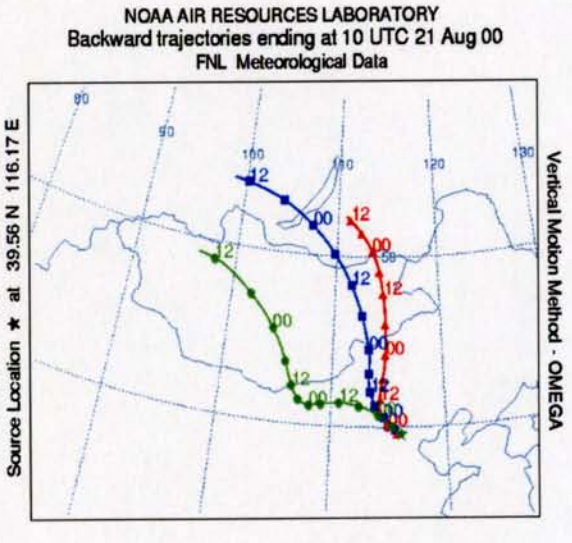
NOAA AIR RESOURCES LABORATORY
Backward trajectories ending at 10 UTC 21 Aug 00
FNL Meteorological Data
Source Location ★ at 39.56 N 116.17 E
Vertical Motion Method - OMEGA

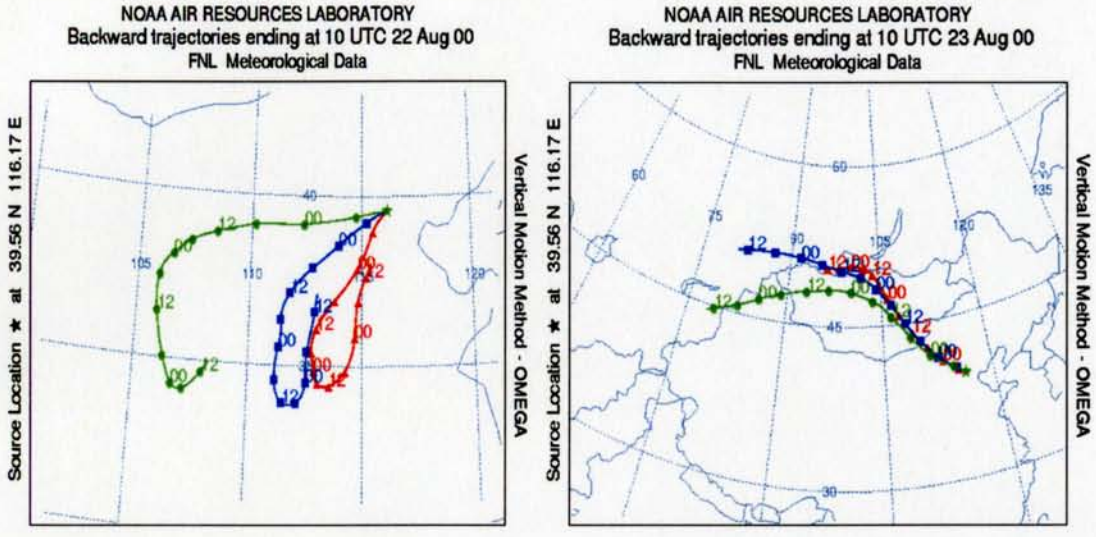

Figure 4.1.4 The distribution of back-trajectories pattern at 1500m, 2000m, 3000m in Beijing, China during the 1st sampling period (14~22 August 2000).

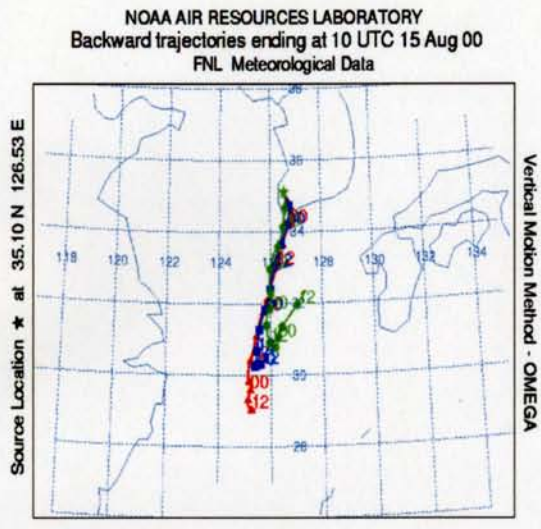
NOAA AIR RESOURCES LABORATORY
Backward trajectories ending at 10 UTC 15 Aug 00
FNL Meteorological Data
Source Location ★ at 35.10 N 126.53 E
Vertical Motion Method - OMEGA

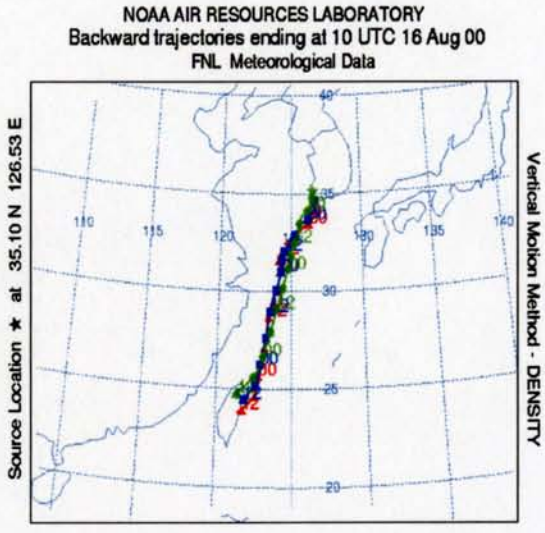
NOAA AIR RESOURCES LABORATORY
Backward trajectories ending at 10 UTC 16 Aug 00
FNL Meteorological Data
Source Location ★ at 35.10 N 126.53 E
Vertical Motion Method - DENSITY

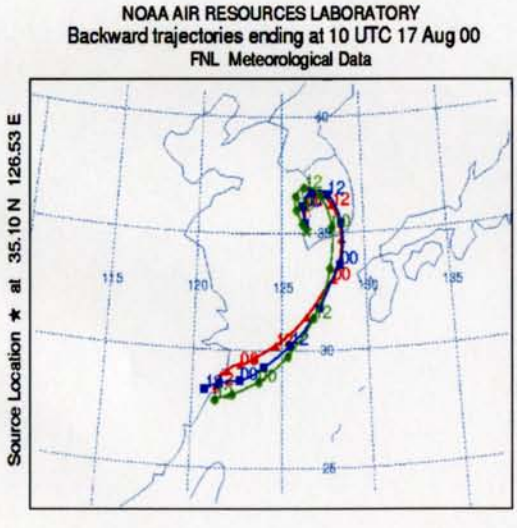
NOAA AIR RESOURCES LABORATORY
Backward trajectories ending at 10 UTC 17 Aug 00
FNL Meteorological Data
Source Location ★ at 35.10 N 126.53 E
Vertical Motion Method - DENSITY

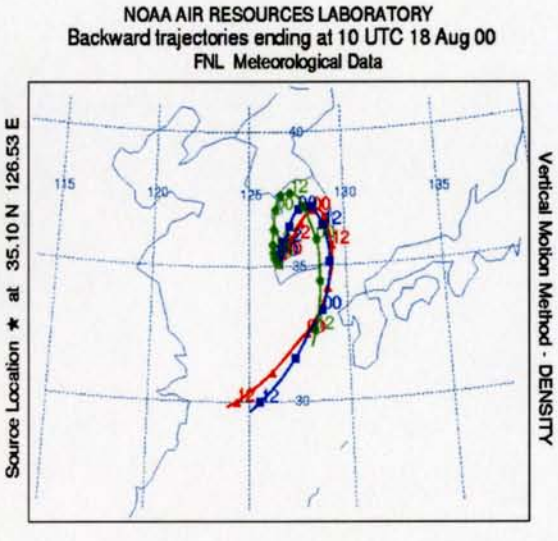
NOAA AIR RESOURCES LABORATORY
Backward trajectories ending at 10 UTC 18 Aug 00
FNL Meteorological Data
Source Location ★ at 35.10 N 126.53 E
Vertical Motion Method - DENSITY

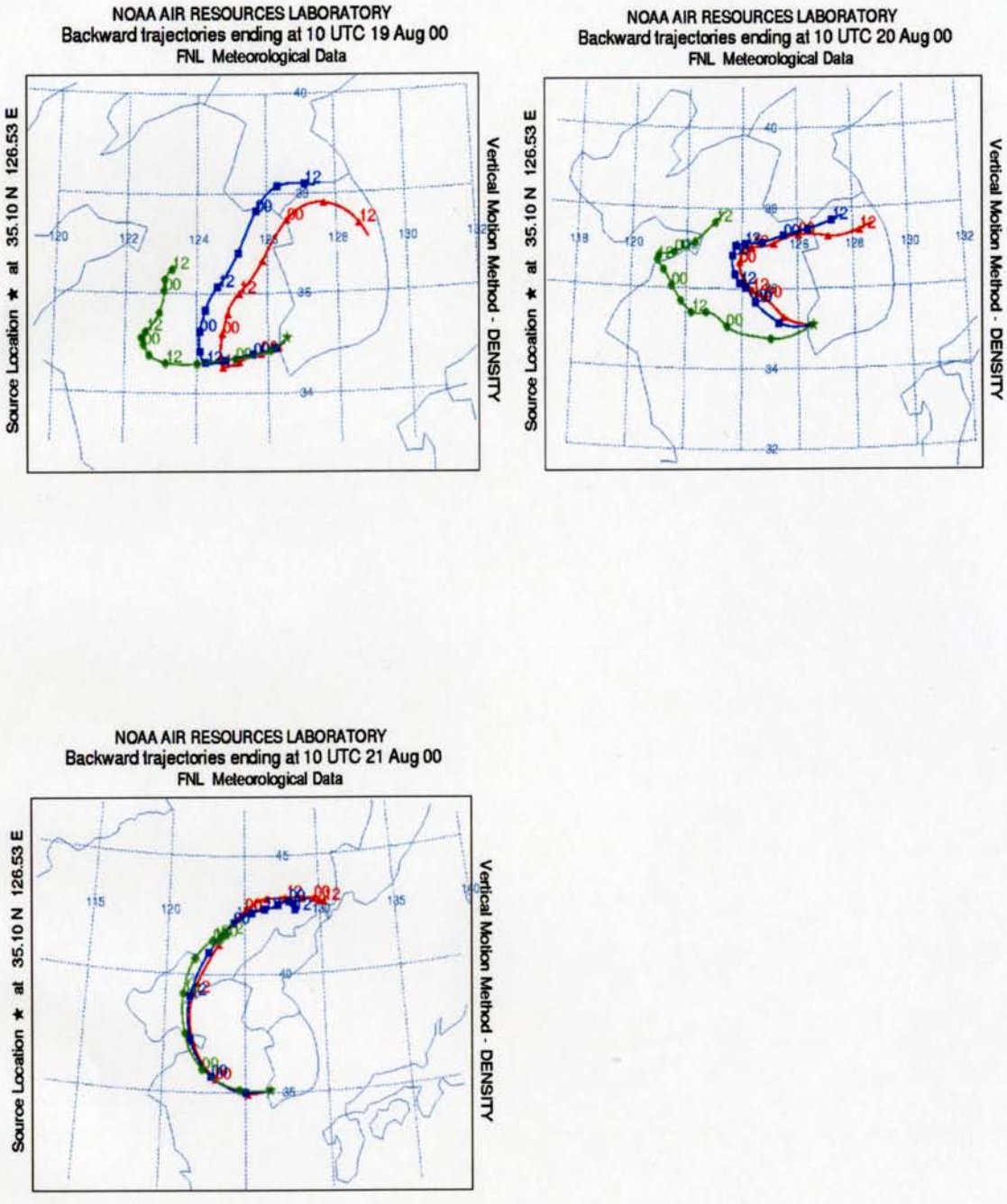

Figure 4.1.5 The distribution of back-trajectories pattern at 1500m, 2000m, 3000m in Kwangju, Korea during the 1st sampling period (14~22 August 2000).

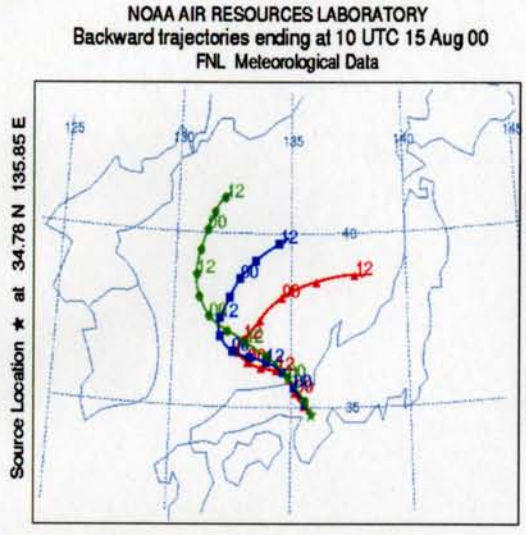
NOAA AIR RESOURCES LABORATORY
Backward trajectories ending at 10 UTC 15 Aug 00
FNL Meteorological Data
Source Location ★ at 34.78 N 135.85 E
Vertical Motion Method - OMEGA

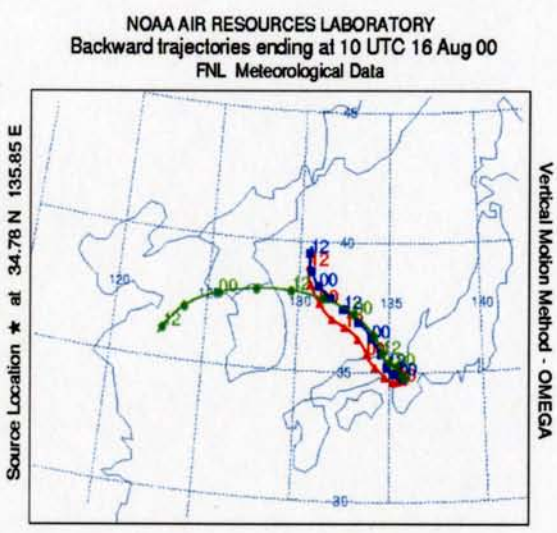
NOAA AIR RESOURCES LABORATORY
Backward trajectories ending at 10 UTC 16 Aug 00
FNL Meteorological Data
Source Location ★ at 34.78 N 135.85 E
Vertical Motion Method - OMEGA

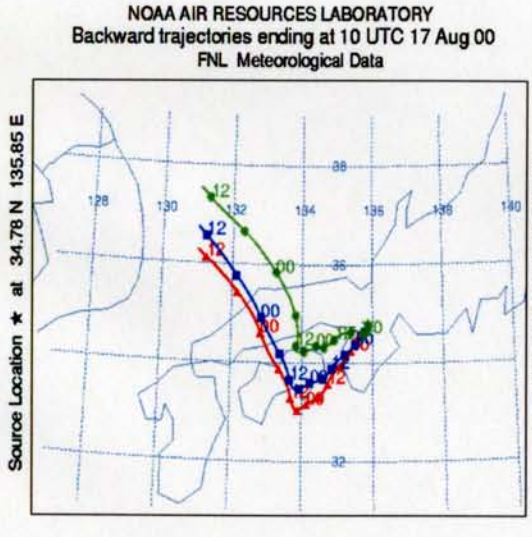
NOAA AIR RESOURCES LABORATORY
Backward trajectories ending at 10 UTC 17 Aug 00
FNL Meteorological Data
Source Location ★ at 34.78 N 135.85 E
Vertical Motion Method - OMEGA

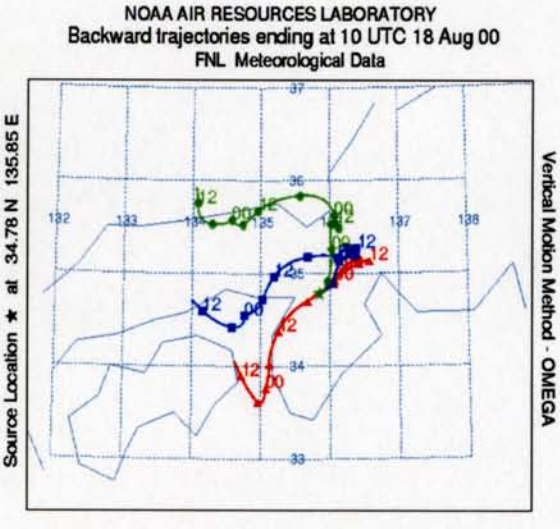
NOAA AIR RESOURCES LABORATORY
Backward trajectories ending at 10 UTC 18 Aug 00
FNL Meteorological Data
Source Location ★ at 34.78 N 135.85 E
Vertical Motion Method - OMEGA

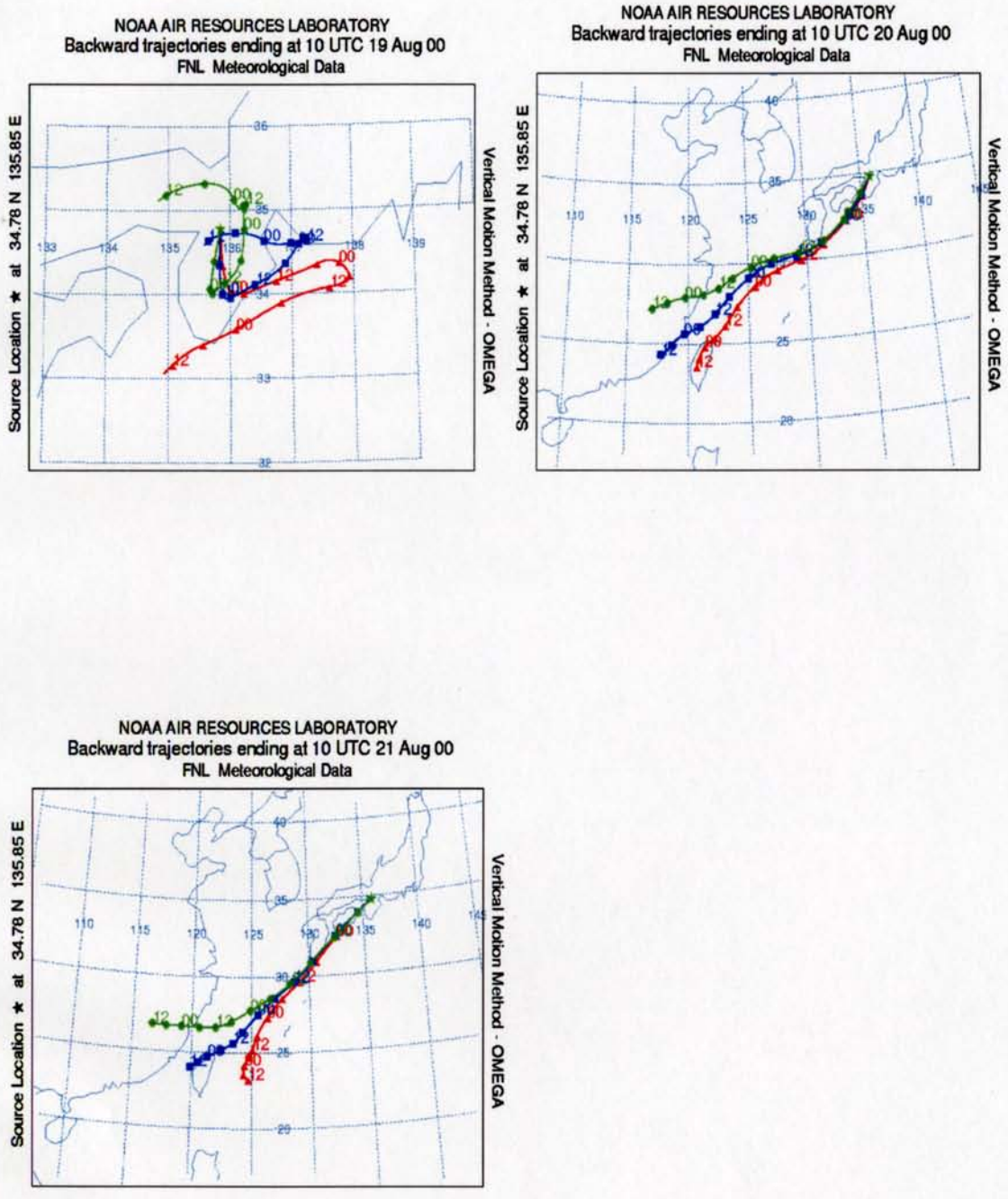

Figure 4.1.6 The distribution of back-trajectories pattern at 1500m, 2000m, 3000m in Kyoto, Japan during the 1st sampling period (14~22 August 2000).

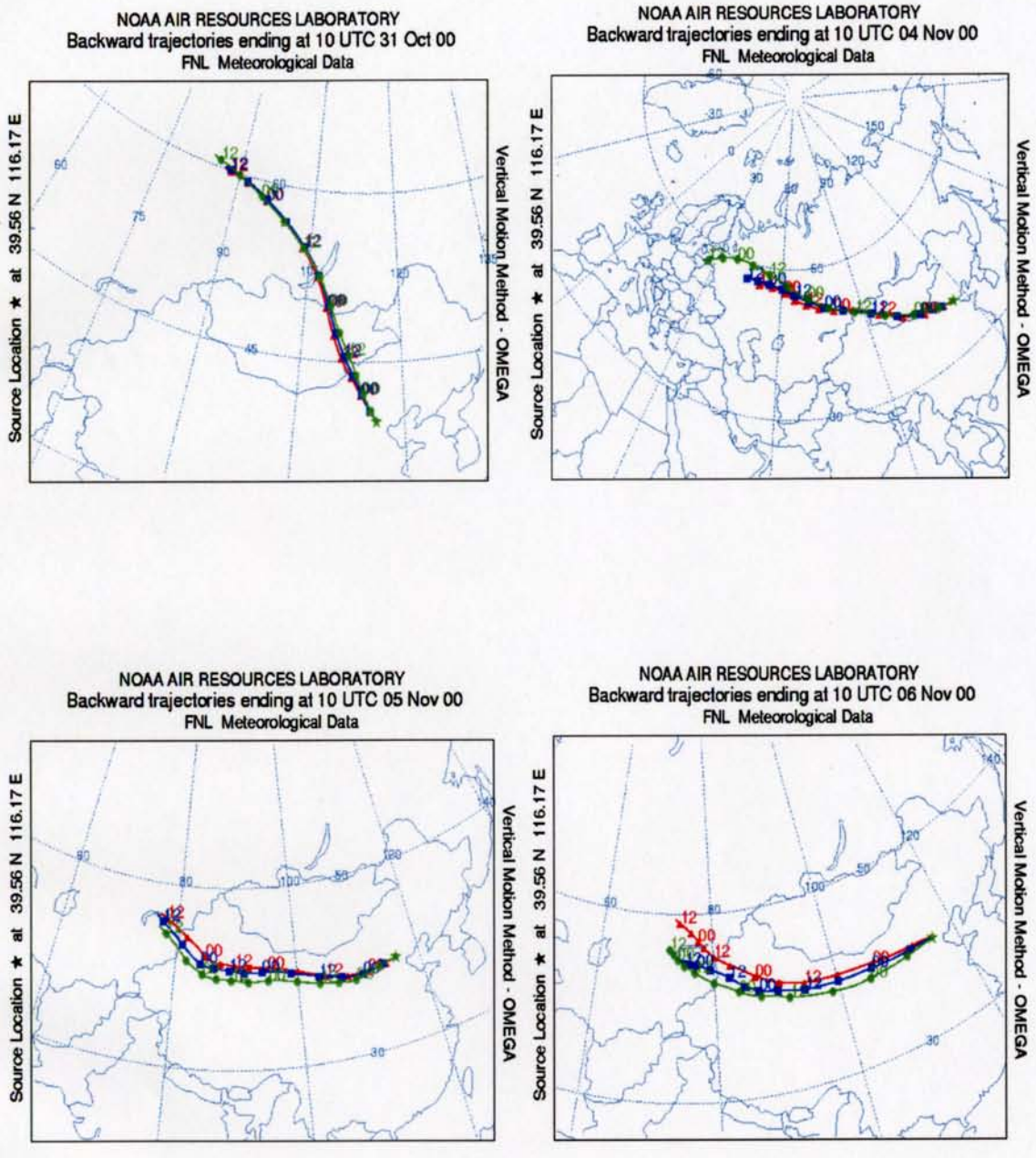

Figure 4.1.7 The distribution of back-trajectories pattern at 1500m, 2000m, 3000m in Beijing, China during the 2nd sampling period (30.October ~ 6 November 2000).

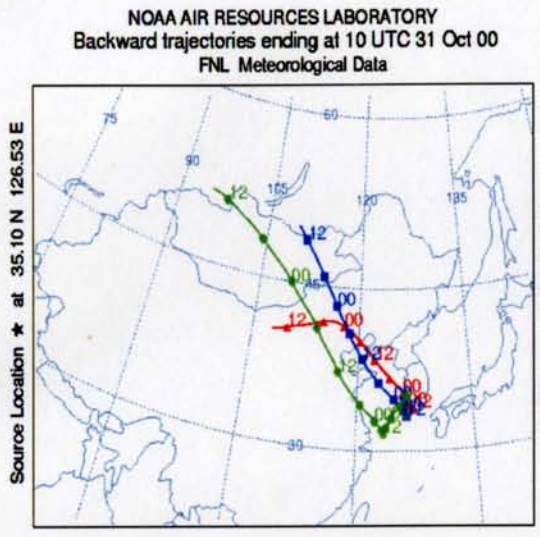
NOAA AIR RESOURCES LABORATORY
Backward trajectories ending at 10 UTC 31 Oct 00
FNL Meteorological Data
Source Location ★ at 35.10 N 126.53 E
Vertical Motion Method - OMEGA

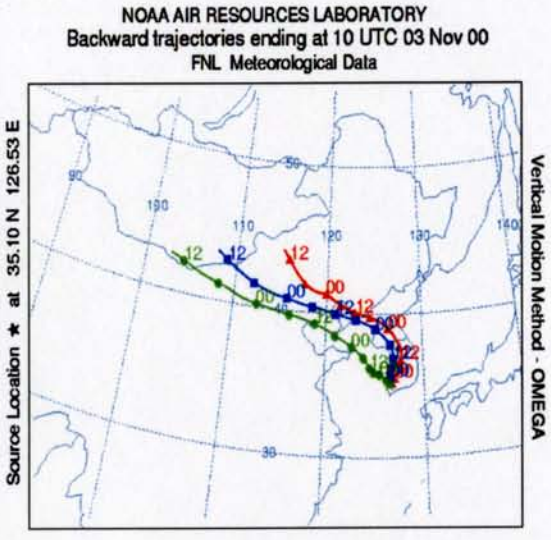
NOAA AIR RESOURCES LABORATORY
Backward trajectories ending at 10 UTC 03 Nov 00
FNL Meteorological Data
Source Location ★ at 35.10 N 126.53 E
Vertical Motion Method - OMEGA

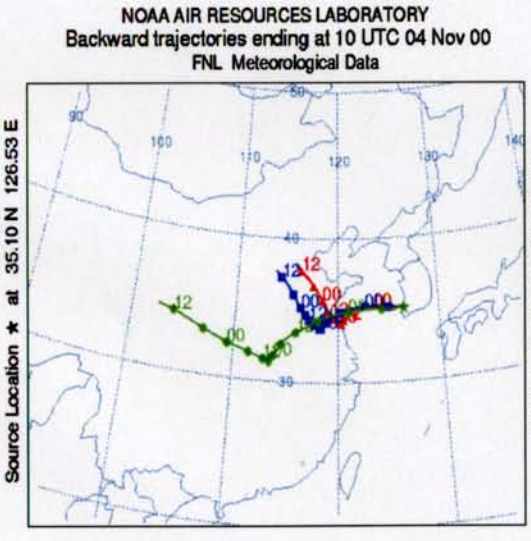
NOAA AIR RESOURCES LABORATORY
Backward trajectories ending at 10 UTC 04 Nov 00
FNL Meteorological Data
Source Location ★ at 35.10 N 126.53 E
Vertical Motion Method - OMEGA

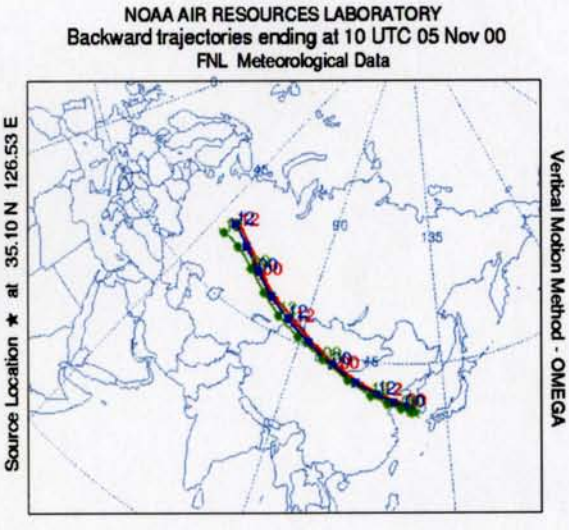
NOAA AIR RESOURCES LABORATORY
Backward trajectories ending at 10 UTC 05 Nov 00
FNL Meteorological Data
Source Location ★ at 35.10 N 126.53 E
Vertical Motion Method - OMEGA

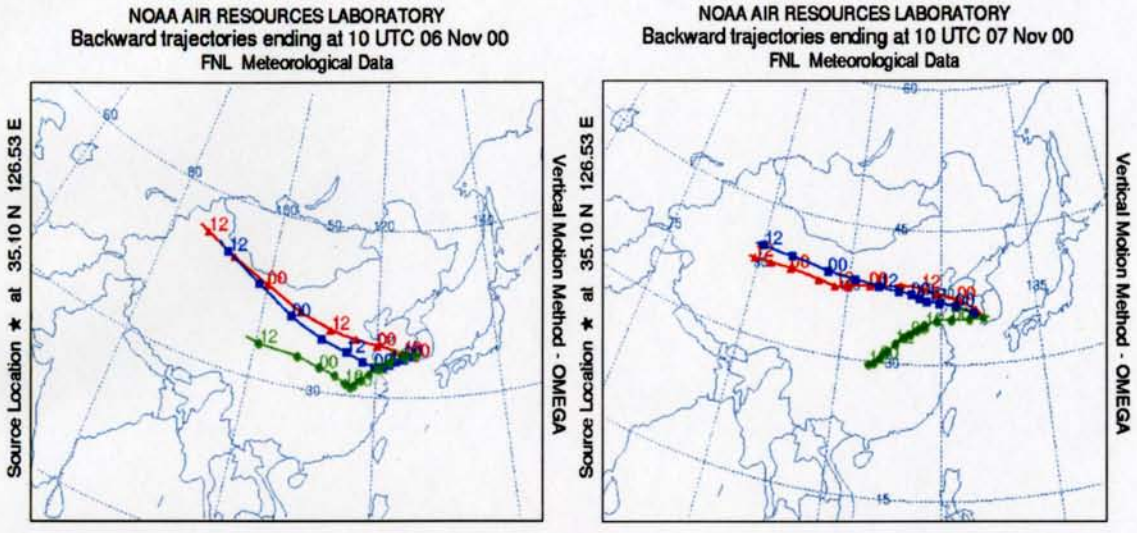

Figure 4.1.8 The distribution of back-trajectories pattern at 1500m, 2000m, 3000m in Kwangju, Korea during the 2nd sampling period (30.October ~ 6 November 2000).

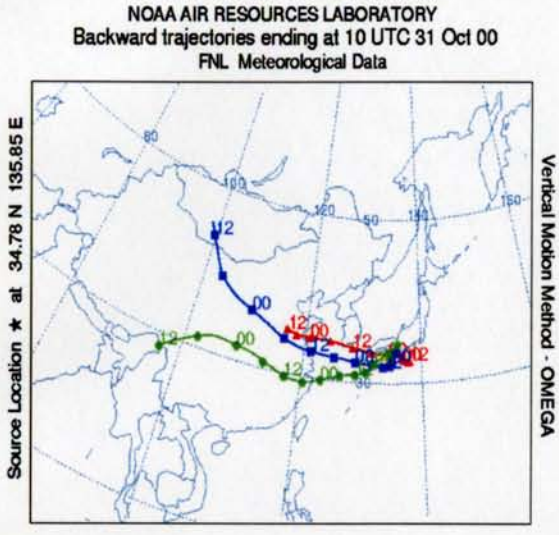
NOAA AIR RESOURCES LABORATORY
Backward trajectories ending at 10 UTC 31 Oct 00
FNL Meteorological Data
Source Location ★ at 34.78 N 135.85 E
Vertical Motion Method - OMEGA

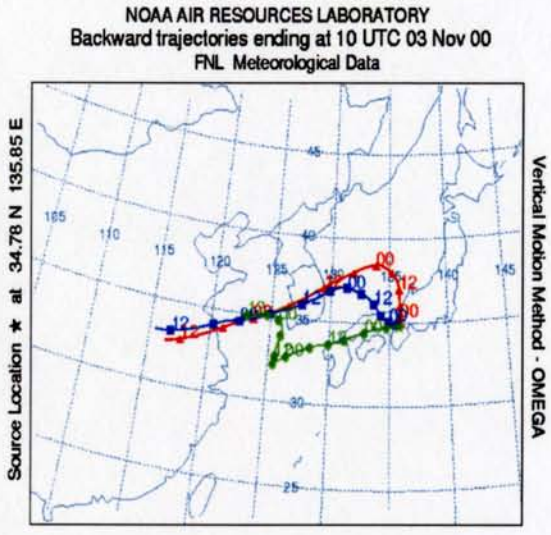
NOAA AIR RESOURCES LABORATORY
Backward trajectories ending at 10 UTC 03 Nov 00
FNL Meteorological Data
Source Location ★ at 34.78 N 135.85 E
Vertical Motion Method - OMEGA

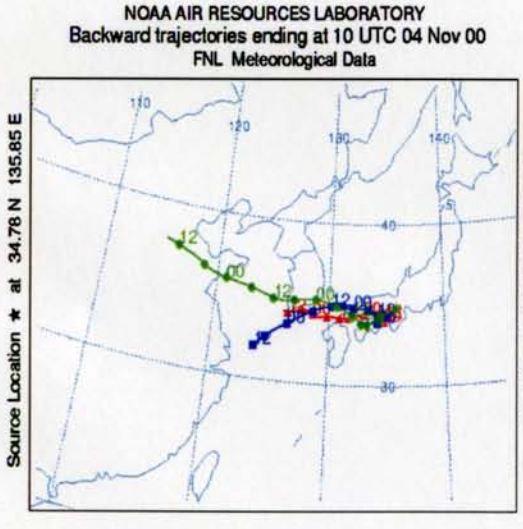
NOAA AIR RESOURCES LABORATORY
Backward trajectories ending at 10 UTC 04 Nov 00
FNL Meteorological Data
Source Location ★ at 34.78 N 135.85 E
Vertical Motion Method - OMEGA

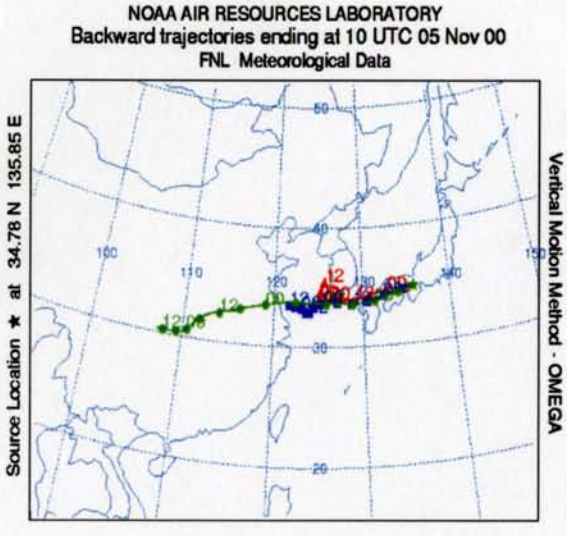
NOAA AIR RESOURCES LABORATORY
Backward trajectories ending at 10 UTC 05 Nov 00
FNL Meteorological Data
Source Location ★ at 34.78 N 135.85 E
Vertical Motion Method - OMEGA

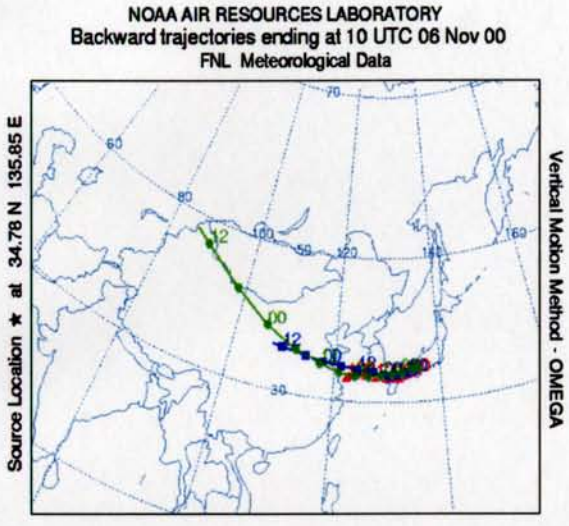

Figure 4.1.9 The distribution of back-trajectories pattern at 1500m, 2000m, 3000m in Kyoto, Japan during the 2nd sampling period (30.October ~ 6 November 2000).

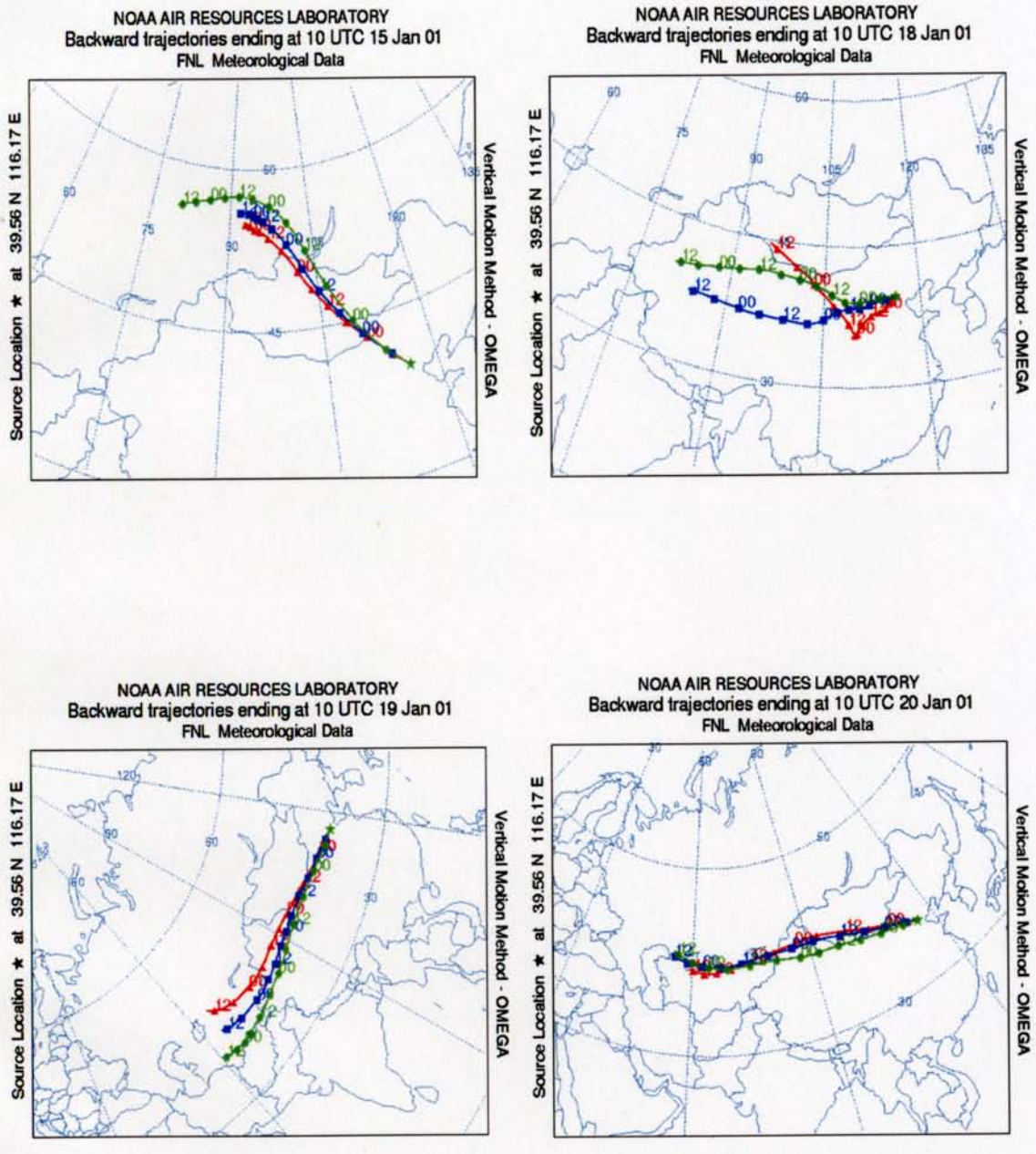

Figure 4.1.10 The distribution of back-trajectories pattern at 1500m, 2000m, 3000m in Beijing, China during the 3rd sampling period (14~21 January 2001).

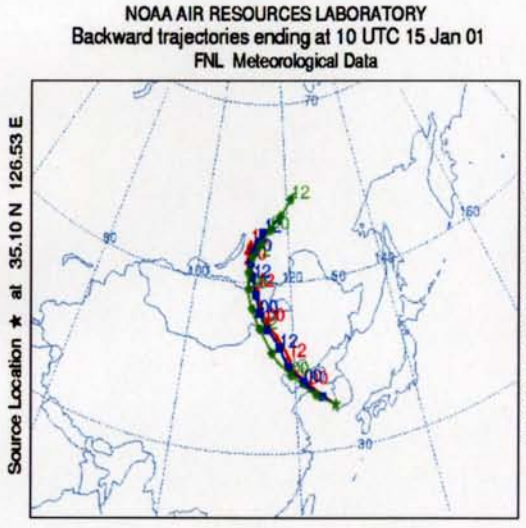
NOAA AIR RESOURCES LABORATORY
Backward trajectories ending at 10 UTC 15 Jan 01
FNL Meteorological Data
Source Location ★ at 35.10 N 126.53 E
Vertical Motion Method - DENSITY

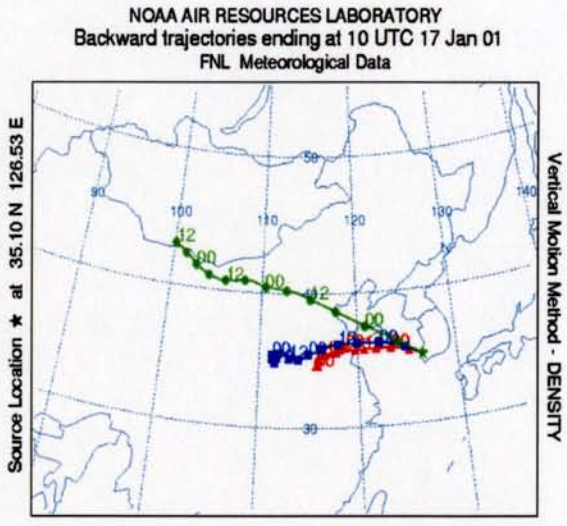
NOAA AIR RESOURCES LABORATORY
Backward trajectories ending at 10 UTC 17 Jan 01
FNL Meteorological Data
Source Location ★ at 35.10 N 126.53 E
Vertical Motion Method - DENSITY

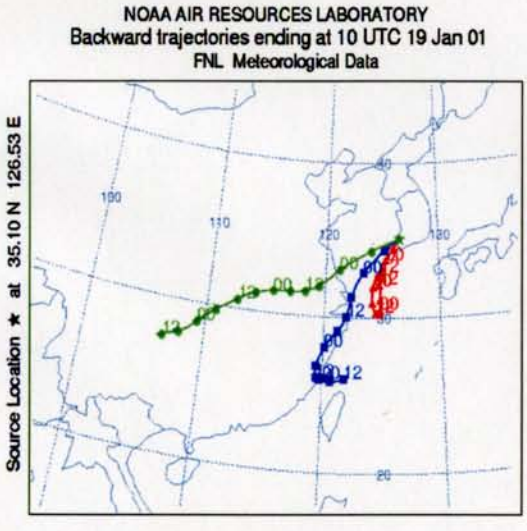
NOAA AIR RESOURCES LABORATORY
Backward trajectories ending at 10 UTC 19 Jan 01
FNL Meteorological Data
Source Location ★ at 35.10 N 126.53 E
Vertical Motion Method - DENSITY

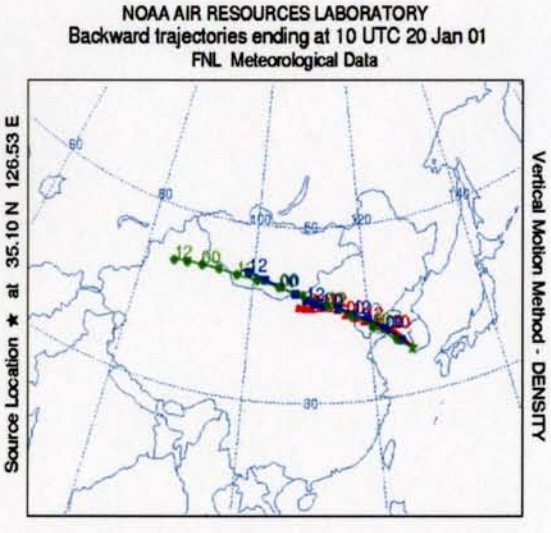
NOAA AIR RESOURCES LABORATORY
Backward trajectories ending at 10 UTC 20 Jan 01
FNL Meteorological Data
Source Location ★ at 35.10 N 126.53 E
Vertical Motion Method - DENSITY

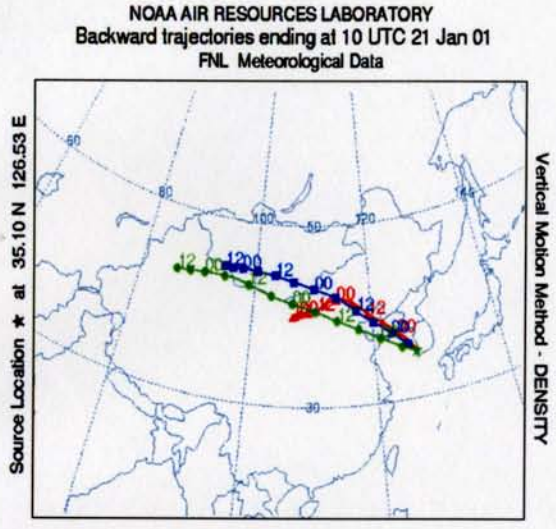

Figure 4.1.11 The distribution of back-trajectories pattern at 1500m, 2000m, 3000m in Kwangju, Korea during the 3rd sampling period (14~21 January 2001).

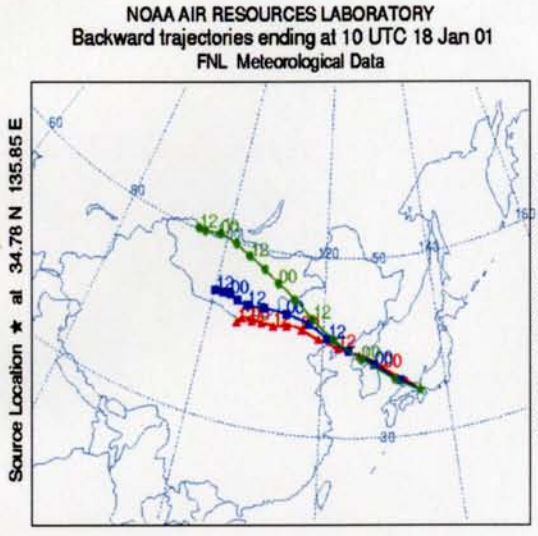
NOAA AIR RESOURCES LABORATORY
Backward trajectories ending at 10 UTC 18 Jan 01
FNL Meteorological Data
Source Location ★ at 34.78 N 135.85 E
Vertical Motion Method - DENSITY

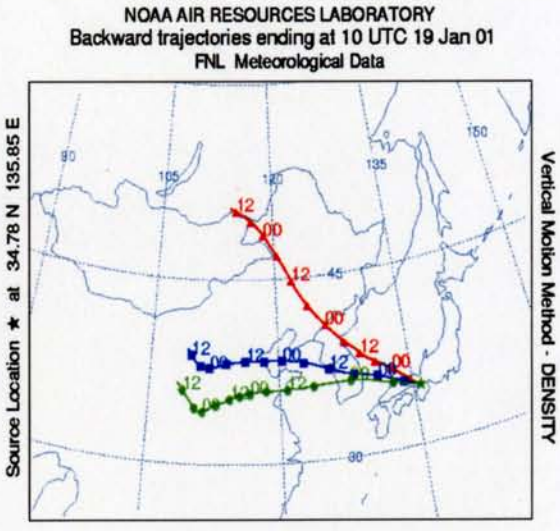
NOAA AIR RESOURCES LABORATORY
Backward trajectories ending at 10 UTC 19 Jan 01
FNL Meteorological Data
Source Location ★ at 34.78 N 135.85 E
Vertical Motion Method - DENSITY

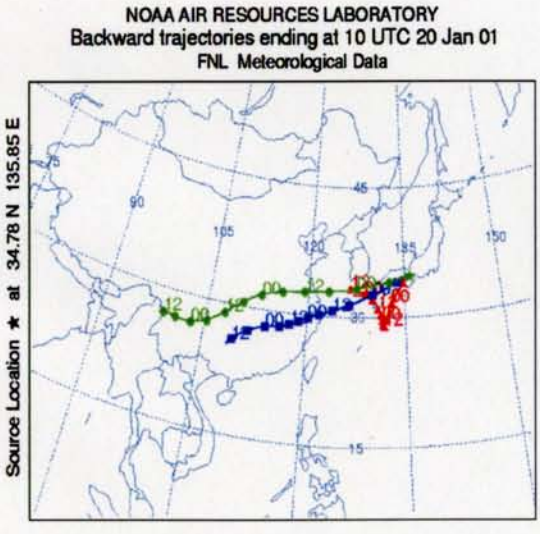
NOAA AIR RESOURCES LABORATORY
Backward trajectories ending at 10 UTC 20 Jan 01
FNL Meteorological Data
Source Location ★ at 34.78 N 135.85 E
Vertical Motion Method - DENSITY

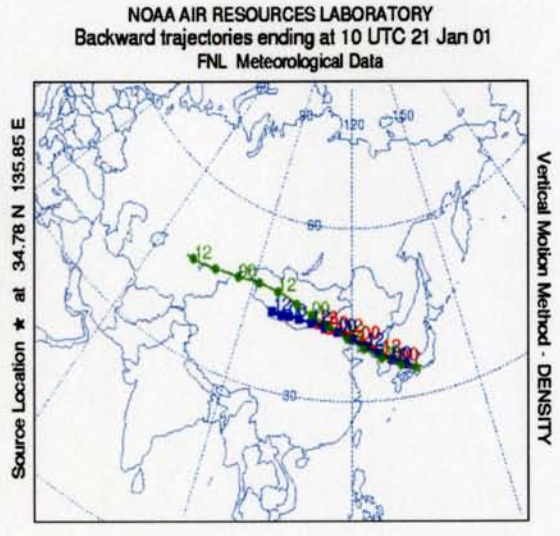
NOAA AIR RESOURCES LABORATORY
Backward trajectories ending at 10 UTC 21 Jan 01
FNL Meteorological Data
Source Location ★ at 34.78 N 135.85 E
Vertical Motion Method - DENSITY

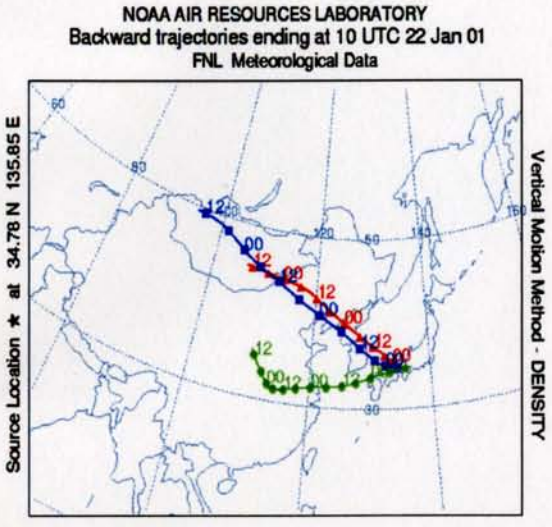

Figure 4.1.12 The distribution of back-trajectories pattern at 1500m, 2000m, 3000m in Kyoto, Japan during the 3rd sampling period (14~21 January 2001).

4.1.4 Organic carbon and elemental carbon

The carbonaceous fraction of ambient particulate matter consists of two major components – graphitic or black carbon (sometimes referred to as elemental carbon) and a variety of organic compounds (organic carbon). Elemental carbon (EC) can be produced only in the combustion process and is therefore solely primary. EC is especially effective in reducing visibility because of its light absorption properties. EC also plays an important role in the formation processes of secondary aerosols in the atmosphere (Chang et al., 1982). Organic carbon (OC), which is a matter of some concern because of possible mutagenic and carcinogenic effects, can be directly emitted from sources (primary OC) or produced from atmospheric reactions involving gaseous organic precursors (secondary OC) (Rogge et al., 1993). OC generally accounts for 60~90% of the carbon mass in airborne particulate matters (Frosjean, 1984) and represents a large variety of organic compounds in many classes, such as aliphatic, aromatic compounds, acids, etc (Daisey et al., 1986). Sources of carbonaceous aerosols are either primary or secondary. Primary sources are emitted as particles ; secondary sources are emitted as gases and undergo chemical or photochemical transformation processes in the atmosphere before forming compounds that have low volatility and may condense to form an aerosol. The natural sources of fine particle carbonaceous aerosols include : (a) primary emissions of particles from natural fires, (b) primary emissions of plant materials injected through abrasion and by direct means, and (c) emissions of organic vapors, which form condensable organics after partial oxidation in the atmosphere. Anthropogenic sources include : (a) primary emission from the burning of biomass, (b) primary emissions from the burning of fossil

fuels, from industrial processes and from fugitive source, and (c) emissions of volatile organics from fossil-fuel burning and industrial processes which form condensable organics after particle oxidation. Organic compounds and carbonaceous compounds such as carbonate are also found in the particle emissions associated with sources of dust and sea-salt aerosol, but since most of the mass of these aerosols in associated with larger-sized particles that are radiatively ineffective and small in number (Penner, 1995).

Table 4.1.5 shows the results of carbon analysis alongwith mass concentration of the aerosol samples collected at stations in January 2001. The concentrations of organic carbon and elemental carbon in Beijing were the highest, compared to those at other two sites. The average EC and OC concentrations in Beijing, Kwangju and Kyoto were 62.0 and 21.9, 7.8 and 3.8, and 3.6 and 1.9 $\mu g/m^3$, respectively. The OC and EC concentrations were plotted in Figure 4.1.13 along with data from other studies. Average OC concentration in PM 2.5 at Beijing was much larger than the values at other urban areas (Gray et al, 1986; Park et al, 2001).

Contributions of the primary and secondary components of aerosol OC have been difficult to quantify. Elemental carbon has often been used as a tracer of primary OC. The underlying hypothesis is that because EC and primary OC often have the same sources, there is a representative ratio of OC/EC for primary aerosol. If the measured ambient OC/EC ratio exceeds this expected value, then the additional OC can be considered to be secondary in origin. A weakness of that approach is that OC/EC emission rates vary by source and therefore the primary ratio will be influenced by meteorology, diurnal and seasonal fluctuations in emissions and local sources (Seinfeld and Pandis, 1998). The OC/EC ratio shown in Table 4.1.5 varied from 1.5 to 3.2. The

average OC/EC ratio at Kyoto was 1.9. This may be evidence that organic carbons are emitted mostly from primary organic local sources. Particulate organic to elemental carbon (OC/EC) ratios exceeding 2.0 have been used to indicate the presence of secondary organic aerosols (Gray et al., 1986) in summertime afternoon samples at downwind receptors. In other words, the additional OC that causes the OC/EC ration to exceed 2.0 can be considered to be secondary in origin (Park et al., 2001), which are the cases for Beijing samples in this study.

Table 4.1.5 Organic carbon (OC) and elemental carbon (EC) concentrations in January 2001.

($\mu g/m^3$)

	Date	Mass	OC	EC	TC	OC/EC
Beijing, China	15	188.9	51.0	15.8	66.8	3.2
	16	258.6	66.7	23.1	89.9	2.9
	17	366.9	82.9	33.4	116.3	2.5
	18	207.1	42.4	16.4	58.8	2.6
	19	278.0	67.0	20.9	87.9	3.2
	AVE.	259.9	62.0	21.9	83.9	2.9
Kwangju, Korea	14	8.3	2.7	0.9	3.6	2.9
	15	14.6	3.2	1.2	4.5	2.6
	16	21.8	4.7	2.0	6.7	2.4
	17	36.7	12.1	5.8	18.0	2.1
	18	62.7	15.9	8.3	24.2	1.9
	19	53.0	10.6	5.7	16.3	1.9
	20	37.9	5.5	2.3	7.8	2.4
	AVE.	33.6	7.8	3.8	11.6	2.3
Kyoto, Japan	15	14.2	4.0	1.6	5.7	2.5
	16	8.0	2.6	1.4	4.0	2.0
	17	18.0	4.2	2.4	6.5	1.8
	18	22.0	3.8	1.8	5.6	2.2
	19	24.1	3.9	2.5	6.4	1.5
	20	23.3	3.4	1.8	5.1	1.9
	21	12.5	3.2	2.0	5.1	1.6
	AVE.	17.5	3.6	1.9	5.5	1.9

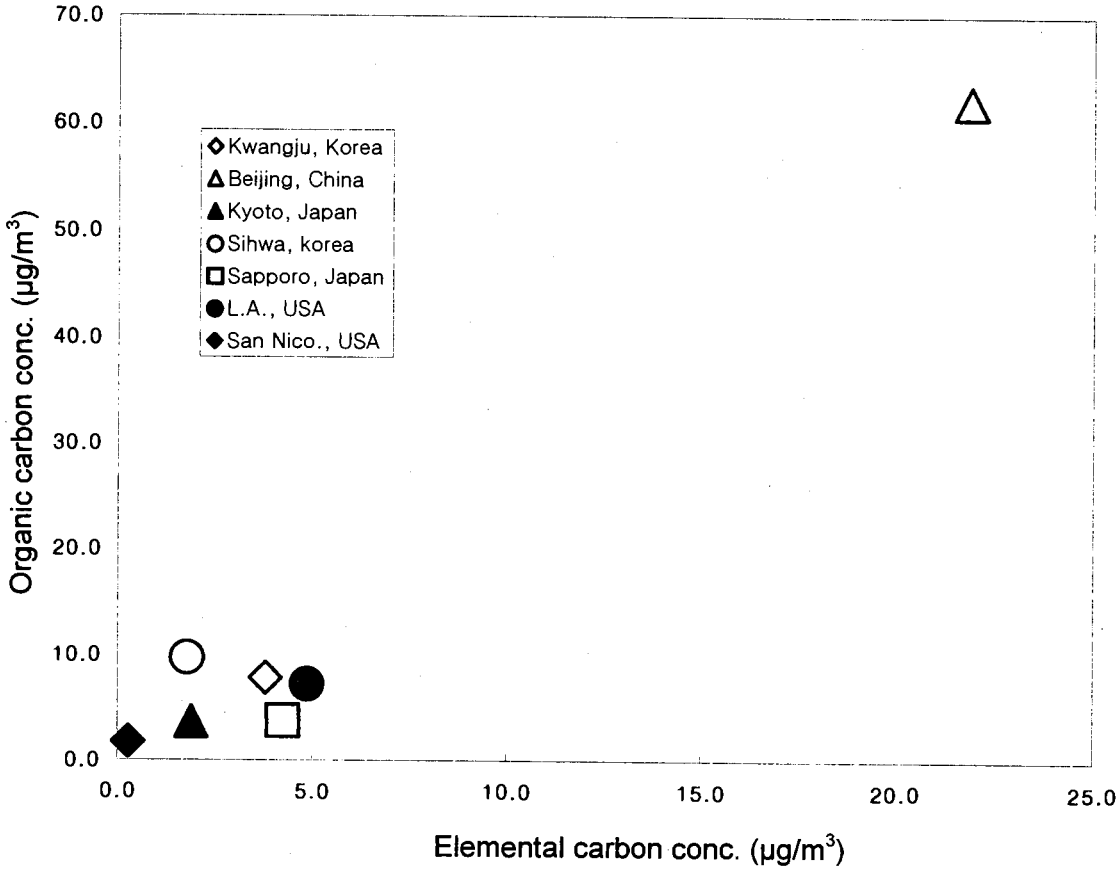

Figure 4.1.13 Comparison of EC with OC : Kwangju, Beijing and Kyoto; in this study; LA and San Nico., USA: Gray et al.(1986); Sihwa, Korea: Park et al.(2001); Sapporo, Japan: Ohta et al.(1998).

4.1.5 Aerosol size distribution

An important characteristic of the generation of atmospheric aerosol particles is its temporal as well as spatial variability. Information on the size distribution of particulate matter is vital to developing an understanding of its generation, transport, deposition, and climatic effects. The number/size distribution is particularly important in climate considerations (Duce, 1995)

In this section, the result of size distribution measurement of atmospheric aerosols over the Kwangju, Korea and Kyoto, Japan are discussed. An eight-stage cascade impactor (MOUDI, Micro-Orifice Uniform Deposition Impactor, and 12-stage low pressure Andersen sampler were operated for collecting size-segregated aerosol samples at Kwangju and Kyoto, respectively. Two problems are likely to occur with impactor type samplers ; one is the bounce problem which would result in collection of particles on subsequent stages due to their impaction on the filter surface during penetration of the jet and the other is that the filters do not suppress particle bounce off completely. Particle bounce effect may be of less significance in the summer than the winter. However, it can be reasonably constant over the sampling period and that the size distribution may well serve intercomparison purpose. As shown in Figure 4.1.14 two size distributions measured at kwangju and Kyoto are very similar, the majority of the mass is in the fine size range (d <2.5 μm). It was reported that winter mass median diameters are slightly smaller than summer values probably due to the effect of the annual variations of the relative humidity. However, the majority of the mass is in the coarse size range during the strong yellow sand events (d >2.5 μm) (Bae, 1999).

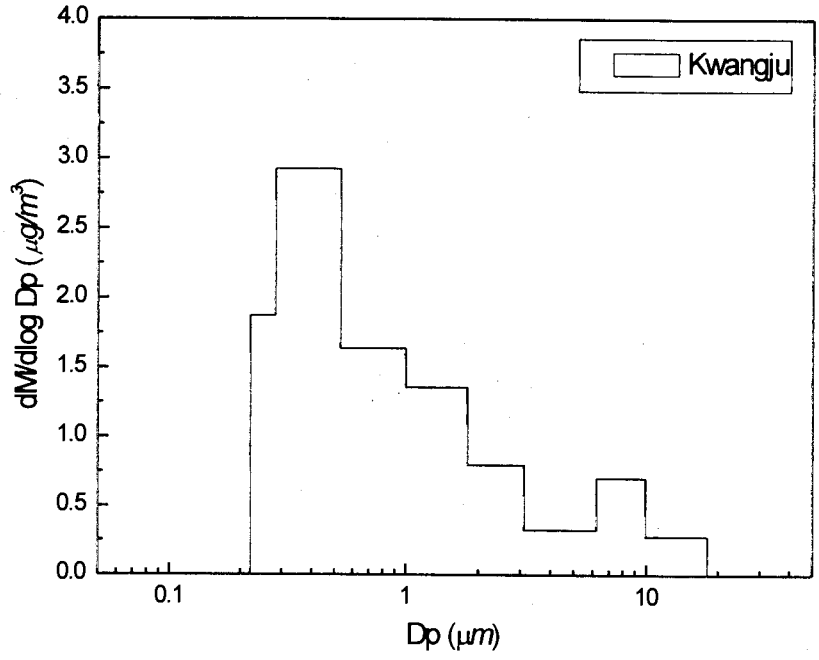

(a) Kwangju, Korea

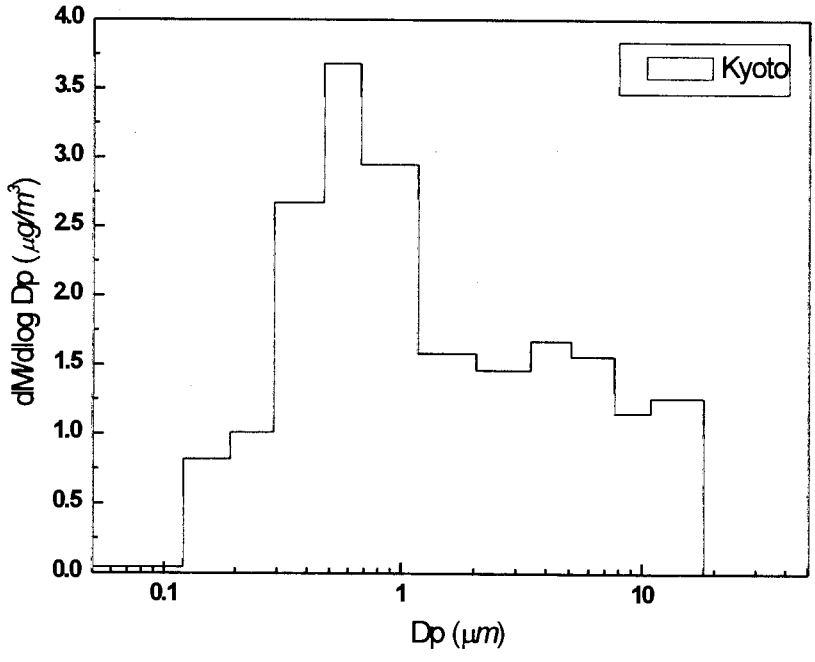

(b) Kyoto, Japan

Figure 4.1.14 Aerosol size distributions measured at Kwangju, Korea (a) and Kyoto, Japan (b) in January 2001.

4.2 Optical properties of aerosols

4.2.1 Aerosol extinction coefficient and visibility

For the chemical mass balance of fine particulate trace element concentrations, three chemical analyses consisting of IC, ICP/MS & /AES, TMO (Thermal Manganese Oxidation) were performed on samples collected at Kwangju, Korea. At most urban atmosphere, fine aerosol species are classified into five major types: sulfates, nitrates, organic mass, elemental and light-absorbing carbon, and soil. Mass concentrations were calculated from the masses of the measured elements and ions according to IMPROVE programs summarized below [IMPROVE, 1993].

Ammonium Sulfate [Sulfates]

In the urban atmosphere where ammonia can be sufficient most sulfur is in the form of ammonium sulfate ($(NH_4)_2SO_4$). All elemental sulfur was assumed as being in the form of ammonium sulfate, and ammonium sulfate concentrations were calculated by multiplying elemental sulfur concentrations by molar correlation factor 4.125. For simplicity, ammonium sulfate is referred to as [sulfate].

Ammonium Nitrate [Nitrates]

Collected nitrate ion is associated with fully neutralized ammonium nitrate aerosol (NH_4NO_3). The mass of ammonium nitrate was calculated by using a molar correlation factor of 1.29 and was referred to as [nitrate].

Organic Mass by Carbon [OMC]

Organic mass concentration by carbon (organics, OMC) was calculated by the Equation 3-4.

$$[OMC] = 1.4[OC] \quad (3\text{-}4)$$

The correlation factor 1.4 assumes that organic mass contains a constant fraction of carbon by weight (Watson et al., 1988).

Elemental Carbon [EC]

Elemental carbon can absorb light, was calculated by the TMO method, which converted the carbon evolved at each step into CO_2, using an oxidizer, MnO_2 then quantified.

Soil [SOIL]

Soil mass concentration was calculated by summing the elements predominantly associated with soil, plus oxygen for the normal oxides (Al_2O_3, SiO_2, CaO, K_2O, FeO, Fe_2O_3, TiO_2), plus a correlation for other compounds such as MgO, Na O, water, and carbonate. A final equation for fine soil after dividing by 0.86 is:

$$[SOIL] = 2.20[Al] + 2.49[Si] + 1.63[Ca] + 2.42[Fe] + 1.94[Ti] \quad (3\text{-}5)$$

Components of these factors were confirmed in comparisons of local resuspended

soils (Cahill, et al., 1981; Pitchford et al., 1981).

Reconstructed Fine Mass [RCFM]

The sum of the above five composites should provide a reasonable estimate of the ambient fine mass concentration measured in the atmosphere (RCFM). The equation for RCFM concentration is therefore:

$$[RCFM] = [Sulfate] + [Nitrate] + [OMC] + [EC] + [SOIL] \quad (3\text{-}6)$$

Coarse Mass [CM]

Coarse mass (CM) was calculated gravimetrically by subtracting fine mass (PM2.5) concentration from total aerosol mass (PM10) concentration:

$$[CM] = [PM10] - [PM2.5] \quad (3\text{-}7)$$

Atmospheric extinction can be calculated from the mass of various particulate species if the scattering cross section of each species is known, and if the hourly ambient relative humidity during sampling is also known. The equations used to determine reconstructed aerosol extinction follow IMPROVE Program protocol and are outlined below [IMPROVE, 1993].

$$b_{ext} = 3\ f(RH)\ [Sulfate] + 3\ f(RH)[Nitrate] + 4\ [OMC] + 1[Soil] + 0.6[CM] + b_{abs} + b_{Ray} \quad (3\text{-}8)$$

Where the first 5 components represent the light scattering by aerosol species, b_{abs}

represents the coefficient of light absorption for fine particles, and b_{Ray} represents the light scattered by molecules of gas in the natural atmosphere, which varies with atmospheric pressure, and is a site-specific measurement based on altitude. Generally b_{Ray} can be negligible at the urban area because the value is extremely smaller than those of others. The constants 3, 4, 1, 0.6 are the dry scattering efficiency of sulfates, nitrates, organics, soil and coarse mass in unit of m^2/g (Sisler, 1996).

The worst visibility is linked to the maximum in sulfate and nitrate concentration that are called acidic aerosol. In most cases, the sulfate and nitrate components of fine aerosol are the largest contributors to light extinction. This is because sulfate, being hygroscopic, generally has higher light extinction efficiency than other species due to associated liquid water. b_{scat} from sulfate and nitrate shows a functional dependence on relative humidity. These species grow rapidly under conditions of increasing humidity to attain diameters that most efficiently scatter light. During the night time the contribution of acidic aerosol is, therefore, higher than during the day time due to higher relative humidity in the ambient atmosphere. Generally, reconstructed light extinction is higher in night time and lower in daytime; however, there are many exceptions to this general rule due to frequent sudden shower in summer and other meteorological conditions.

In Figure 4.2.1 "Best 20%" is the average of the lowest 20 percent of extinction coefficient values. Likewise the terms, "Worst 20%" and "Middle20%" refer to an average of the upper 20 % range, 80 to 100 %, and middle 20 % range, 40 to 60 %, respectively.

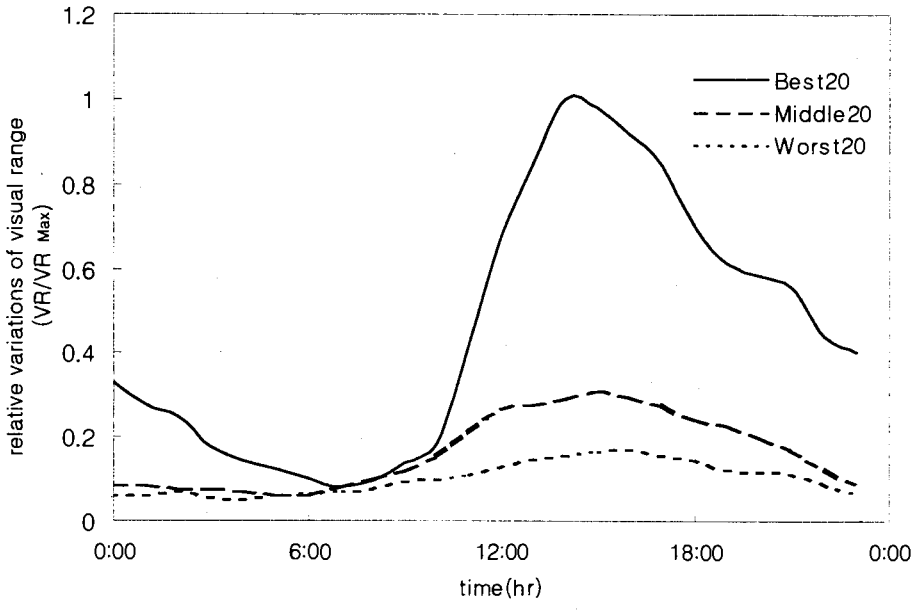

Figure 4.2.1 Diurnal variation of relative visual range by the three haze levels.

a)"Best 20 %": VR =50 ~ 62km, b_{ext} = 0.063 ~ 0.078 Mm^{-1}, dv = 18.4 ~ 20.6

b)"Middle 20%": VR =24 ~ 36km, b_{ext} = 0.109 ~ 0.163 Mm^{-1}, dv = 23.9 ~ 27.9

c)"Worst 20%": VR < 12km, b_{ext} > 0.326 Mm^{-1}, dv > 34.8

While an average visual range increased from 5.9 to 61.7km, average light extinction budgets of sulfate and nitrate decreased from 43.8 to 12.7 % and from 18.0 to 8.7 %, respectively. Under the same condition average light extinction budget of elemental carbon and organics increased from 12.8 to 22.2 % and from 21.8 to 47.0 % respectively during the intensive monitoring period.

4.2.2 Contributions of Light absorption by EC

During summer intensive monitoring period, 12 July to 22 July 2000 in Kwangju, mean light absorption budget by elemental carbon was 7.3 % and daytime mean light

absorption budget was 7.5 %. Visual range varied from 1.7km to 62.4 km during the sampling period. Average visual range during day time and night time was 15.3km and 13.8km respectively.

Figure 4.2.2 shows that the variation of visual range have great correlation with the ratio of b_{abs} to b_{ext}. On a clean day absorption coefficient, b_{abs} by elemental carbon becomes a major contributor to degradation of visibility in the urban atmosphere. Effect of elemental carbon on light absorption increased 4.6 times while the visual range increased from 11.8 to 58.6km. During the same time period elemental carbon concentration did not exhibit any apparent correlation with the variation of visual range. These results illustrate that sulfate, nitrate and hygroscopic organic compounds are important major contributors to degradation of visibility due to increased light scattering under worse visibility conditions as compared to small absorption by elemental carbon.

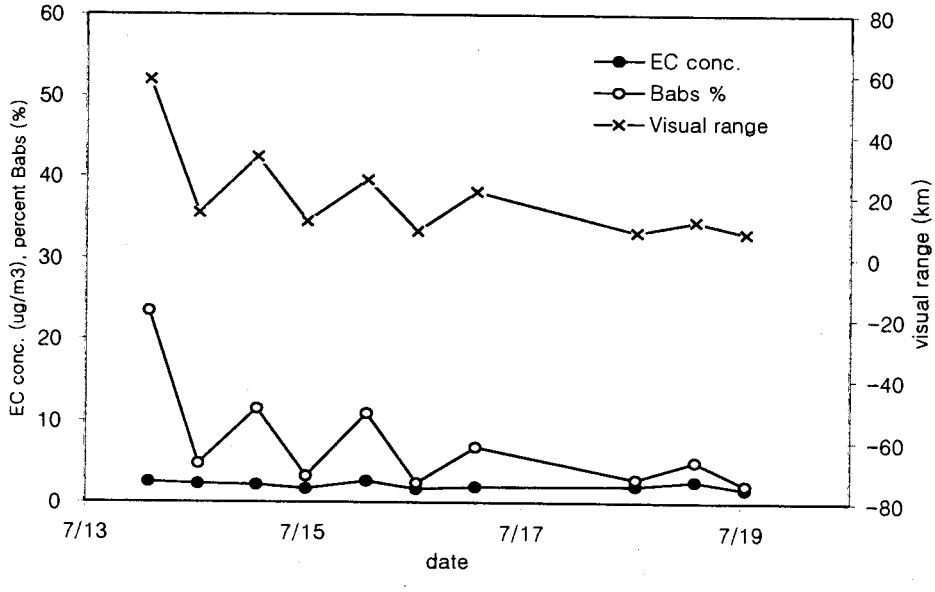

Figure 4.2.2 Effect of Carbonaceous particles on visibility degradation.

4.3 Radiative properties of atmospheric aerosols.

4.3.1 Radiative properties of aerosols

Figure 4.3.1 shows the diurnal variation of monthly mean global and diffuse radiations at Kwangju (January ~ December 2000). Results show a distinct seasonal difference in the mean diurnal variation of global and diffuse radiations in the individual at each site. The daily global and diffuse radiations increase steadily in the early hours (08hr from December ~ February and 06hr from March ~ November) and reaches maxima around 12hr-13hr in the afternoon, and gradually decreases to their minima at about 17hr-20hr depending on the month of the year. The maximum average seasonal global radiation at Kwangju was measured to be 750w/m^2, 716.4 w/m^2, 554.9 w/m^2, and 494.2 w/m^2 in spring, summer, fall and winter respectively. The maximum diffuse radiation was measured to be 346.7 w/m^2, 590.8 w/m^2, 460.7 w/m^2 and 374.7 w/m^2 in spring, summer, fall and winter respectively at Kwangju. The high value of diffuse radiation in spring can be attributed to the increase in the atmospheric aerosol loading in the Korea peninsular and also to the intensive biomass burning.

Figure4.3.2 shows the daily distribution of global and diffuse radiation at Kwangju. The figure depicts an increase in the diffuse radiation at the surface during the spring season (March-May) that corroborates the earlier findings of maximum diffuse radiation during spring months. Figure 4.3.3 shows the daily diffuse ratio at Kwagnju and it similarly indicates a maximum of 0.95 in May (spring).

Figures 4.3.4 and 4.3.5 show the diurnal variations of monthly mean global and diffuse radiations at Beijing and Ulaanbaartar respectively for November – December

2000. The values of the maximum monthly mean hourly global and diffuse radiations at Beijing are 294.1w/m^2 and 242.4 w/m^2 respectively while Ulaambaartar recorded 211.8 w/m^2 and 167.9 w/m^2 respectively. Figures 4.3.1, 4.3.2, 4.3.3 4.3.4 and 4.3.5 show seasonal variation of the global and diffuse radiations each months at Kwangju, Beijing and Ulaanbaartar.

Figure 4.3.6 shows the annual variation of global and diffuse radiations at Kwangju from January-December 2000. It shows a gradual increase in global and diffuse radiations from the early hours (600-700hr), reaches their maxima at 1200hr local time and decreases to near zero in the evening at around 1900hr.

Figure 4.3.7 gives an insight to the seasonal distribution of the hourly global radiation for clear days free from dust and clouds. It shows global radiation is maximized in summer and minimized in winter.

Figure 4.3.8 shows the seasonal variation of diffuse radiation at Kwangju for clear days from January-December 2000. It is evident from this figure that the maximum diffuse radiation in spring is as a resulted from depletion of solar radiation by atmospheric aerosol. Figure 4.3.9 shows the total atmospheric optical depth (TOD) at Kwangju during the periods of measurement. The maximum and minimum daily total atmospheric optical depths are 0.84 and 0.09 in March and October, respectively. The maximum TOD in March also corroborates the earlier findings of increase in atmospheric aerosol at Kwangju in spring. The minimum in October can be attributed to the dust free clean air condition under low relative humidity. However, it is interesting to note an increase in the TOD at Kwangju in October due to the prevalent biomass burning in this area in preparation for the next farming season. The annual mean TOD at Kwangju was 0.28 while the seasonal was 0.25, 0.32, 0.29 and 0.29 for winter,

spring, summer and fall, respectively. This indicated that except for the winter season all other seasons have their total atmospheric optical depth higher than the average in the year under consideration.

Figures 4.3.10 and 4.3.11 show the total atmospheric optical depth at Beijing and Ulanbaartaar, respectively but for limited time period from October to December 2000. .During this time period the maximum and minimum daily TOD values were recorded at Beijing to be 0.65 and 0.17, respectively. This is in strong agreement with the findings of Yunfeng et al., (2000) on the characteristics of atmospheric aerosol optical depth variation over China in the past 30years. However, the maximum and minimum TOD recorded at Ulaanbaartar were 0.59 and 0.04, respectively for the period October ~ December 2000. Figure 4.3.12 shows the relationship between the monthly total atmospheric optical depth, the computed clearness index, (CI) and the diffuse ratio at Kwangju from January ~ December 2000. The clearness index, (CI) indicates the percentage depletion of incoming radiation by the atmosphere while the diffuse ratio is a quantity that mirrors the effectiveness of the sky in the scattering the incoming radiation (Ideriah & Suleman, 1989, Kuye & Japtap, 1992). From figure 4.3.12 it is evident that as the clearness index of the atmosphere decreases from February till May. The TOD values and the diffuse ratio reache their maxima in March. Figure 4.3.13 shows the correlation between the clearness index and TOD at Kwangju. A negative correlation of 0.67 was observed which represents an inverse relationship between the TOD and the clearness index at Kwangju. The total atmospheric optical depth (TOD) and Aerosol optical depth (AOD) at Kwangju are shown in Figure 4.3.14. The maximum occurrence of TOD and AOD varies from season to season and result shows that the atmospheric aerosol loading in the atmosphere at Kwangju was higher in year

2000 than the previous years. The maximum AOD at Kwangju in 1998, 1999 and 2000 are 0.66, 0.59 and 0.72, respectively while the maximum TOD were 0.71, 0.63 and 0.76 respectively. Figure 4.3.13 shows the daily variation of Total Atmospheric Optical Depth at Kwangju (January – December 2000), Beijing (October-December 2000) and Ulanbaataar (October-December 2000).

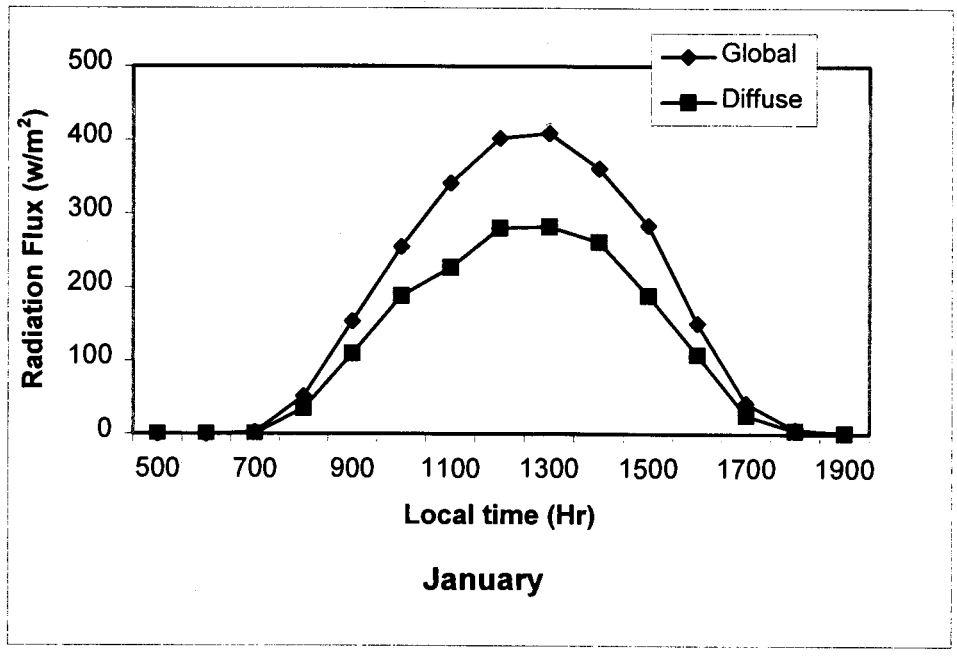

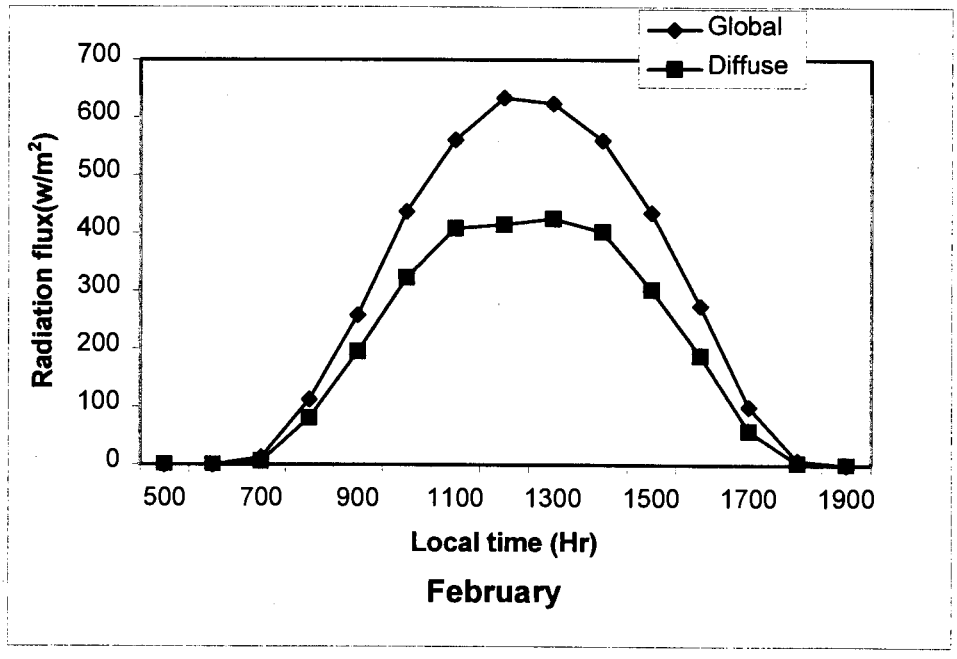

Figure 4.3.1 Diurnal Variations of Monthly mean global and diffuse radiations at Kwangju (January ~ December 2000).

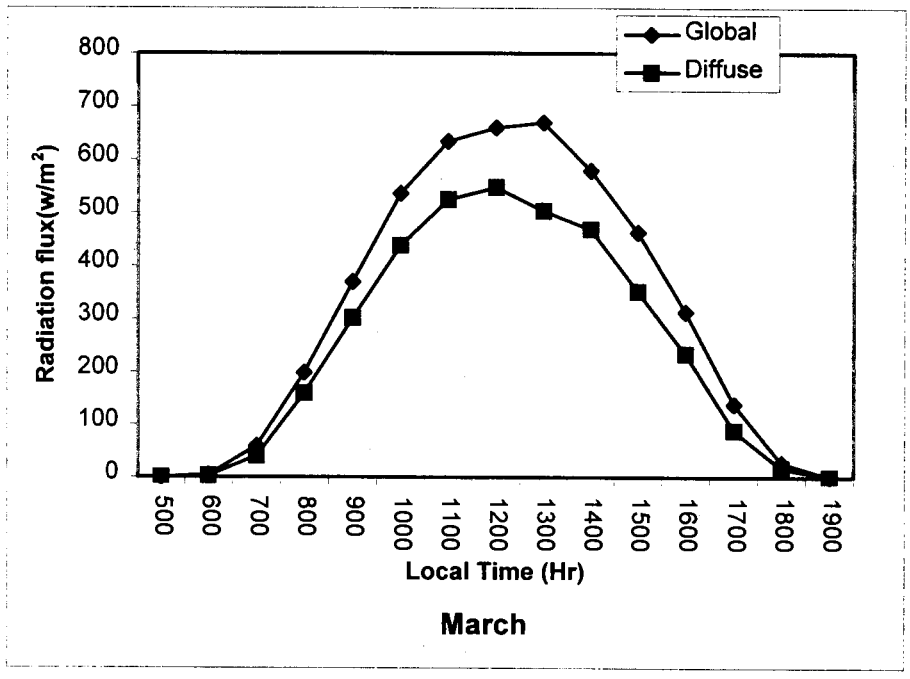

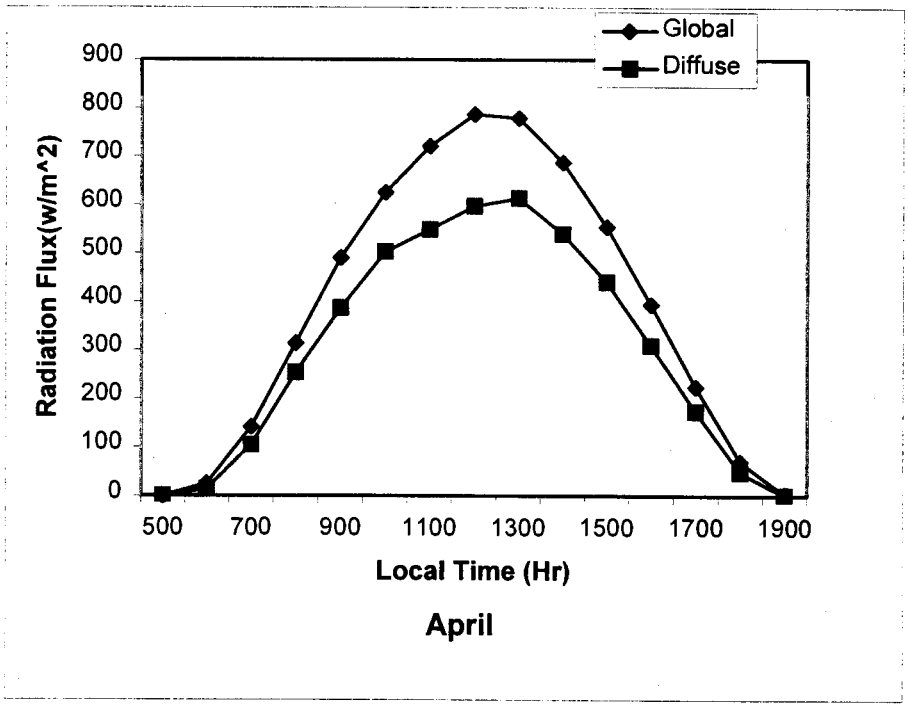

Figure4.3.1 (Continued)

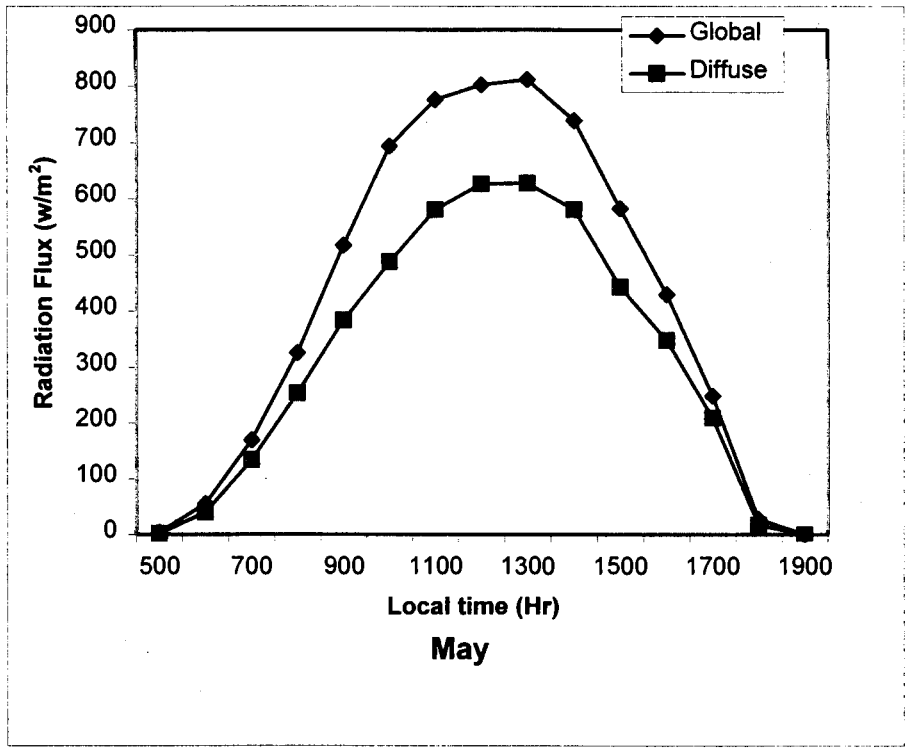

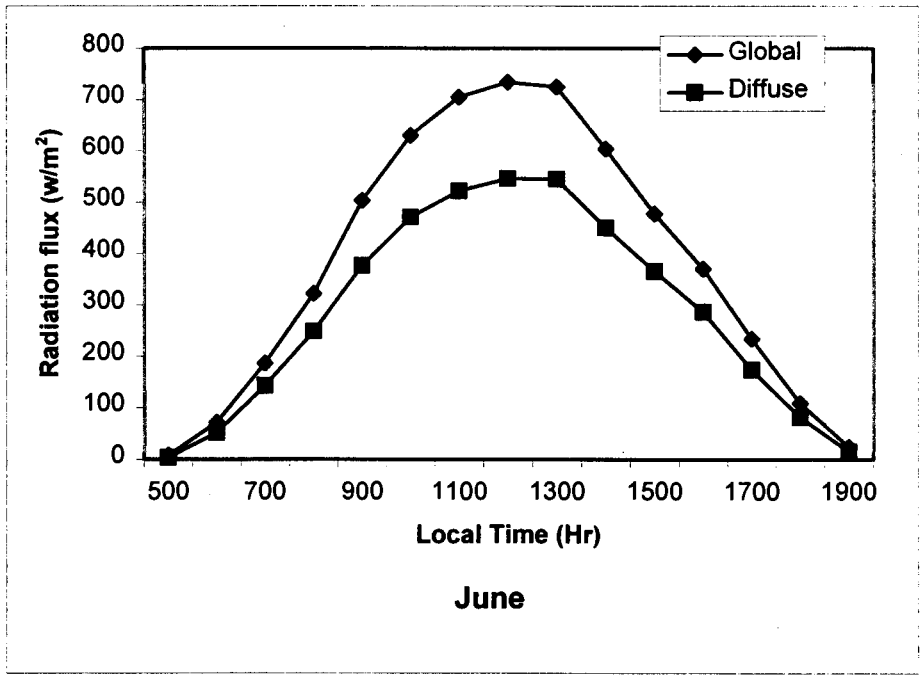

Figure 4.3.1 (Continued)

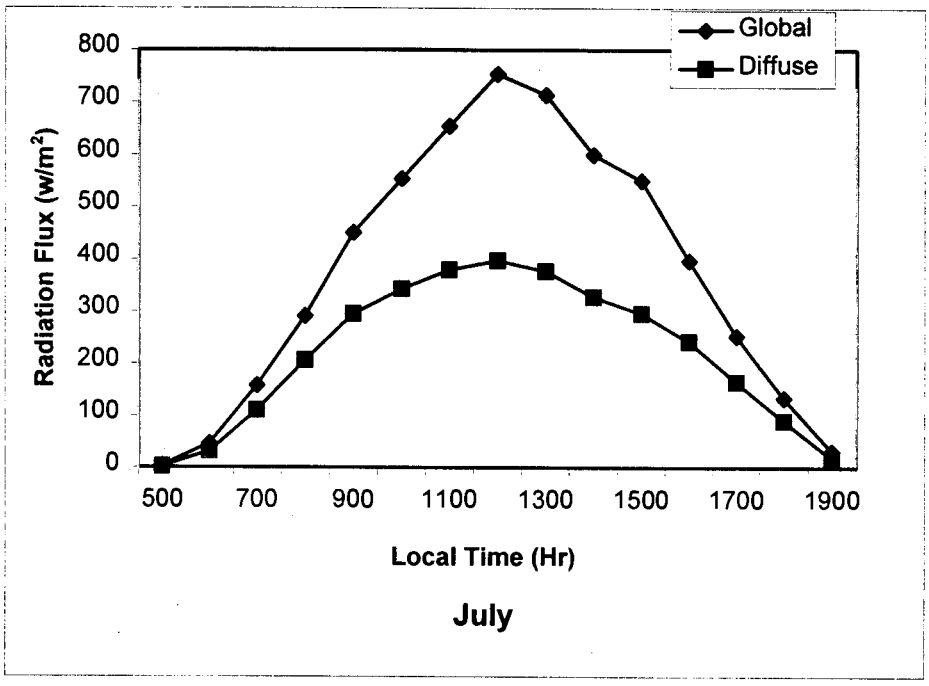

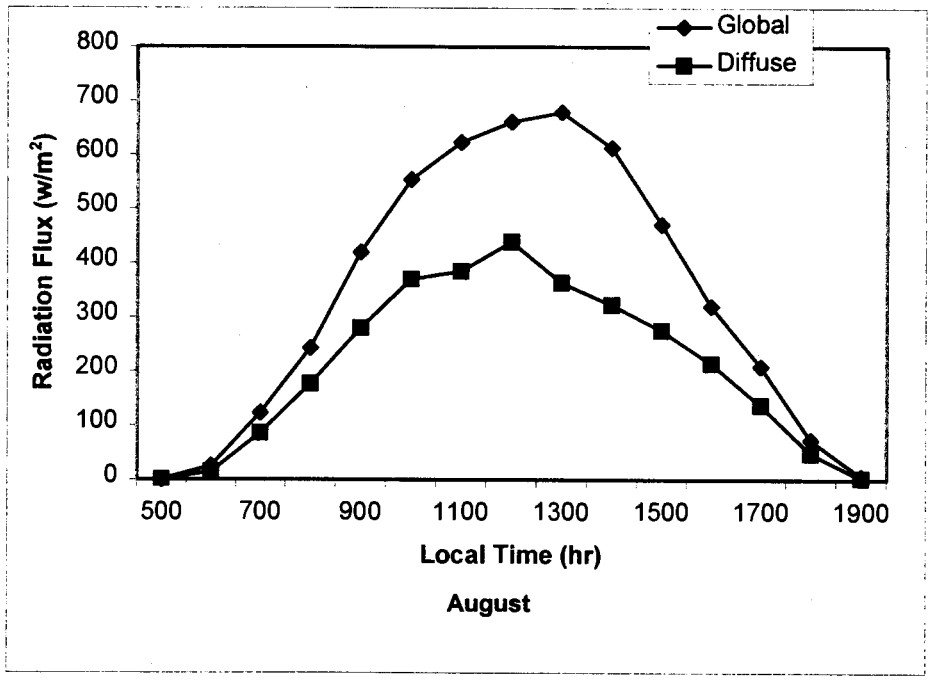

Figure 4.3.1 (Continued)

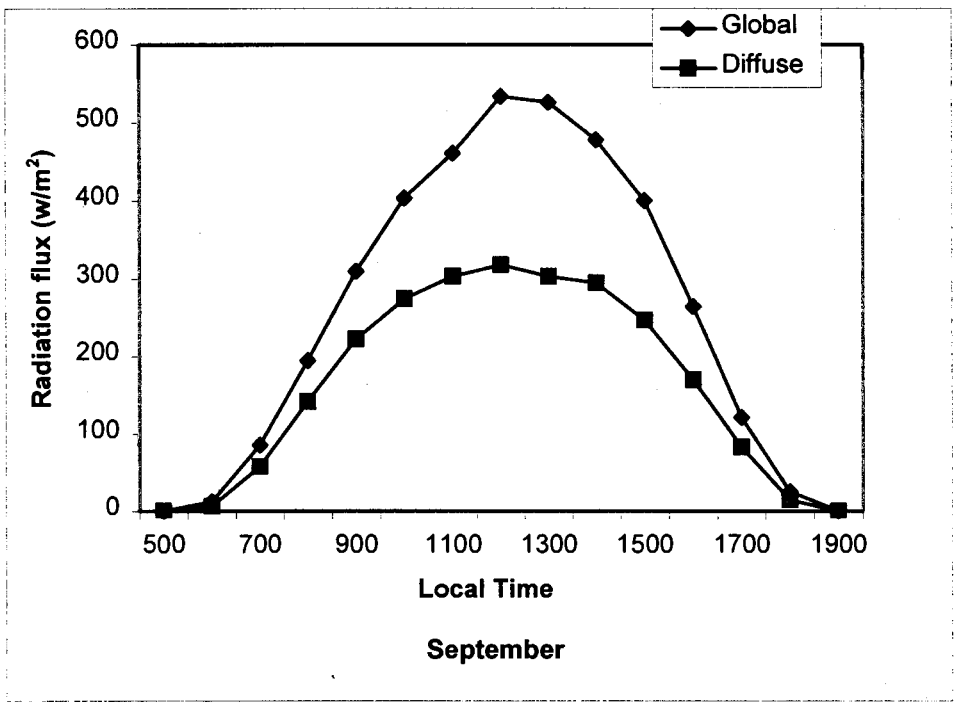

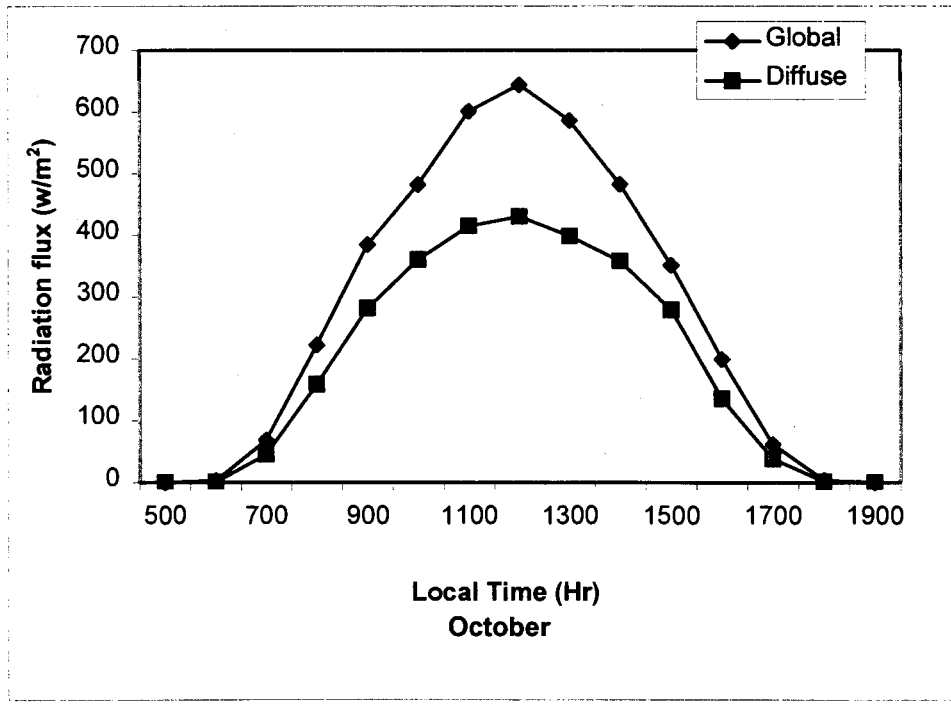

Figure 4.3.1 (Continued)

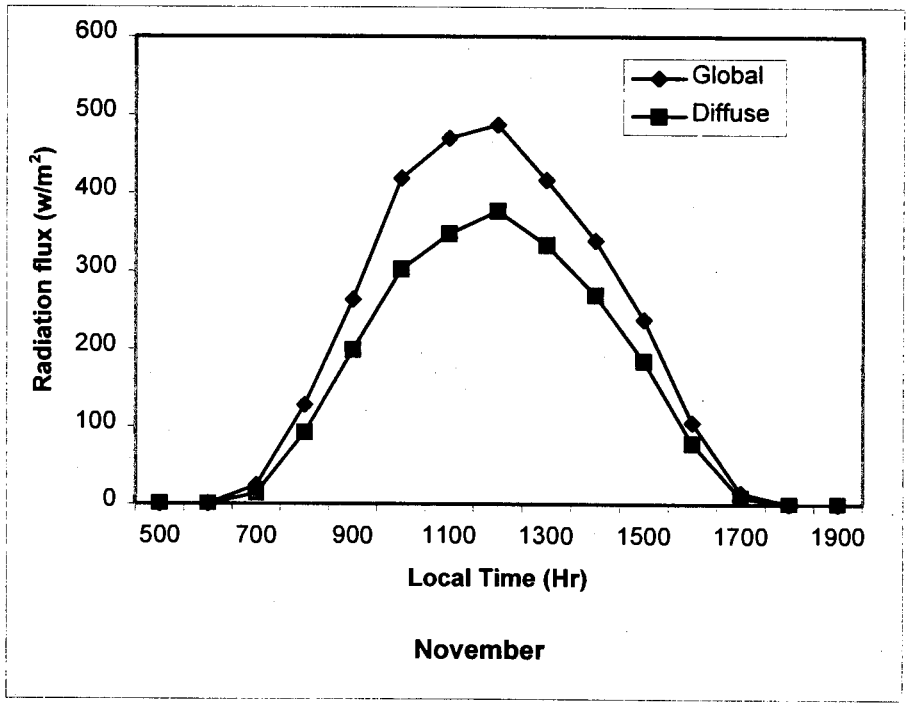

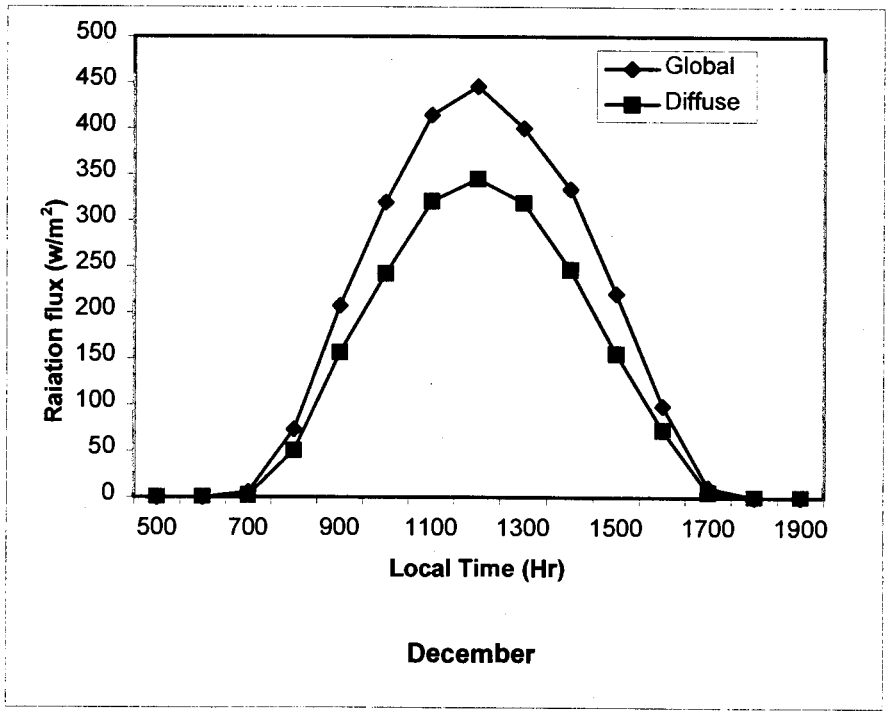

Figure 4.3.1 (Continued)

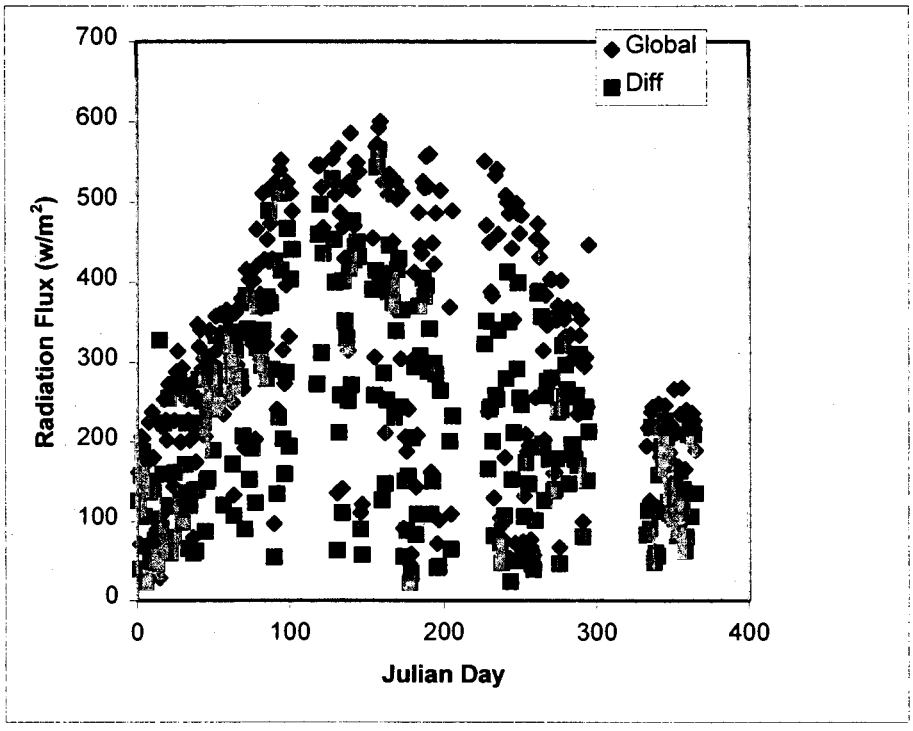

Figure 4.3.2 Daily variations of global and diffuse radiations at Kwangju (January ~ December 2000).

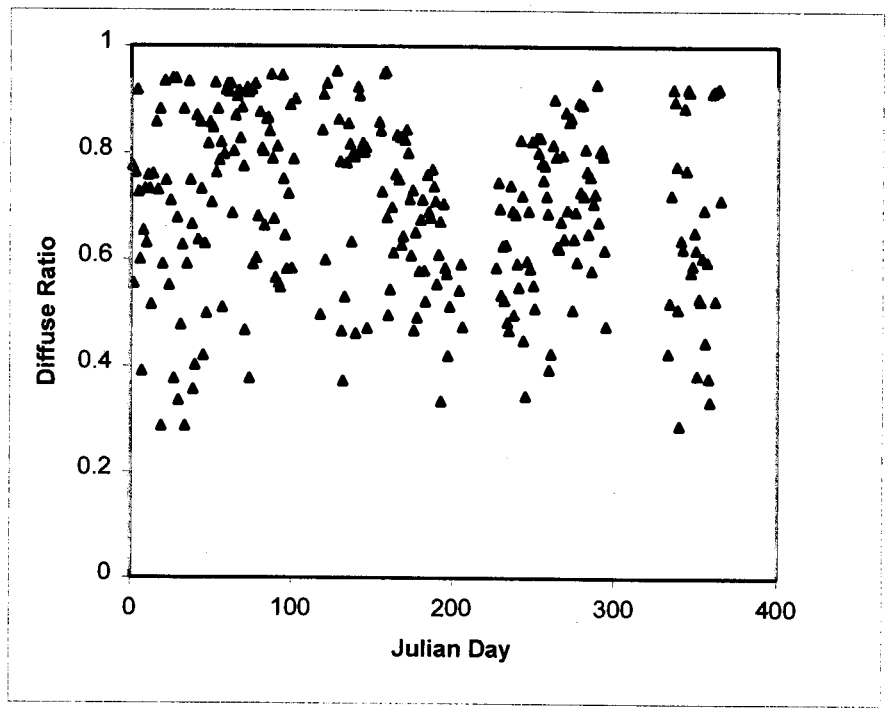

Figure 4.3.3 Daily Variations of Diffuse ratio at Kwangju (January ~ December 2000).

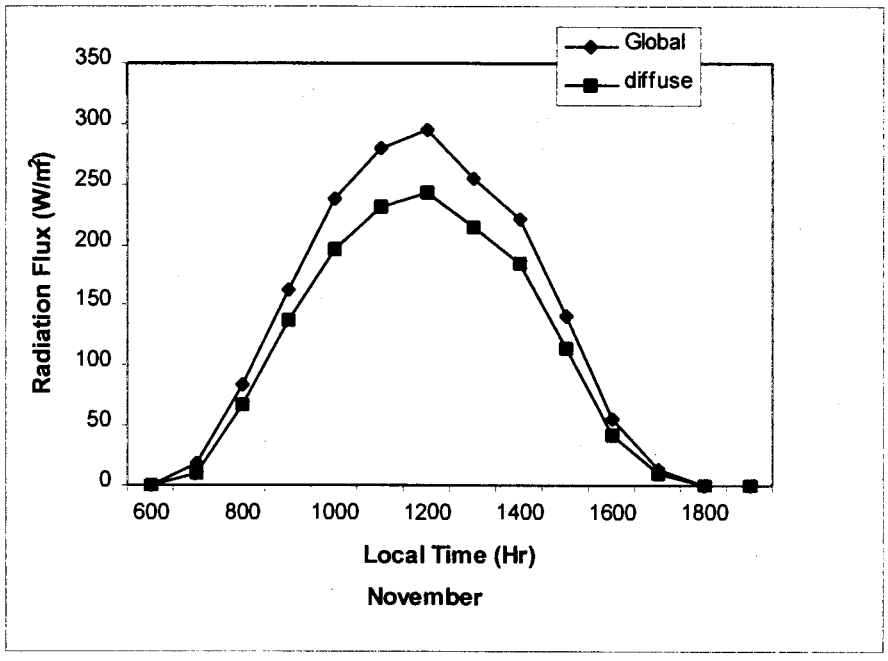

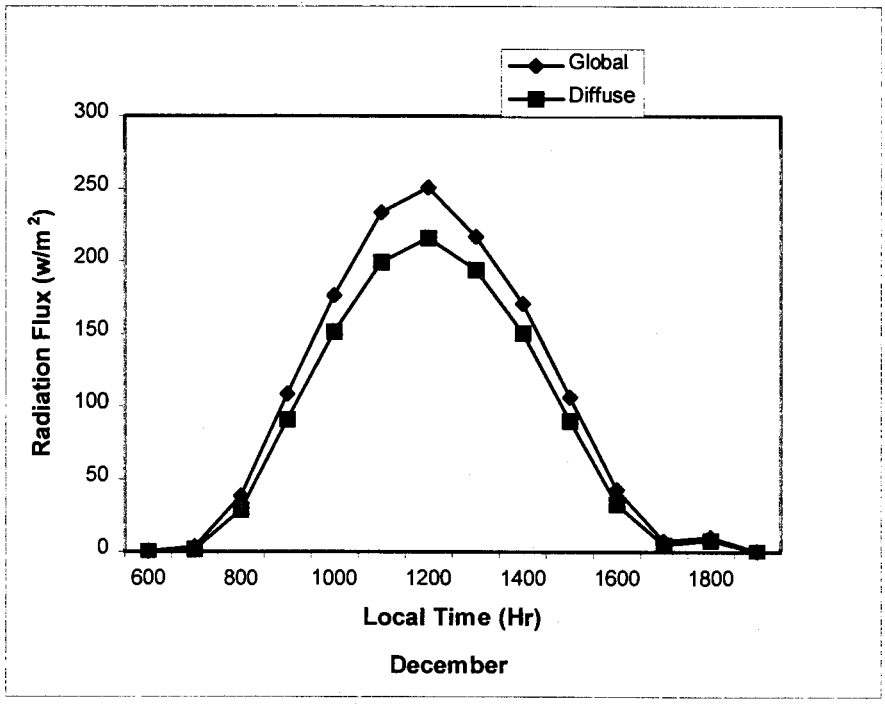

Figure 4.3.4 Diurnal Variation of Monthly mean Global and Diffuse Radiations at Beijing (November ~ December 2000).

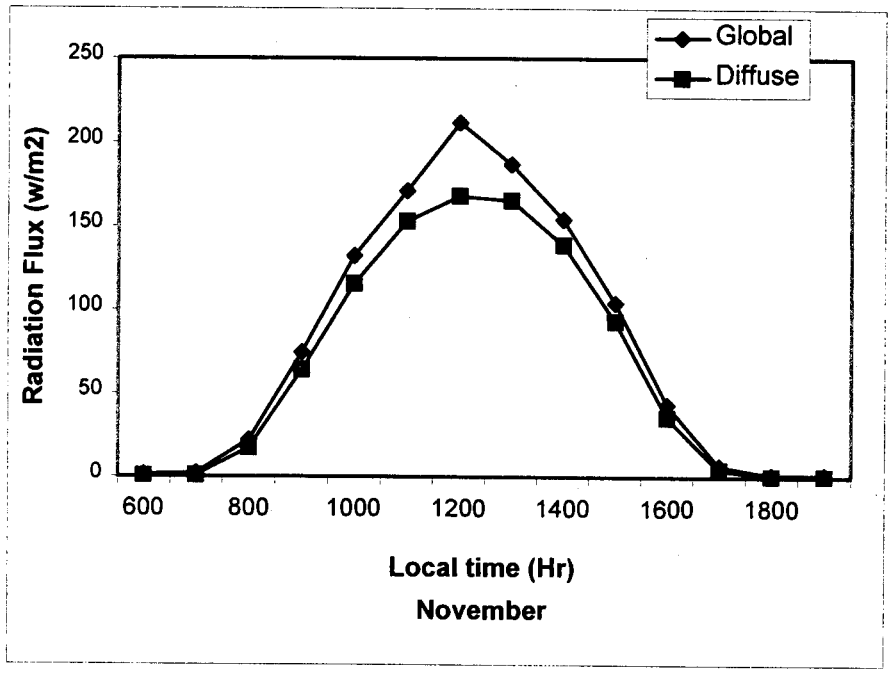

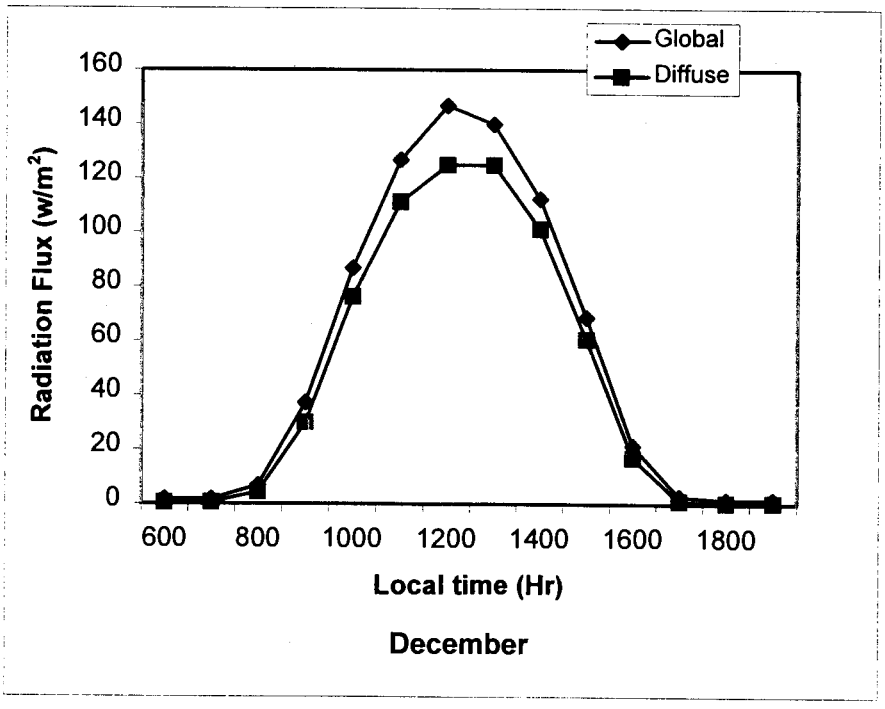

Figure 4.3.5. Diurnal Variations of Monthly mean Global and Diffuse Radiations at Ulaanbaartar (November ~ December 2000).

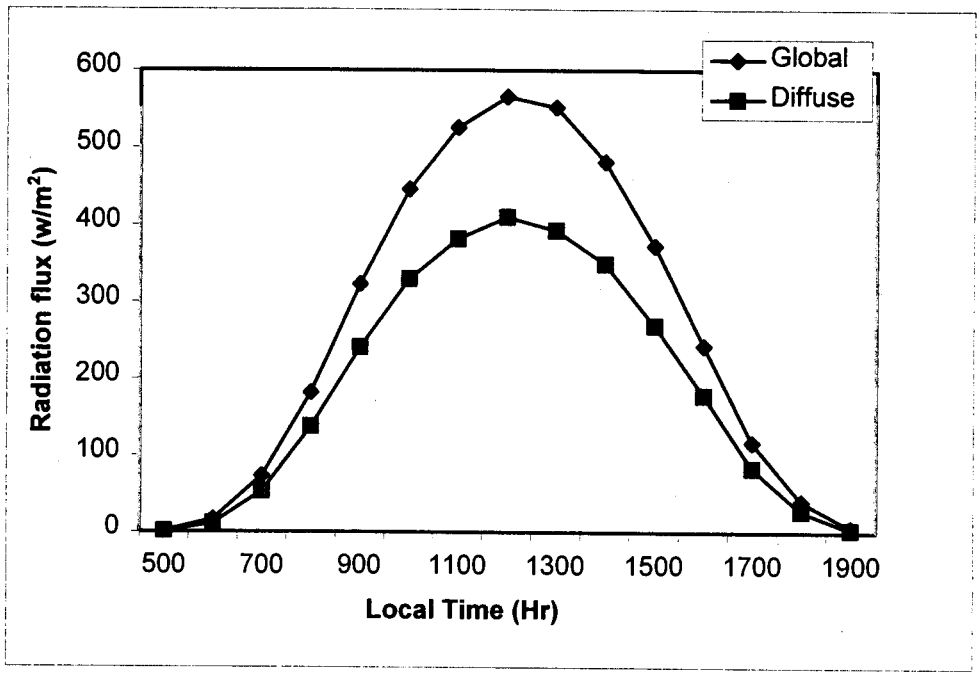

Figure 4.3.6 Annual Variation global and diffuse radiation at Kwangju (January ~ December 2000).

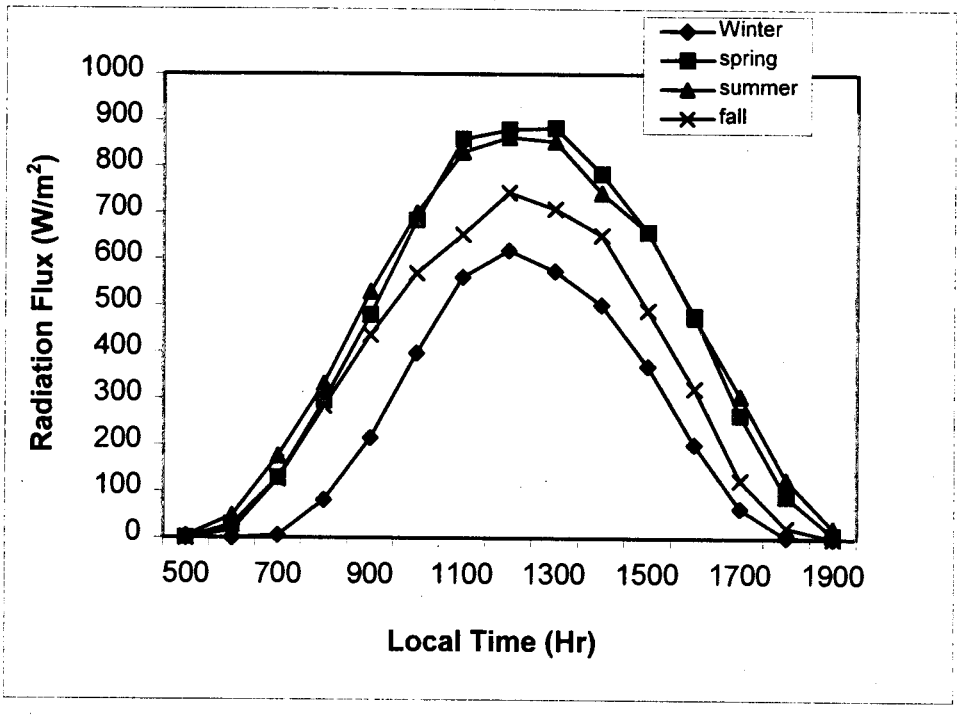

Figure 4.3.7 Seasonal Diurnal Variation of Global Radiation for Clear Days at Kwangju (January ~ December 2000).

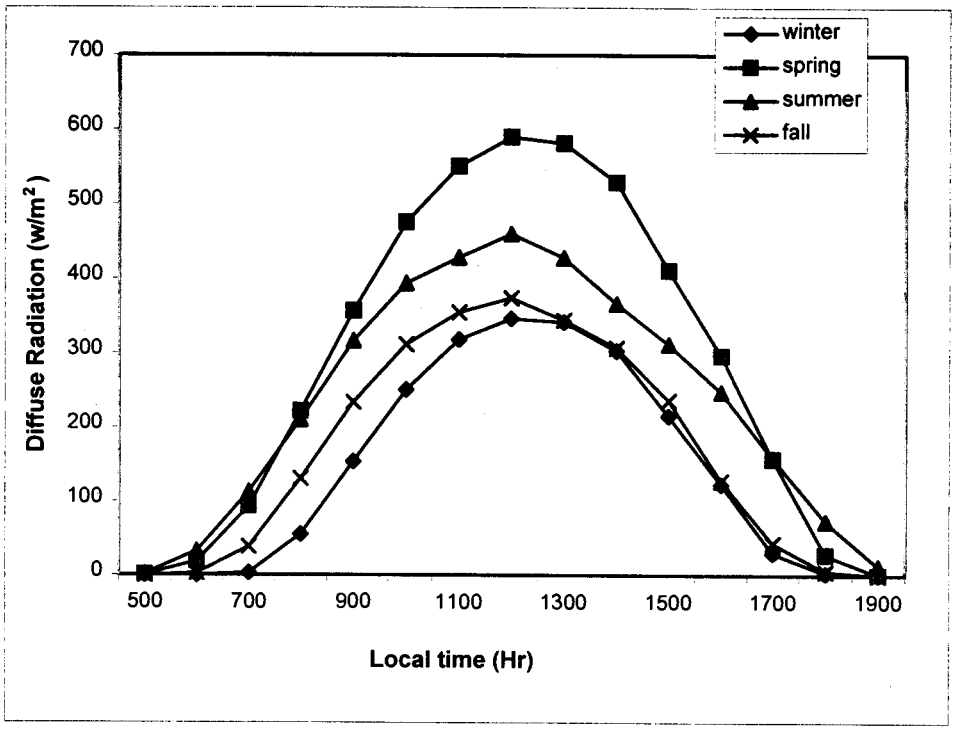

Figure 4.3.8 Seasonal variation of diffuse radiation for clear days at Kwangju (January ~ December 2000)

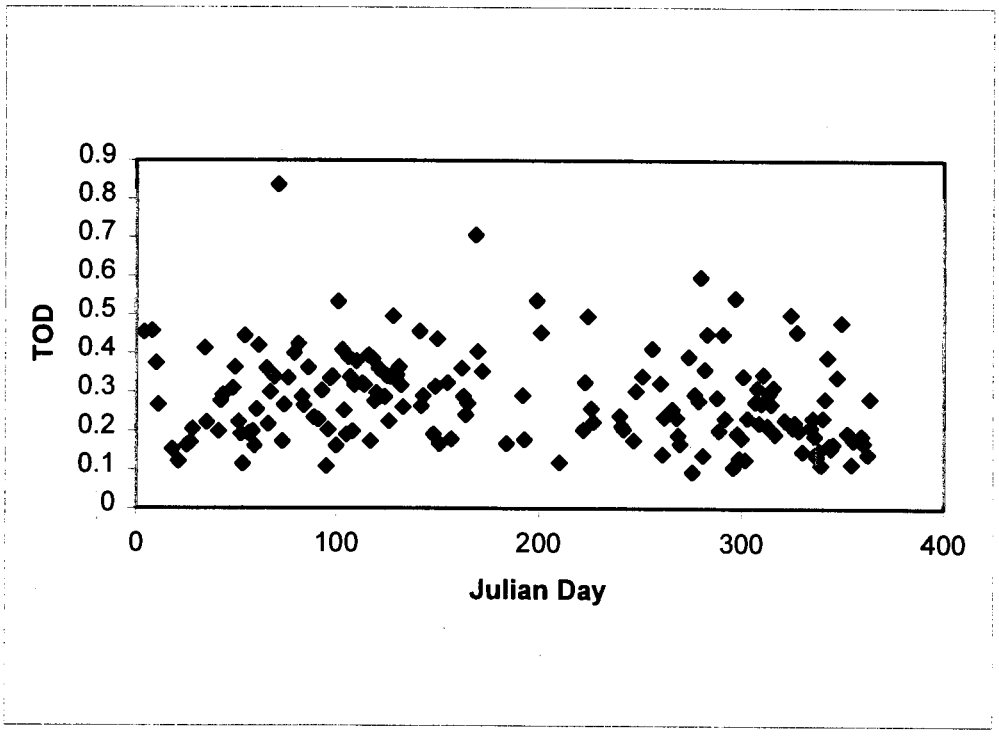

Figure 4.3.9 Total Atmospheric Optical Depth at Kwangju (January ~ December 2000).

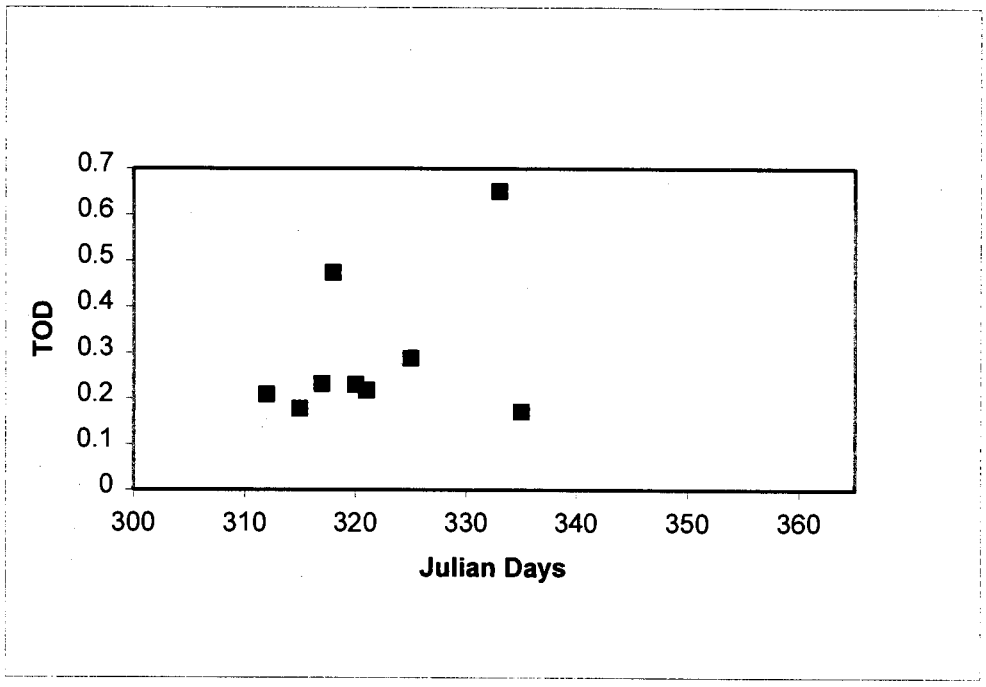

Figure 4.3.10 Daily Variation of Total Atmospheric Optical Depth at Beijing (November ~ December 2000).

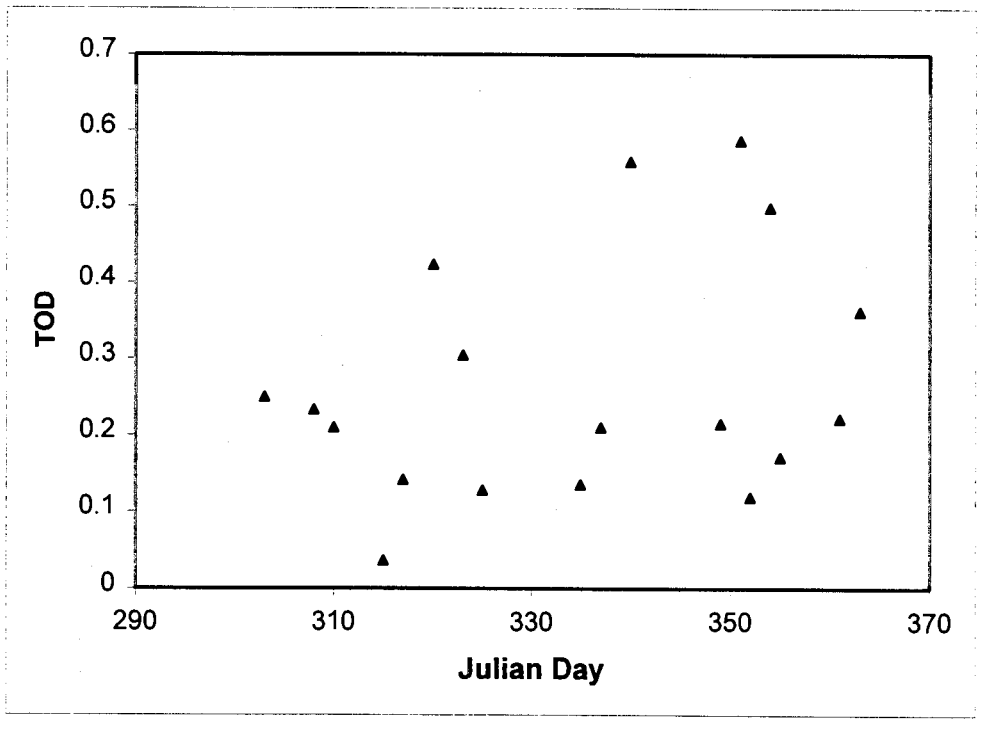

Figure 4.3.11 Daily variation of Total Atmospheric Optical Depth at Ulaanbaartar (October ~ December 2000).

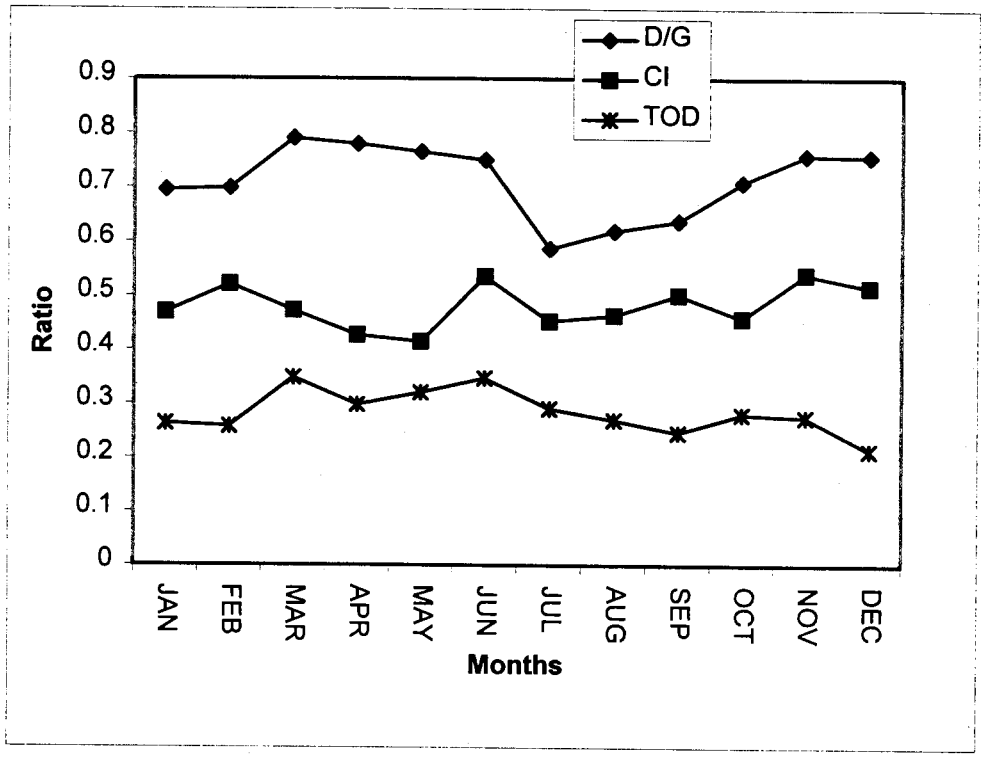

Figure 4.3.12 Monthly Total Atmospheric Optical Depth (TOD), Clearness Index (CI), Diffuse Ratio (D/G) at Kwangju (January ~ December 2000)

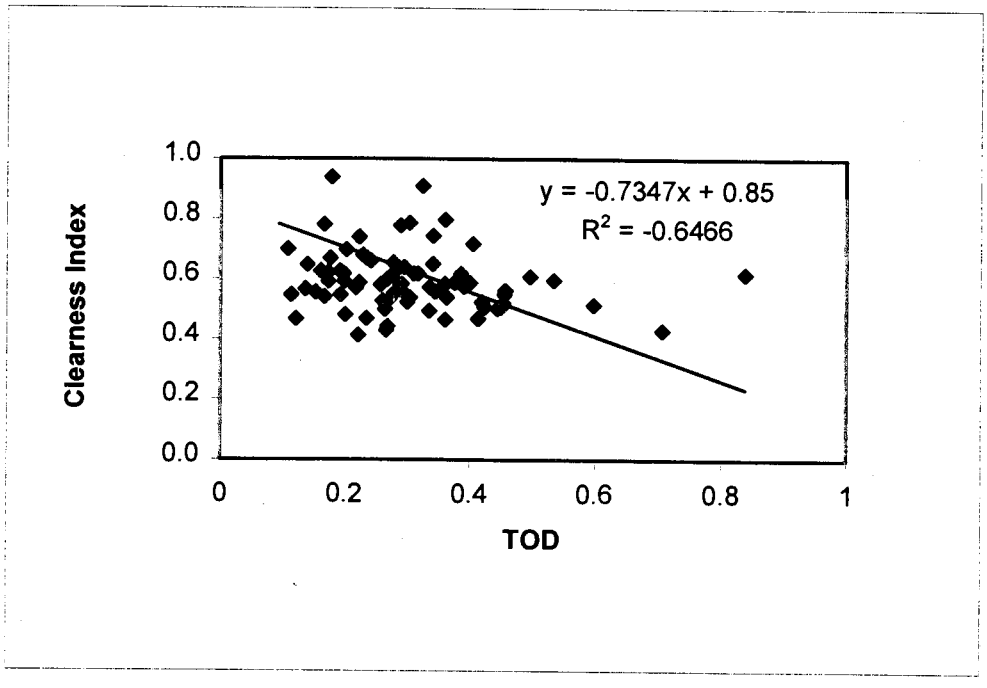

Figure 4.3.13 Clearness index against TOD at Kwangju (January ~ December 2000)

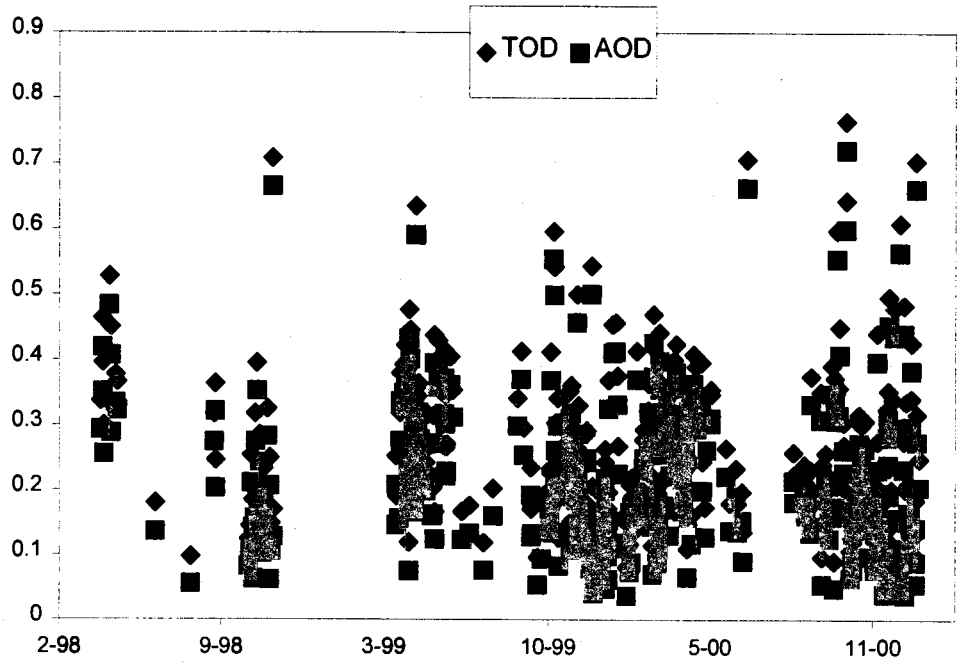

Fig 4.3.14 Total Atmospheric Optical Depth at Kwangju (February 1998 ~ February 2000)

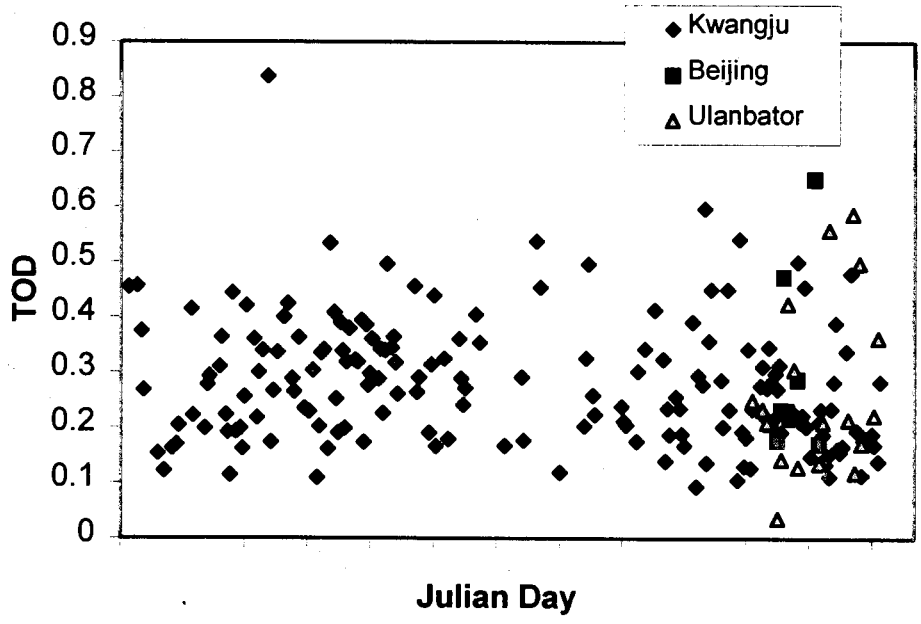

Fig 4.3.15 Total Atmospheric Optical Depth at Kwangju (January ~ December 2000), Beijing (October ~ December 2000), and Ulanbaataar (October ~ December 2000).

4.4 Surface UV radiation over the Northeast Asia

4.4.1 Surface UV radiation monitoring

Table 4.4.1a and b summarize hourly mean UVB andUVA irradiance measured at Kwangju, Korea. Figures 4.4.1a and b are the plots of the diurnal variation of UVB and UVA irradiance at Kwangju, respectively. The maximum values of UVB and UVA irradiance of the measurement period are 1.32 W/m^2 and 41.22 W/m^2 at noon in August, respectively. Diurnal variations of UVB and UVA in summer months, July and August are very similar each other as shown in Figures 4.4.1a and b. This can be attributed to difference in total cloud cover. Even though summer solstice is closer in July, monthly mean total cloud cover in July (6.4/10) was greater than that in August (5.3/10) at Kwangju.

In Table 4.4.2 and Figure 4.4.2, the diurnal variation of UVB irradiance is shown for three months, October ~ December 2000 at Ulaanbaatar, Mongolia. Maximum hourly mean occur at noon for the period. Table 4.4.3 and Figure 4.4.3 show diurnal variation of surface UVB irradiance at Kyoto for two months, November and December 2000. The maximum hourly mean value was observed at noon in November, and between 11:00 AM and noon in December. For Ulaanbaatar and Kyoto, the UVB measurement will continue in the future to get long-term records of UVB irradiance.

The UV irradiances measured by UV radiometer at three sites are compared in Figure 4.4.5.

Table 4.4.1a. Diurnal Variation of UVB irradiance in 2000 at Kwangju, Korea

unit : W/m^2

Hour	Feb	Mar	Apr	May	Jun	Jul	Aug	Sep	Oct	Nov
5			0.01	0.01	0.01	0.01	0.01			
6		0.01	0.01	0.02	0.03	0.03	0.02	0.01	0.01	0.01
7	0.01	0.02	0.05	0.09	0.11	0.12	0.10	0.04	0.02	0.01
8	0.02	0.08	0.16	0.25	0.27	0.32	0.29	0.15	0.11	0.05
9	0.10	0.21	0.37	0.52	0.54	0.61	0.57	0.35	0.30	0.16
10	0.22	0.40	0.61	0.78	0.78	0.91	0.95	0.58	0.51	0.32
11	0.33	0.59	0.81	0.94	0.99	1.14	1.18	0.87	0.70	0.42
12	0.38	0.65	0.87	1.06	1.05	1.26	**1.32**	0.86	0.77	0.47
13	0.37	0.63	0.86	1.08	0.94	1.26	1.13	0.78	0.67	0.37
14	0.29	0.48	0.67	0.87	0.69	1.02	0.92	0.64	0.47	0.24
15	0.16	0.28	0.43	0.57	0.52	0.73	0.62	0.37	0.24	0.11
16	0.06	0.13	0.20	0.31	0.29	0.43	0.35	0.14	0.08	0.03
17	0.01	0.04	0.07	0.12	0.12	0.19	0.16	0.03	0.02	0.01
18	0.01	0.01	0.01	0.03	0.04	0.05	0.04	0.01		
19			0.01	0.01	0.01	0.01	0.01			
No. of data	10	31	29	19	30	23	8	5	27	27

Table 4.4.1b. Diurnal Variation of UVA irradiance in 2000 at Kwangju, Korea

unit : W/m^2

Hour	Feb	Mar	Apr	May	Jun	Jul	Aug	Sep	Oct	Nov
5			0.65	0.92	1.16	0.92	0.80			
6		1.07	2.09	3.38	4.17	3.63	3.09	1.22	0.91	0.45
7	1.46	3.88	7.32	8.83	9.72	10.27	9.37	5.38	3.62	3.53
8	5.05	10.28	15.03	16.57	16.48	17.90	16.75	12.41	10.33	7.06
9	12.63	18.15	24.37	26.76	25.39	25.48	24.78	19.05	18.69	12.53
10	19.83	26.26	32.45	32.85	31.49	32.35	34.24	25.58	25.05	18.66
11	24.87	32.04	37.28	36.01	35.96	36.72	38.36	33.96	30.18	21.50
12	26.06	33.07	38.48	39.28	36.85	39.25	**41.22**	32.34	31.87	22.53
13	25.54	32.78	38.97	40.97	33.87	39.67	35.72	30.53	29.03	19.95
14	23.04	28.15	34.09	35.90	27.22	34.33	31.35	27.90	23.23	16.30
15	16.18	20.40	26.34	27.71	23.53	28.49	24.46	20.08	15.64	11.89
16	8.69	12.70	17.00	19.20	16.47	20.98	17.82	11.16	7.84	7.23
17	2.89	5.73	8.87	10.95	9.88	12.99	11.94	4.24	2.50	4.89
18	0.69	1.56	2.76	4.54	4.53	5.72	5.10	1.06		
19			0.61	1.21	1.23	1.43	1.21			
No. of data	10	31	29	19	30	23	8	5	27	27

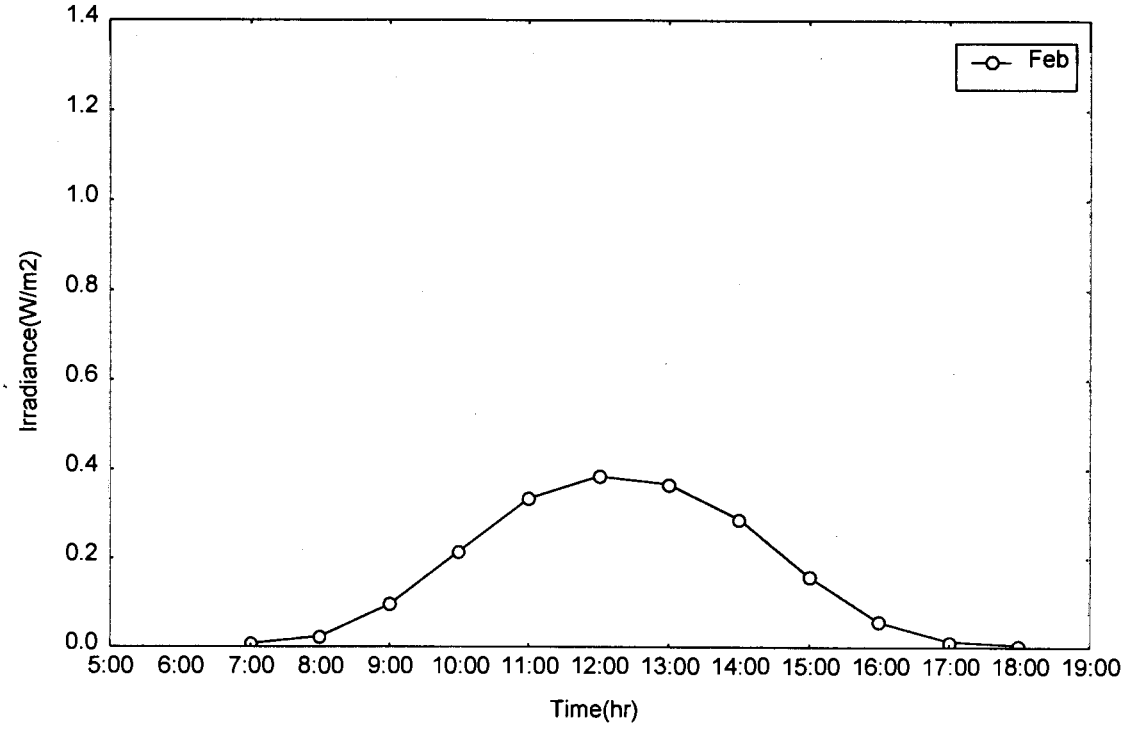

(a) Winter

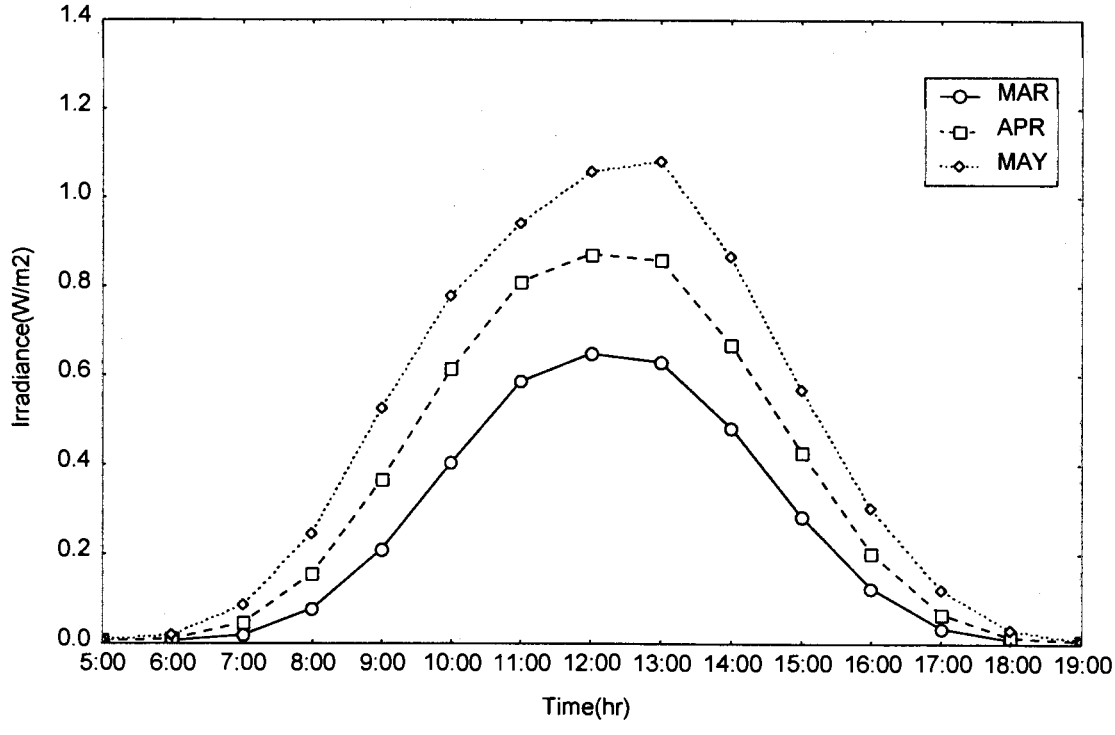

(b) Spring

Figure 4.4.1a. Diurnal Variation of UVB irradiance in 2000 at Kwangju, Korea

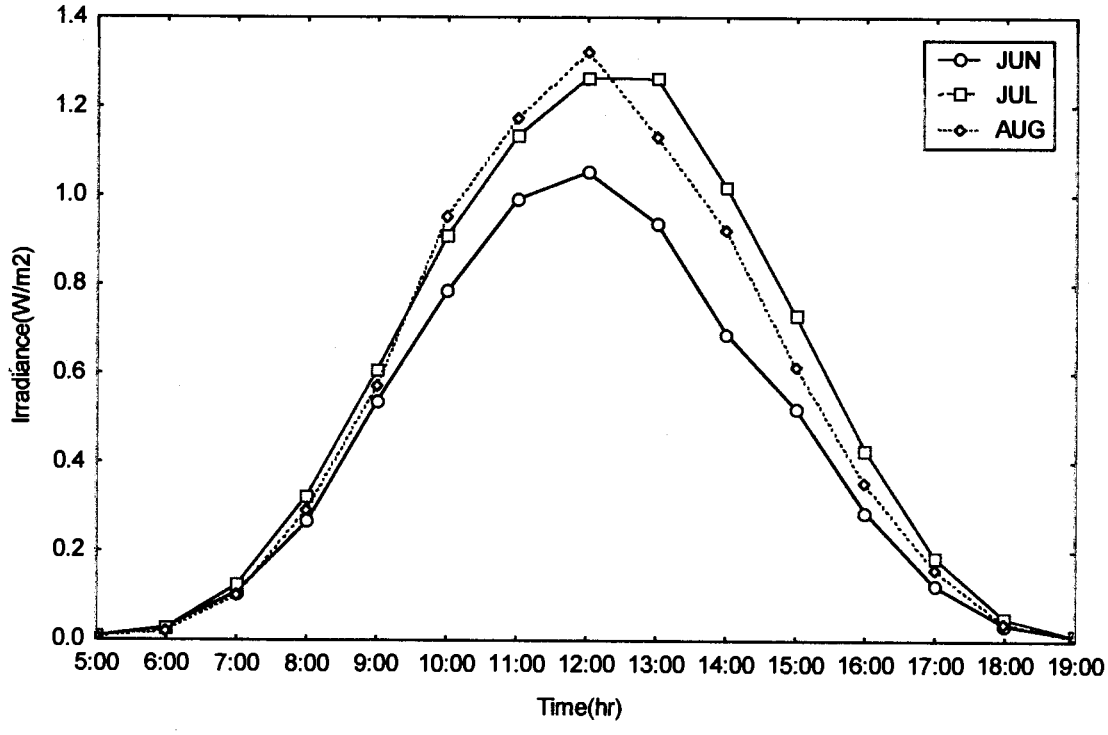

(c) Summer

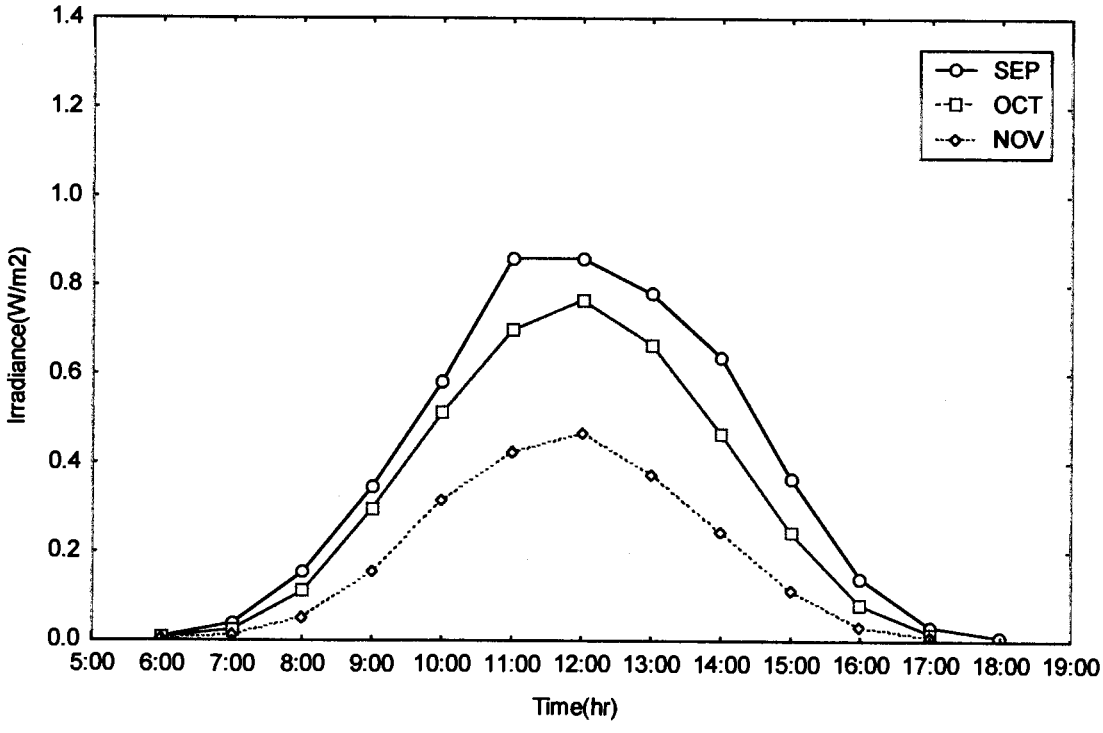

(d) Fall

Figure 4.4.1a. (continued)

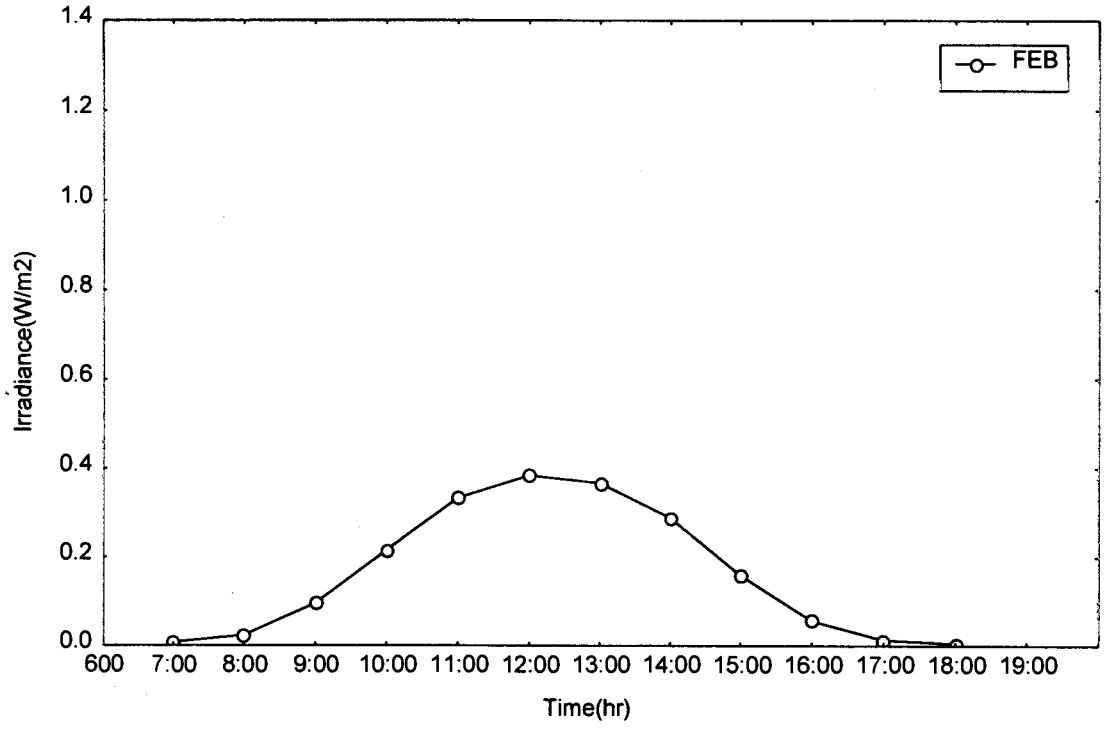

(a) Winter

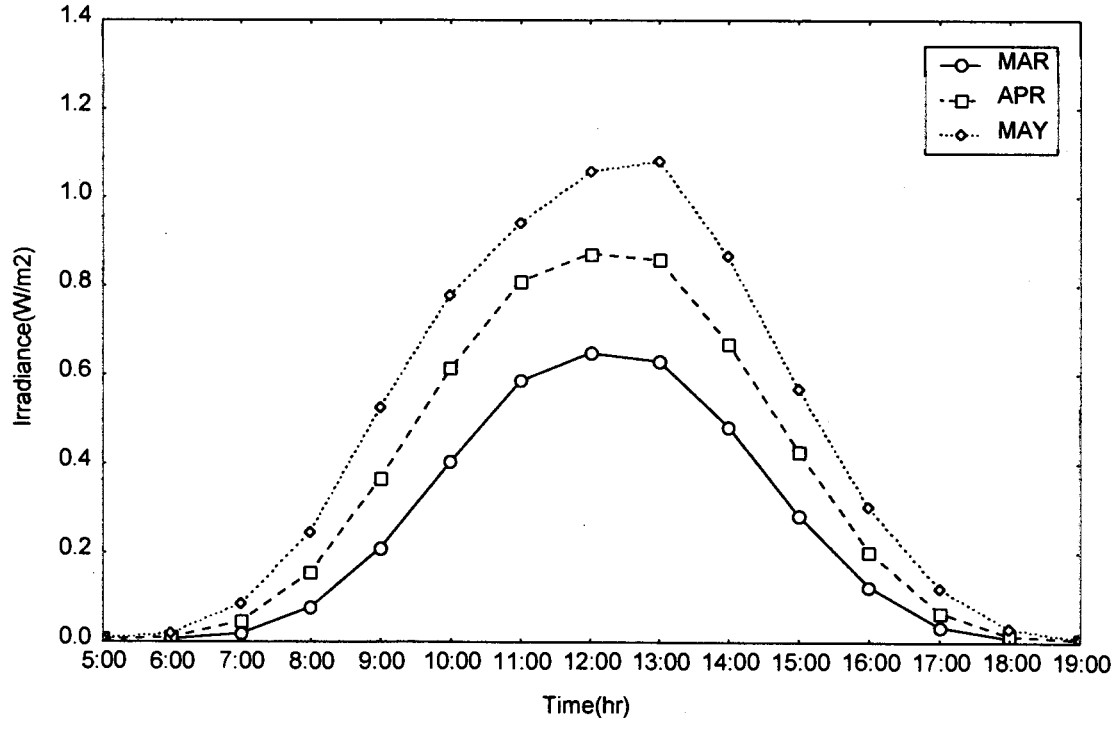

(b) Spring

Figure 4.4.1b. Diurnal variation of UVA irradiance in 2000 at Kwangju, Korea

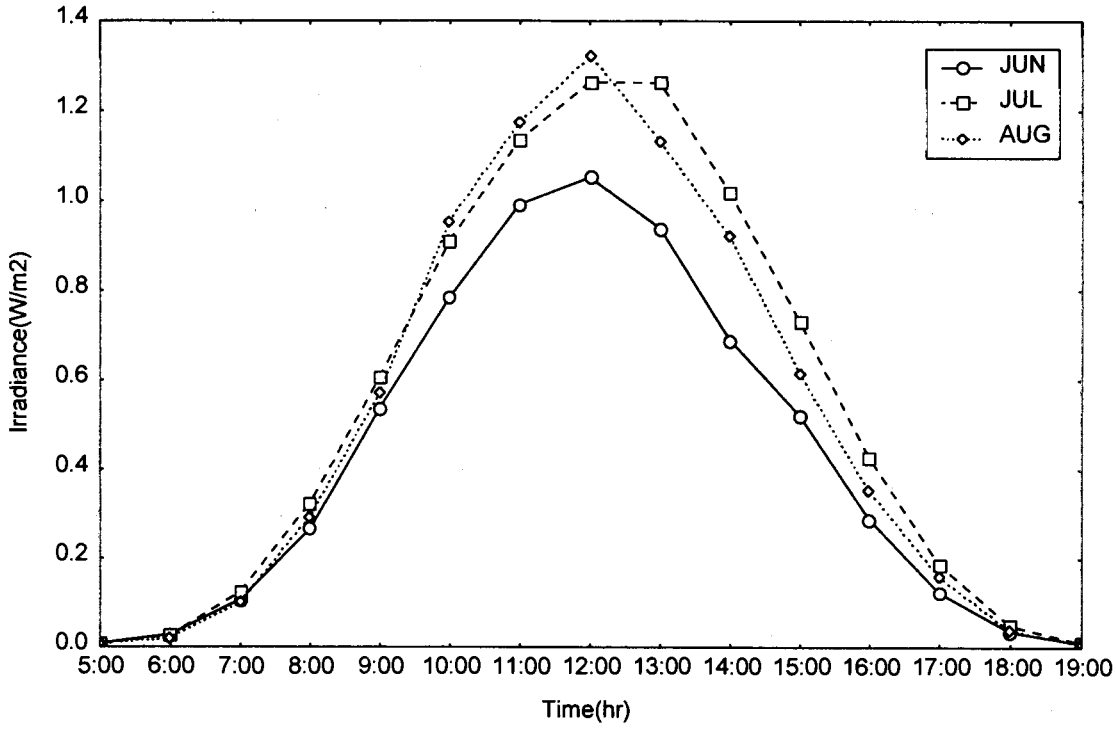

(c) Summer

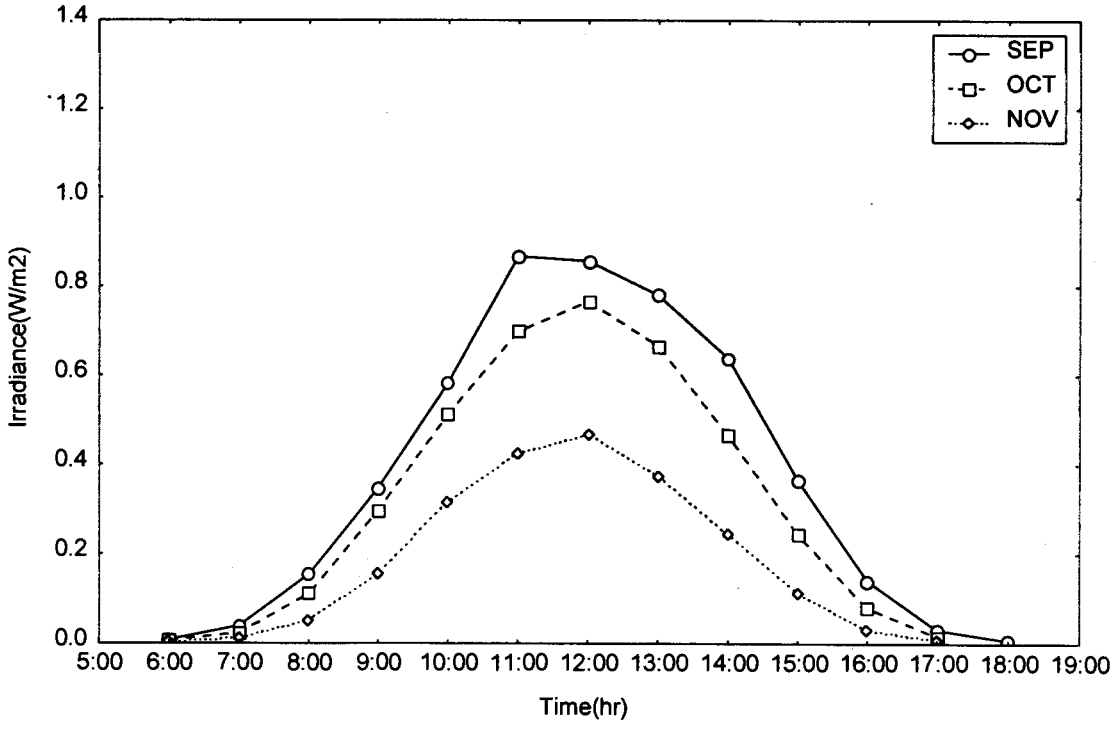

(d) Fall

Figure 4.4.1b. (continued)

Table 4.4.2. Diurnal Variation of UVB irradiance in 2000 at Ulaanbaatar

unit : W/m^2

Hour	Oct	Nov	Dec
8	0.02	0.01	
9	0.08	0.02	0.01
10	0.22	0.06	0.02
11	0.35	0.11	0.04
12	0.41	0.15	0.06
13	0.41	0.14	0.06
14	0.30	0.09	0.04
15	0.15	0.03	0.01
16	0.05	0.01	
17	0.03		

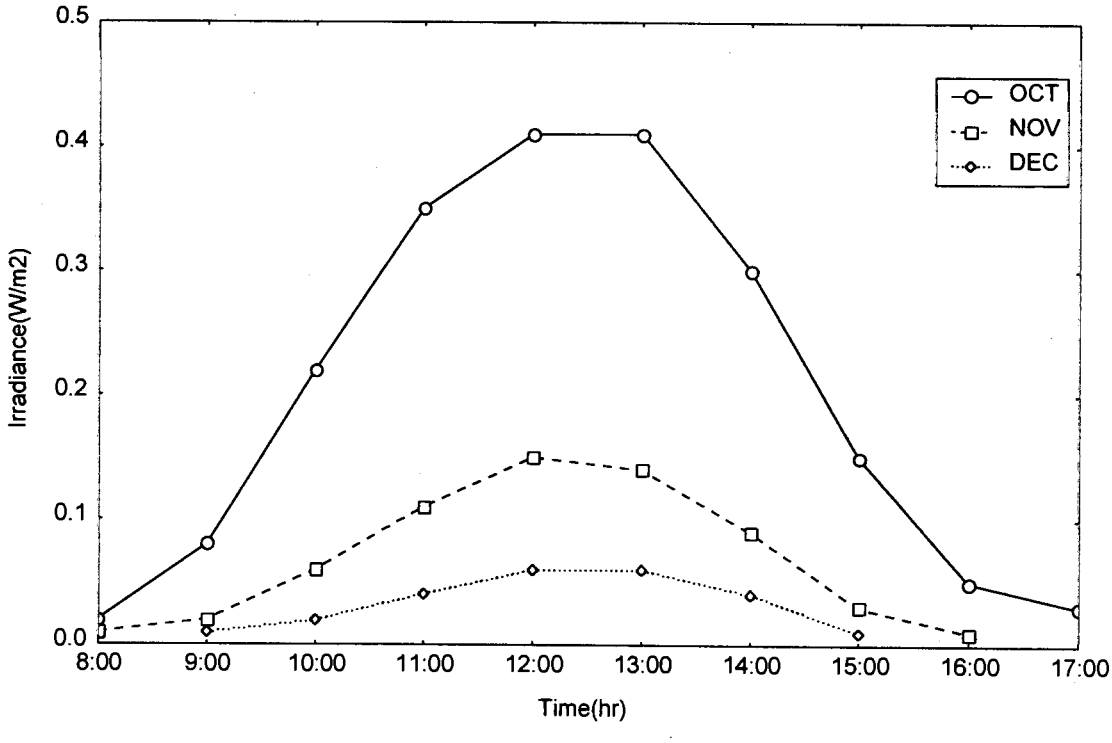

Figure 4.4.2. Diurnal variation of UVB irradiance in 20000 at Ulaanbaatar, Mongolia

Table 4.4.3. Diurnal variation of UVB radiation at Kyoto, Japan 2000

unit : W/m^2

Time	Nov	Dec
7	0.000	0.007
8	0.020	0.052
9	0.103	0.139
10	0.220	0.227
11	0.332	0.270
12	0.396	0.270
13	0.354	0.209
14	0.261	0.116
15	0.154	0.041
16	0.058	0.005

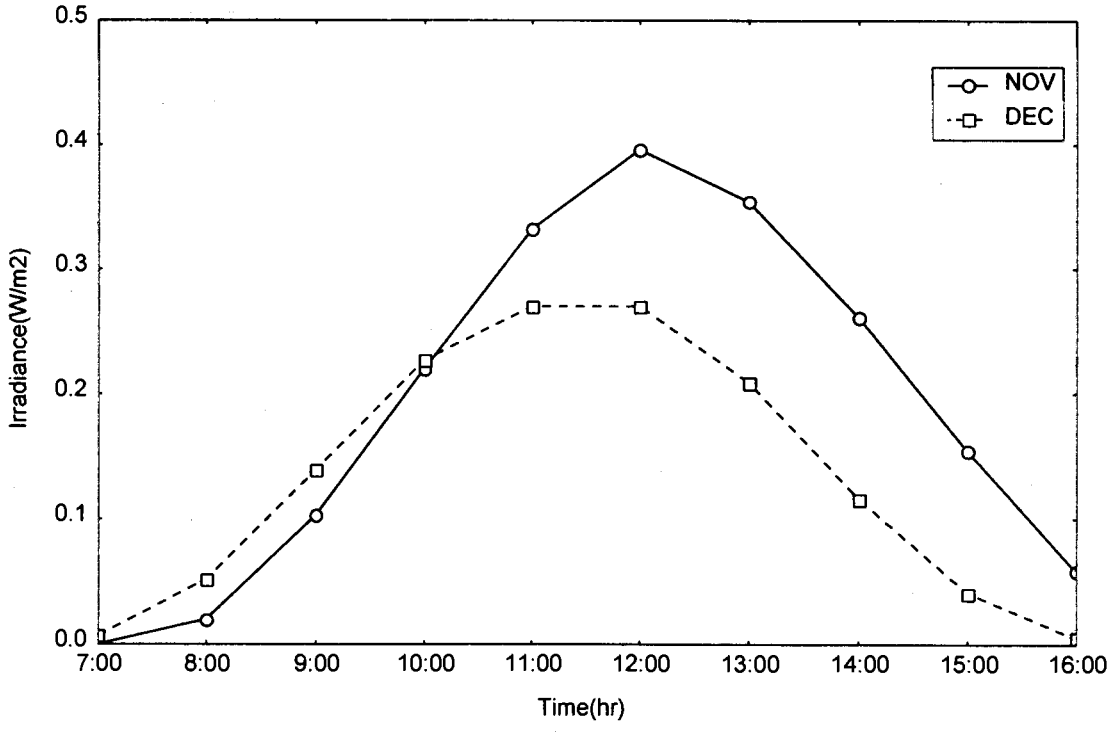

Figure 4.4.3. Diurnal variation of UVB irradiance in 2000 at Kyoto, Japan

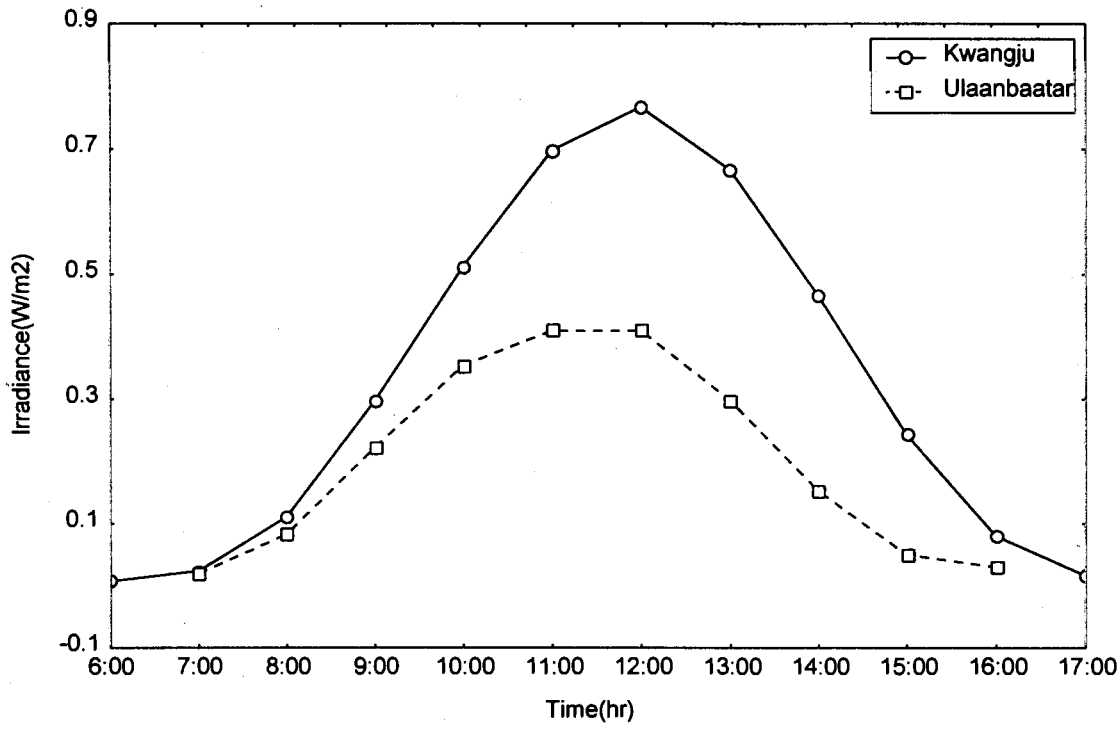

(a) October

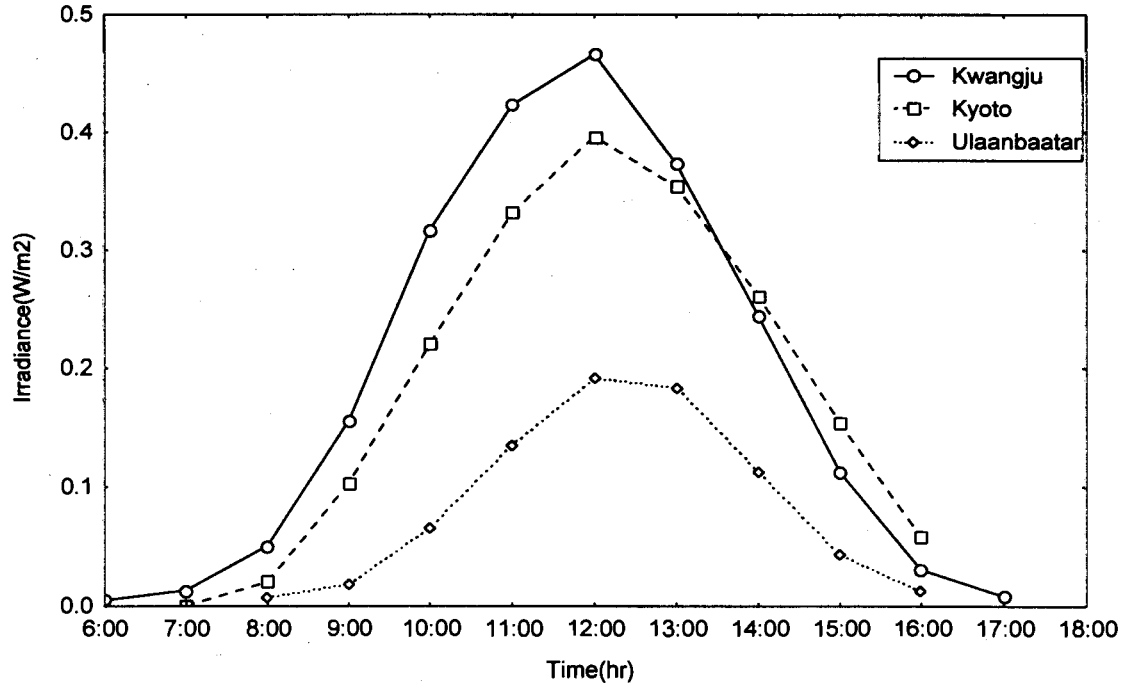

(b) November

Figure 4.4.4. Comparison of surface UVB irradiance in 2000 over the Northeast Asia stations

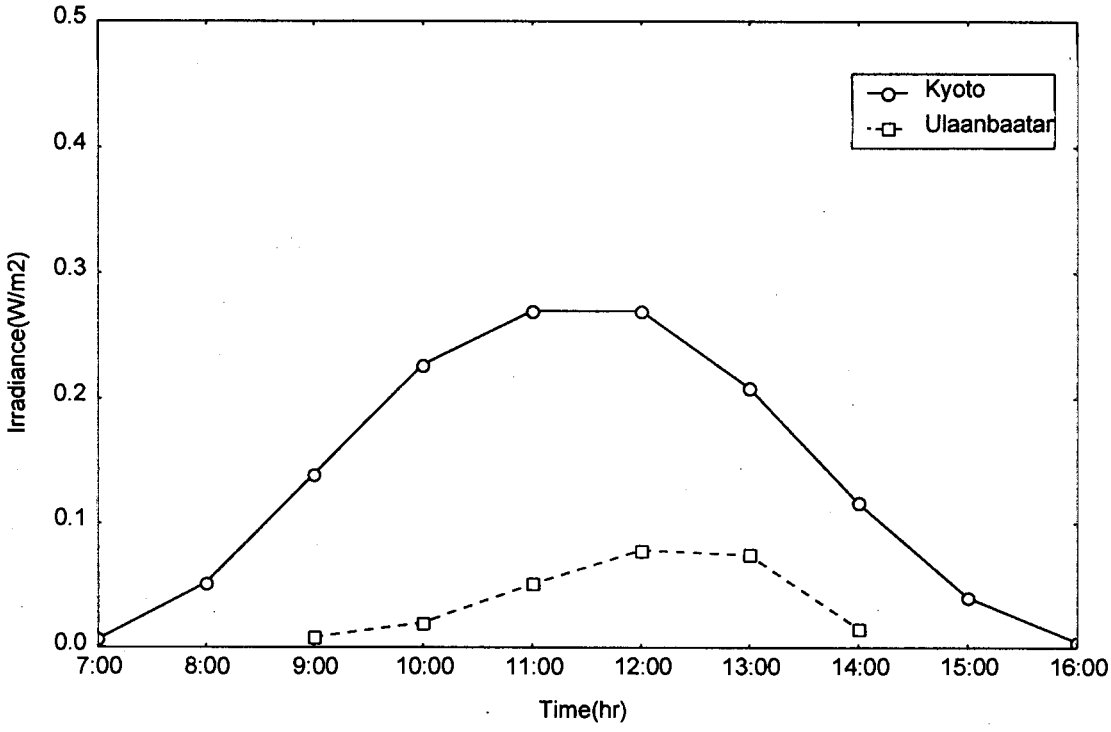

(b) December

Figure 4.4.4. (continued)

4.4.2 Atmospheric aerosol Impact on Surface UV Irradiance

Surface UV radiation varies with relative optical air mass. *Park* [1998] reported that 1% decrease in optical air mass caused 3% ~ 19% increase in surface UV radiation increases in Seoul, Korea. Figure 4.4.5 is a scatter plot of surface UVB radiation versus total column ozone concentration at each solar zenith angle for the data measured during February ~ November 2000. As the relationship between surface UVB radiation and ozone is well known it shows clear anti-correlation. The correlation coefficients between total column ozone and UVB irradiance are - 0.91 ~ - 0.83, which is in good agreement with - 0.95 ~ - 0.84 of *Reid et al.* [1994] in New Zealand.

Figure 4.4.6(a) ~ (c) shows the attenuation of UV irradiance with increasing AOD. In the figures regression lines are plotted which are based on the following equation,

$$I(\theta) = A(\theta)e^{-b(\theta)\tau(\lambda)}$$

where $A(\theta)$, and $b(\theta)$ are constants related to solar zenith angle, $I(\theta)$ is global irradiance(in this case, global UVA and UVB irradiance), and $\tau(\lambda)$ is aerosol optical depth at wavelength λ (*Meleti et al.*, 2000). Regression constants are summarized in Table 4.4.4. Since the surface UVB irradiance is greatly attenuated by total column ozone, the correlation coefficients between AOD and UVA irradiance are larger than those between AOD and UVB irradiance. The $b(\theta)$ values of UVB irradiance are larger than those of UVB irradiance, which is same with *Meleti et al.* 's result (2000). It means shorter wavelength radiation is more sensitive to atmospheric aerosol loading. Table 4.4.5 summarizes the correlation coefficients for two ozone levels, 270 DU and 350 DU confirming that the surface UVB irradiance is strongly affected by the total column ozone. Constants $A(\theta)$ and $b(\theta)$ are also summarized in Table 4.4.5 for two

cases of constant total column ozone, 270 DU and 350 DU. The $b(\theta)$ also increases with solar zenith angle since larger solar zenith angle means longer path length to the surface. Irradiance through longer path length is more attenuated by atmospheric aerosol. For median AOD of 0.198, 1% increase in AOD caused 0.23 %, 0.11 %, and 0.024 % decrease in UVB irradiance, and 12.8 %, 9.0 %, and 3.5 % decrease in UVA irradiance at solar zenith angle of 60°, 70°, and 80°, respectively.

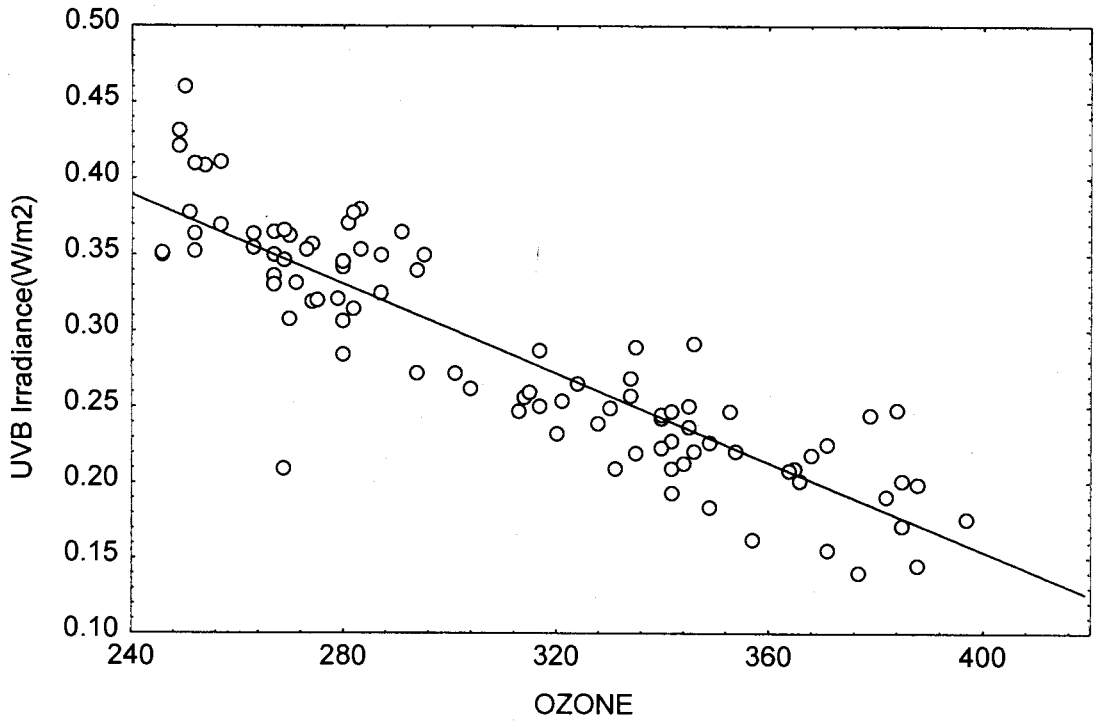
0.50
0.45
0.40
0.35
0.30
0.25
0.20
0.15
0.10
UVB Irradiance(W/m2)
240
280
320
360
400
OZONE

(a)

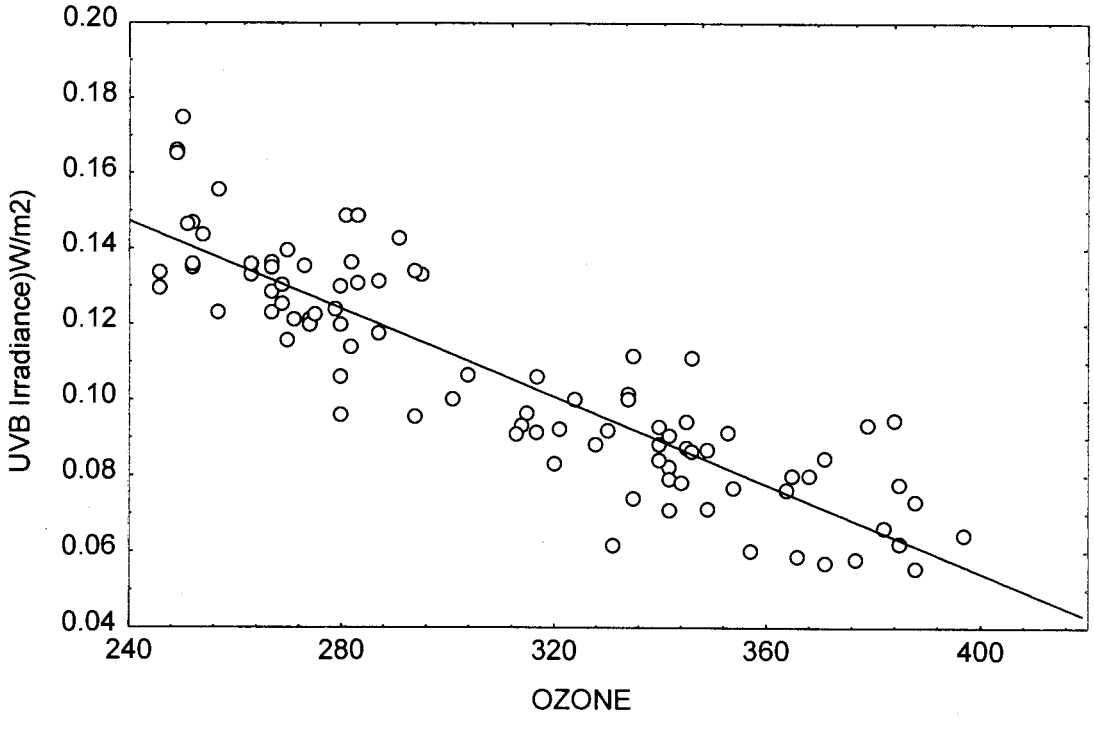
0.20
0.18
0.16
0.14
0.12
0.10
0.08
0.06
0.04
UVB Irradiance)W/m2)
240
280
320
360
400
OZONE

(b)

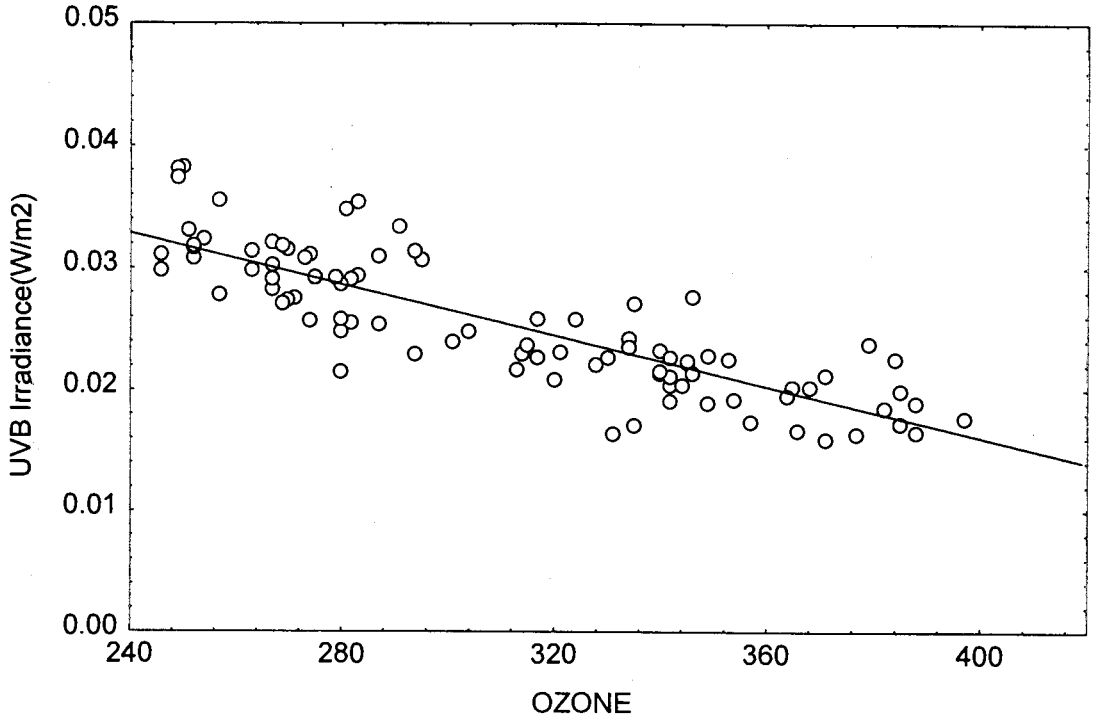

(c)

Figure 4.4.5. Scatter plots of UVB irradiance versus total column ozone (DU) at solar zenith angles ; (a) 60°, (b) 70°, and (c) 80°.

Table 4.4.4 Correlation constants of $A(\theta)$ and $b(\theta)$, and correlation coefficients from the exponential regression fits between the surface UV irradiance and AOD at selected solar zenith angles.

	UVA			UVB		
	$A(\theta)$	$b(\theta)$	r	$A(\theta)$	$b(\theta)$	r
60°	24.68	0.58	**-0.62**	0.33	0.83	**-0.36**
70°	14.46	0.72	**-0.71**	0.13	1.00	**-0.43**
80°	5.73	0.70	**-0.71**	0.03	0.96	**-0.49**

Table 4.4.5 Correlation coefficients(r) between AOD and UVB irradiance and correlation constants of $A(\theta)$ and $b(\theta)$ at selected total column ozone concentrations at selected solar zenith angle

	270 DU (N=22)			350 DU (N=17)		
	$A(\theta)$	$b(\theta)$	r	$A(\theta)$	$b(\theta)$	r
60°	0.37	0.34	-0.66	0.27	0.76	**-0.54**
70°	0.14	0.57	-0.80	0.10	0.82	**-0.56**
80°	0.03	0.71	-0.78	0.03	0.68	**-0.58**

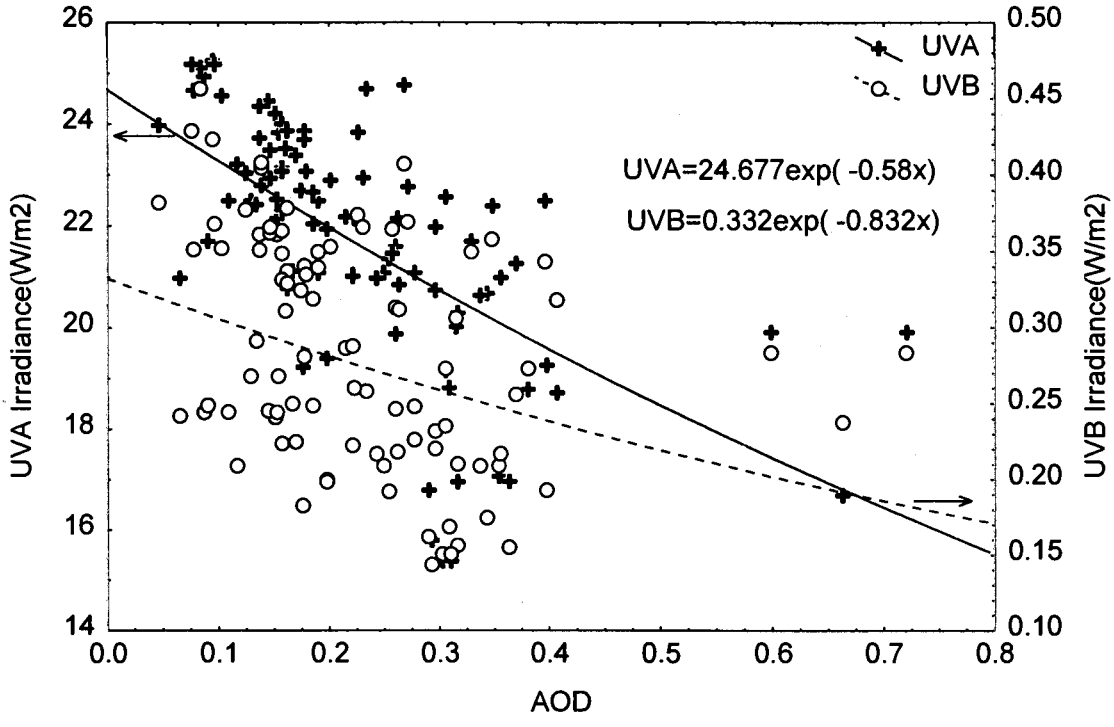
UVA
UVB
UVA=24.677exp(-0.58x)
UVB=0.332exp(-0.832x)
UVA Irradiance(W/m2)
UVB Irradiance(W/m2)
AOD
26
24
22
20
18
16
14
0.50
0.45
0.40
0.35
0.30
0.25
0.20
0.15
0.10
0.0
0.1
0.2
0.3
0.4
0.5
0.6
0.7
0.8

(a)

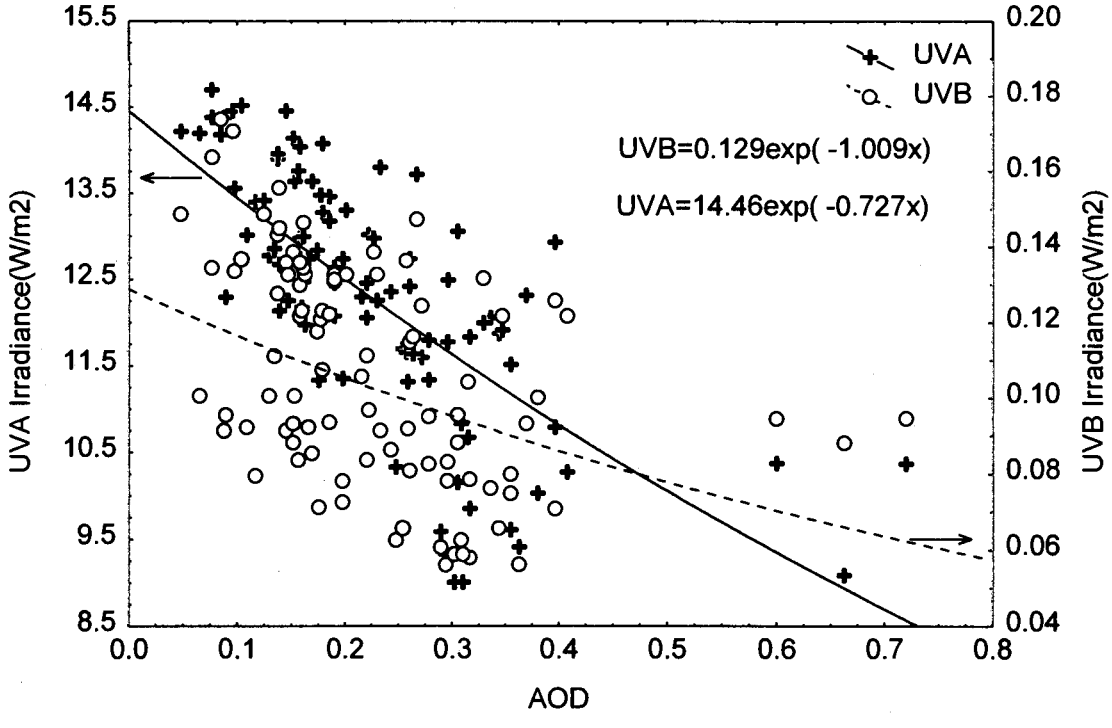
UVA
UVB
UVB=0.129exp(-1.009x)
UVA=14.46exp(-0.727x)
UVA Irradiance(W/m2)
UVB Irradiance(W/m2)
AOD
15.5
14.5
13.5
12.5
11.5
10.5
9.5
8.5
0.20
0.18
0.16
0.14
0.12
0.10
0.08
0.06
0.04
0.0
0.1
0.2
0.3
0.4
0.5
0.6
0.7
0.8

(b)

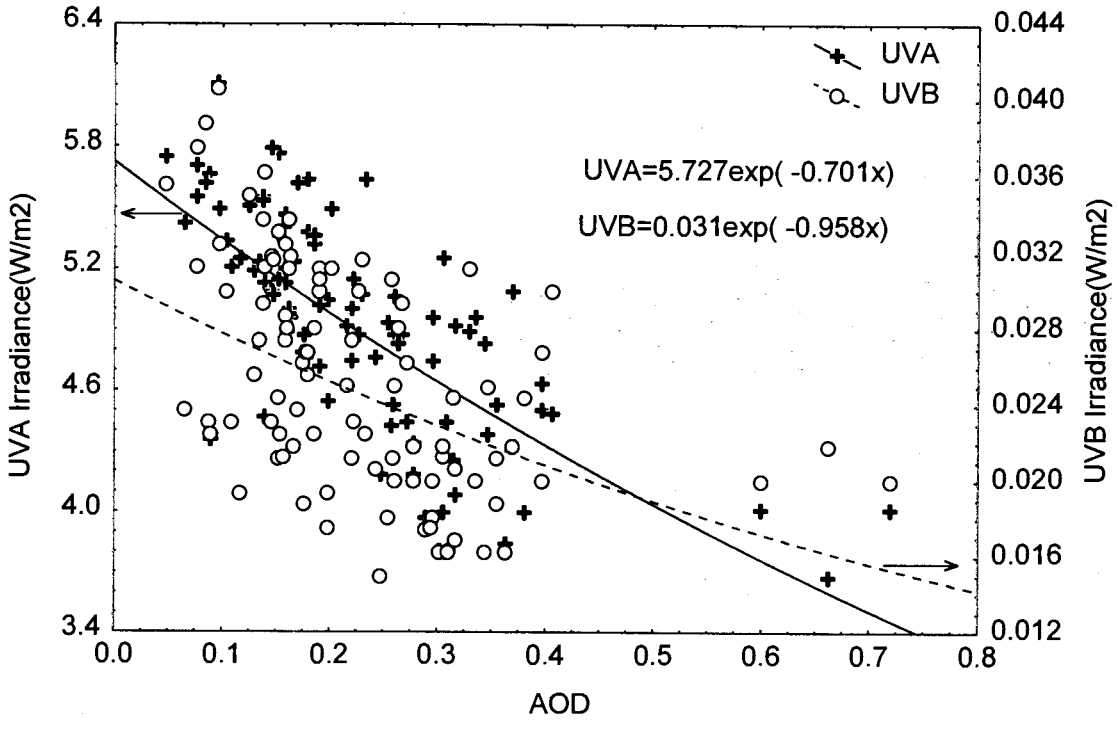

(c)

Figure 4.4.6 Scatter plots of the surface UV irradiance as a function of AOD for different solar zenith angles ; (a) 60°, (b) 70°, and (c) 80°

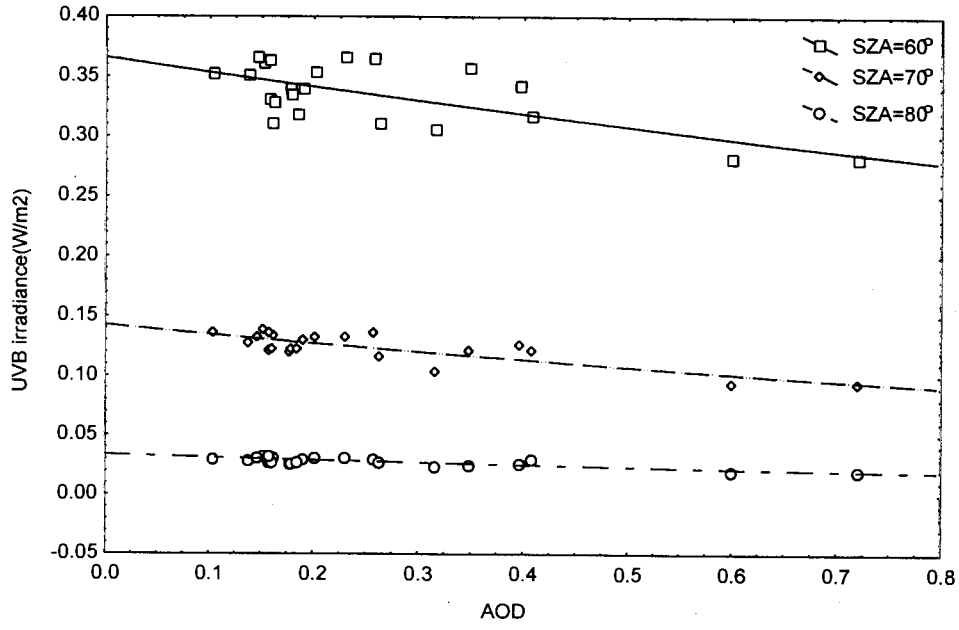

(a)

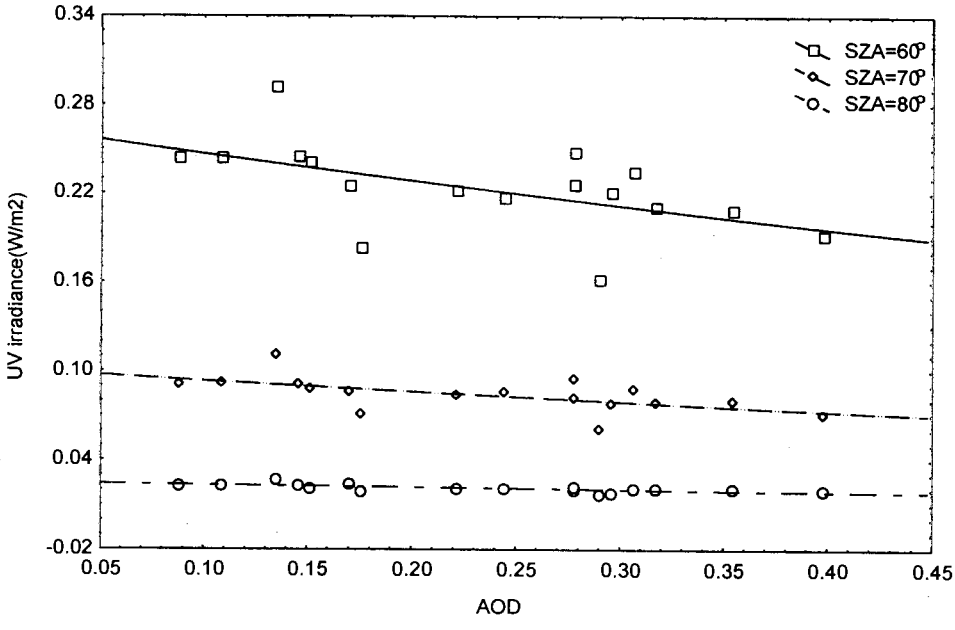

(b)

Figure 4.4.7 Scatter plots and exponential regression fits of UVB irradiance versus AOD at selected solar zenith angle when total ozone column is 270 DU (a) and 350 DU (b).

5. CONCLUSIONS

5. Conclusions

Chemical properties of atmospheric aerosols were analyzed for the aerosol samples collected during at Beijing, China, Kwangju, Korea, and Kyoto, Japan. Concentrations of mass and ion compounds were minimized in summer and maximized in wihnter at all three measurement sites. The Asian dust from China or Mongolia can affect the atmospheric composition over the Northeast Asia in spring. Air mass back trajectory analysis revealed that the characteristics of aerosols were affected by the pathway of the air mass. From the carbon analysis, the ratio of OC to EC has been observed to vary from 0.5 to 3.2 implying the abundance of secondary organic carbon aerosols. Aerosol size distribution over the Kwangju, Korea and Kyoto, Japan shows that fine fraction particle dominate in the urban atmosphere.

The atmospheric aerosol's radiative effect is an important factor that affects the global atmospheric and ground radiative energy budget. Measurement results inthis study show that solar radiation at Kwangju, Ulaanbaartar, and Beijing is greatly attenuated by aerosol particles in the atmosphere as it shows a remarkable seasonal differences in the diurnal variations of global and diffuse radiations in all three sites. At Kwangju, the maximum and minimum daily total atmospheric optical depths were 0.84 and 0.09 in March and October, respectively. The maximum TOD in March can be attributed to the high atmospheric aerosol loading in Kwangju in spring. The minimum TOD in October is resulted from clean air conditions free from dust, The maximum and minimum values of the total atmospheric optical depths at Beijing October ~ December 2000 are 0.65 and 0.17, respectively. This is in strong agreement with the findings of earlier work [Yunfeng et al., 2000] on the characteristics of atmospheric aerosol optical

depth variation over China in the past 30years. The maximum and minimum TOD at Ulaanbaatar October ~ December 2000 were 0.59 and 0.04, respectively.

Two main goals of this study are 1) to monitor the surface UV radiation over the Northeast Asia, and 2) to investigate the aerosol impact on the surface UV irradiance. UV radiometers were installed at Kwangju Ulaanbaatar, and Kyoto to measure the surface UV irradiance. Rotating Shadowband Radiometers (RSR) were also installed to estimate the aerosol optical depth (AOD). Diurnal variation of the surface UVB and UVA irradiance at Kwangju is characterized by maximum value of 1.32 W/m^2 and 41.22 W/m^2 at noon, respectively. Scatter plots of UV irradiance versus aerosol optical depth (AOD) show anticorrelation between surface UV radiation and AOD. For median AOD of 0.198, 1% increase in AOD caused 0.23 %, 0.11 %, and 0.024 % decrease in UVB irradiance, and 12.8 %, 9.0 %, and 3.5 % decrease in UVA irradiance at solar zenith angle of 60°, 70°, and 80°, respectively. Monitoring and characterizing the surface UV radiation will continue at three sites in order to establish a long-term database for atmospheric changes.

REFERENCES

REFERENCES

Hobbs, P. V., Aerosol-Cloud-Climate Interactions, Academic Press, California, pp. 1-31 (1993)

Charlson, R. J., and J. Heintzenberg, Aerosol Forcing of Climate, John Wiley & Sons, England, 43-72, 1994

Chow, J. C., Measurement Methods to Determine Compliance with Ambient Air Quality Standards for Suspended Particles, *J. Air & Waste Manage. Assoc.* 45, 320 - 382, 1995

Meszaros, E. , T. Bareza, A. Geleneser, J. Hlavay, G. Kiss, Z. Krivacsy, A. Molnar and K. Polyak, Size Distributions of Inorganic and Organic Species in the Atmospheric Aerosol in Hungary, *J. Aerosol Sci.* 28, 1163-1175, 1997

Hering, S., A. Eldering and J. H. Seinfeld, Bimodal Character of Accumulation Mode Aerosol Mass Distributions in Southern California, Atmos. Environ., 31, 1- 11, 1997

Seinfeld, J. H., and S. N. Pandis, Atmospheric Chemistry and Physics from Air Pollution to Climate Change, John Wiley & Sons, New York, 700-765, 1998

AH Technical Services, Guidelines for Preparing Reports for the NPS Air Quality Division, 1987.

Beveridge, P., Gearhart, B., and Matsumura, R., Draft - IMPROVE Aerosol Sampler: Instructions and Forms for Siting and Installation, August 1993.

Air Resource Specialists, Inc., Standard Operating Procedures and Technical Instructions for Transmissometer Systems, 1993-1996.

Cahill, T. A., L. L. Ashbaugh, R. A. Eldred, P. J. Feeney, B. H. Kusko, and R. G.

Flocchini, Comparisons between Size-Segregated Resuspended Soil Samples and Ambient Aerosols in the Western United States. *Atmospheric Aerosol:* Source/Air Quality Relationships, Am. Chem. Soc. Symp. Ser., 167, edited by E. Macias, Washington, D.C., 1981.

Cahill, T. A., Eldred, R. A., Wilkinson, L. K., Perley, B. P., and Malm, W. C., Spatial and Temporal Trends of Fine Particles at Remote US Sites (AWMA Annual Meeting & Exhibition), June 1990.

Chow, J. C., Measurement Methods to Determine Compliance with Ambient Air Quality Standards for Suspended Particles, *J. of the Air & Waste Management Association,* ISSN 1047- 3289, May 1995.

Countess, R. J., Wolff, G. T. and Cadle, S. H. The Denver Winter Aerosol: a Comprehensive Chemical Characterization. *J. of the Air Pollution Control Association*, 1980.

Dockery, D. W., and Pope, C. A. Acute Respiratory Effects of Particulate Air Pollution, Annual Review of Public Health 15, 107-132, 1994

Dockery, D. W., Scwartz., J. and Ransom, M. R. Darly Mortality and PM10 Pollution in Utah Valley. Archives of Environmental Health 47, 211-217, 1992

Eldred, R.A., and Cahill, T.A., Trends in Elemental Concentrations of Fine Particles at Remote Sites in the United States, Atmospheric Environment 28-5:1009-1019, 1994.

Friedlander S.K., Smoke, Dust and Haze, 122, John Wiley & Sons, 1977.

Gray, H. A., Cass, G. R., Source Contributions to Atmospheric Fine Carbon Particle Concentrations, Atmospheric Environment Vol. 32, No. 22, 3805-3825, 1998.

Haas, P.J., Technical Note - Visibility: Modeling, Monitoring and Regulation, March

1980.

IMPROVE, Spatial and Temporal Pattern and the Chemical Composition of the Haze in the United States, 1993.

Malm, W. C., Gebhart, K. A., Molenar, J., Cahill, T. A., Eldred, R. E., and Huffman, D., Examining the Relationship Between Atmospheric Aerosols and Extinction at Mount Rainier National Park, *Atmospheric Environ*ment 28, 347-360, 1994.

Malm, W. C., J. F. Sisler, D. Huffman, R. A. Eldred, and T. A. Cahill, Spatial and Seasonal Trends in Particle Concentration and Optical Extinction in the United States. *J. Geophys, Res.*, 99(D1), 1347-1370, 1994.

Pitchford, M. L., M. C. Green, H. P. Kuhns, I. Tombach, W. C. Malm, M. Scruggs, R. J. Farber and V. Mirabella Project MOHAVE Final Report, 5-1～5-14, 1999.

Monitoring System for Visibility Studies. Proc. APCA (Air Pollution Control Assoc.) Ann. Mtg., 81, 1-16, 1988.

National Research Council Protecting Visibility in National Parks and Wilderness Areas, National Academy Press, 127～129, 1993.

Pitchford, M.L., and W. C. Malm, Development and Application of a Standard Visual Index, Atmospheric Environment 28, 1049-1054, 1994.

Sisler, J. F., D. Huffman, D. A. Latimer, W. C. Malm, and M. L. Pitchford, Spatial and Temporal Patterns and the Chemical Composition of the Haze in the United States: An Analysis of Data from the IMPROVE Network 1988-1991 - Vol. I (ISSN No. 0737-5352-26), February 1993.

Tombach, I., Walther, E. G., Huang, A., and Ligh, D., Performance Criteria for Monitoring Visibility-Related Variables (AV-FR-87/635), November 1990.

Turpin, B. J., Huntzicker, J. J., Larson, S. M. and Cass, G. R. Los Angeles Summer

Energy 43, 325-330, 1989

IMPROVE, Spatial and Temporal Pattern and the Chemical Composition of the Haze in the United States, 1993.

Kuye A. and S. S. Jagtap, Analysis of solar radiation data for Port Harcourt, Nigeria. *Solar Energy*, 49(2), 139-145. 1992

Al-Dhafriri, A. M., M. S. Al-Ayed, and M. Bin Mahfoodh, Long-term Monitoring and Analysis of Hourly Solar UV Radiation in the 290~380 nm Range in the Middle Region of Saudi Arabia, *J. Air & Waste Manage. Assoc.*, 50, 1045~1049, 2000

Bais, A. F., M. Blumthaler, A. R. Webb, J. Groebner, P. J. Kirsch, B. g. Gardiner, C. S. zerefos, T. Svenoe, and T. J. Martin, Spectral UV Measurements over Europe within the Second European Stratospheric Arctic and midlatitude Experiment Activities, *J. of Geophys. Res.*, 102(D7), 8731-8736, 1997

Bernhard, G., B. Mayer, G. Seckmeyer, and A. Moise, Measurements of Spectral Solar UV Irradiance in Tropical Australia, *J. Geophys. Res.*, 102(D7), 8719~8730, 1997

Cappellani, F., C. Kochler, Ozone and UV-B variations at Ispra from 1993 to 1997, *Atm. Env.*, 33, 3787~3790, 1999

Estupinan, Jeral G., Sethu Faman, Gennaro H. Crescenti, John J. Streicher, and Willian F. Barnard, Effects of Clouds and Haze on UV-B Radiation, *J. of Geophys. Res.*, 101(D11), 16,807-16,816, 1996

Grobner, J., A. Albold, M. Blumthaler, T. Cabot, A. De la Casiniere, J. Lenoble, T. Martin, D. Masserot, M. Muller, R. Philipona, T.Pichler, E. Pougatch, G. Rengarajan, D. Schmucki, G. Seckmeyer, C. Sergent, M. L.Toure, and P. Weihs, Variability of Spectral Solar Ultraviolet Irradiance in an Alpine Environment, *J. of Geophys.*

Res., 105(D22), 26,991~27,003, 2000

Harrison, Lee, and Joseph Michalsky, Objective Algorithms for the Retrieval of Optical depths from Ground-based Measurements, *Applied Optics*, 33(22), 5126-5132, 1994

Iqbal, Muhammad, *An Introduction to Solar Radiation*, Academic Press, 1983

Kim, Jeongeun, Seong Y. Ryu, and Young J. Kim, *Proceedings of the Third International Symposium on Advanced Environmental Mnitoring*, 255-256, 2000

Kylling, A., A. f. Bais, Blumthaler, J. Schreder, C. S. Zerefos, and E. Kosmidis, Effect of aerosols on Solar UV Irradiances during the Photochemical Activity and Solar Ultraviolet Radiation Campaign, *J. of Geophys. Res.*, 103(D20), 26,051-26,060, 1998

Kwon, H. J., Variations of the Surface Ultraviolet-b radiation with Changes in the Ozone Layer, MS Dissertation, 1996

Mayer, B., G. Seckmeyer, Systematic Long-term Comparison of Spectral UV measurements and UVSPEC Modeling Results, *J. Geophys. Res.*, 102(D7), 8755~8767, 1997

Meleti, C., Cappellani, F., Measurements of Aerosol Optical Depth at Ispra : analysis of the Correlation with UV-B, UV-A, and Total Solar Irradiance, *J. Geophys. Res.*, 105(D4), 4971~4978, 2000

Min, Hee-Kyoung, A Study on Variation of Aerosol Optical Depth (AOD) in the Atmosphere using RSR (Rotating Shadowband Radiometer) data, MS Dissertation, 2000

Park, Ji Yong, Sensitivity of Surface UV Radiation due to Changing Total Ozone in the

Ozone in the Frederick Model, MS Disseration, Yonsei University, 1998

Reid, E. Basher, X. Zheng and S. Nichol, Ozone-related Trends in Solar UVB series, *Geophys. Res.* Lett., 21, 2719-1716, 1994

Sabziparvar, Ali A., Piers M. de F., and Keith P. Shine, Changes in Ultraviolet Radiation due to Stratospheric and Tropospheric Ozone Changes since Preindustrial times, *J. Geophys. Res.*, 103(D20), 26,107~26,113, 1998

Tsay, Si-Chee, Ultraviolet Radiationin the Arctic ; The Impact of Potential Ozone Depletion and Cloud Effects, *J. Geophys. Res,..*97(D8), 7289-7840, 1992

UVB-1 Ultraviolet Pyranometer Installation and User Guide, ver.2.0, Yankee Environmental Systems, Inc., 1997

Weele, Michale Van, Effect of Clouds on Ultraviolet Radiation : photodiss-ociation rates of chemical species in the troposphere, 19

ACKNOWLEDGEMENTS

ACKNOWLEDGEMENTS

The authors gratefully acknowledge the support of the Asia-Pacific Network for Global Change Research (APN) and global change for SysTem for Analysis Research and Training (START) for financing this project under the research grant APN 2000-16. We are very thankful for the provision of fund for the establishment of the radiation stations at Kwangju, Beijing, Ulanbator and Kyoto. Thanks are also due to the Advanced Environmental Monitoring Research Center for all the administrative support for the success of this project.

We equally wish to express our profound gratitude to all our principal investigators, Prof. Shi (Institute of Atmospheric Physics, China), Prof. Kasahara (Kyoto University, Japan) and Dr Bulgan (Central Laboratory of Environmental Monitoring, Mongolia) for their immense contributions.

Advanced Environmental Monitoring Research Center (ADEMRC)
Kwangju Institute of Science and Technology (KJIST)
1 Oryong-dong, Puk-gu, Kwangju, 500-712, Korea
Tel : +82-62-970-3402, 3403 Fax : +82-62-970-3404